Supramolecular structures of dendronized polymers and DNA on solid substrates

DISSERTATION

zur Erlangung des akademischen Grades
doctor rerum naturalium
(Dr. rer. nat.)
im Fach Physik

eingereicht an der
Mathematisch-Naturwissenschaftlichen Fakultät I
Humboldt-Universität zu Berlin

von
Frau Dipl.-Phys. Illdiko Maria Gössl
geboren am 03.02.1974 in Kassel

Präsident der Humboldt-Universität zu Berlin:
Prof. Dr. Jürgen Mlynek

Dekan der Mathematisch-Naturwissenschaftlichen Fakultät I:
Prof. Dr. Michael Linscheid

Gutachter:

1. Prof. Dr. J. P. Rabe
2. Prof. Dr. B. Röder
3. Prof. Dr. R. R. Netz

eingereicht am:	15.4.2003
Tag der mündlichen Prüfung:	30.6.2003

Abstract

Complexes of oppositely charged polyelectrolytes play an important role in both biology and material science, for instance DNA condensation in vitro, nucleosomal structure, non-viral gene transfection systems as well as layer-by-layer adsorption. Although there are theories predicting overcharging of polyelectrolyte complexes, the driving forces are still under debate and systematic experimental studies on single polyelectrolytes remain challenging. Therefore the question arose if it is possible to analyze *single* polyelectrolyte complexes, using DNA and dendronized polymers, with the scanning force microscope in order to investigate the complexation in detail.

For the complex analysis, the polyelectrolytes were allowed to interact in solution and then to adsorb on negatively charged mica or on mica coated with a positively charged polymer. Scanning force microscopy was used to investigate the adsorbed species. DNA/dendronized polymer complexes of charge ratio of 1/1 through 1/0.7 adsorbed on mica coated with a positively charged polymer. The analysis of high resolution molecular images indicated that DNA wraps around the dendronized polymer with an estimated pitch of (2.30 ± 0.27) nm and (2.16 ± 0.27) nm for dendronized polymers of generation two and four, respectively. In the proposed model the polyelectrolyte with the smaller linear charge density is wrapped around the more highly charged dendronized polymer, resulting in a negatively overcharged complex. This overcharging is consistent within recent theories of spontaneous overcharging of complexes of one polyelectrolyte wrapping around the other.

Using the complex of DNA and dendronized polymers of second generation, the influence of monovalent salt concentration on the molecular structure was studied. By increasing the salt concentration the pitch showed a minimum as predicted by the interplay of electrostatic forces and entropic interactions of polyelectrolyte adsorption. At high salt concentration (2.4 M NaCl) the release of DNA from the complex can be observed.

The results showed that the DNA/dendronized polymer system can be used as a new, high potential model system to investigate single polyelectrolyte interactions. With regard to recent theories, the experimental results indicate that the overcharging of the complex is mainly driven by electrostatic forces whereas contributions of counterion entropy and bending energy seem to be negligible. This understanding may be useful for the design of single polyelectrolyte complexes for non-viral gene delivery systems and might help to optimize the transfection efficiency based on the structure of the vector system.

Keywords:
DNA complex, polyelectrolyte complex, influence of salt concentration, scanning force microscopy

Abstract

Komplexe aus entgegengesetzt geladenen Polyelektrolyten haben sowohl in der Biologie als auch in den Materialwissenschaften eine große Bedeutung. Im Mittelpunkt des Interesses stehen besonders die Kondensation der DNA in vitro, die Struktur des Nukleosoms im Zellkern, nicht-virale Systeme zur Transfektion von DNA in Zellen oder der Vorgang der layer-by-layer Adsorption. Verschiedene Theorien befassen sich mit den treibenden Kräften solcher Komplexbildungen. Allerdings standen experimentelle Untersuchungen auf diesem Gebiet bisher noch aus. Dieser Arbeit liegt die Fragestellung zu Grunde, ob es mit Hilfe der Rasterkraftmikroskopie möglich ist, die Struktur *einzelner* Polyelektrolytkomplexe, bestehend aus den beiden Polyelektrolyten DNA und dendronisierten Polymer, aufzuklären und ihre Komplexbildung zu untersuchen.

Die Komplexe bildeten sich in Lösung und wurden anschließend auf einer unbeschichteten oder mit positiven Polymeren beschichteten Glimmeroberfläche adsorbiert. Auf der positiv beschichteten Glimmeroberfläche hafteten DNA-dendronisierte Polymer Komplexe mit einem Ladungsverhältnis von 1:1 bis 1:0.7 (DNA:dendronisiertes Polymer). Anhand der hochaufgelösten rasterkraftmikroskopischen Aufnahmen wurde ein Modell entwickelt, das die Umwicklung der DNA um das dendronisierte Polymer beschreibt. Der DNA-DNA Abstand ergab sich zu (2.30 ± 0.27) nm für den Komplex mit DNA und zweiter Generation dendronisierter Polymere und zu (2.16 ± 0.27) nm mit vierter Generation. Die theoretische Vorhersage der Überladung der Komplexe konnte experimentell bestätigt werden.

Mit Hilfe der Rasterkraftmikroskopie konnte überdies der Einfluss des Salzgehaltes der Lösung auf die Bildung der Komplexe mit DNA und zweiter Generation dendronisierter Polymere untersucht werden. Wie man anhand des Zusammenwirkens von elektrostatischen Kräften und entropischen Wechselwirkungen bei der Adsorption von Polyelektrolyten vorhersagen kann, durchlief der DNA-DNA Abstand ein Minimum bei ansteigendem Salzgehalt. Bei sehr hohem Salzgehalt (2.4 M NaCl) konnte das Ablösen der DNA von dem Komplex beobachtet werden.

Die untersuchten DNA/dendroniserten Polymer Komplexe bilden ein neues Modellsystem, mit dem einzelne Polyelektrolyt-Wechselwirkungen direkt untersucht werden können. Ein Vergleich der experimentellen Daten mit den vorhandenen Theorien zeigte, dass der Prozess des Überladens weitgehend durch elektrostatische Wechselwirkung zwischen den beiden Polyelektrolyten beschrieben werden kann. Sowohl entropische Beiträge als auch die Biegeenergie der umwickelnden DNA sind vernachlässigbar. Basierend auf diesen Ergebnissen können neue Trägerstrukturen für effizientere nicht-virale DNA-Transfektionssysteme entwickelt werden.

Schlagwörter:
DNA Komplex, Polyelektrolytkomplex, Einfluss des Salzgehaltes, Rasterkraftmikroskopie

meinen Eltern

Contents

Chapter 1

Introduction

Deoxyribonucleic acid (DNA) organizes into tightly packed structures in viruses and cells. Of special interest is the precise packing of DNA molecules in the nucleus, i.e. the nucleosomes. Here, the DNA molecule is wrapped around a protein core (see Figure) that carries charges opposite to that of DNA. Much research has been carried out in order to obtain insight into the mechanisms of this complexation of DNA molecules using oppositely charged macroions [1]. However, the molecular structure of most DNA complexes is not well understood and remains experimentally a challenge [2].

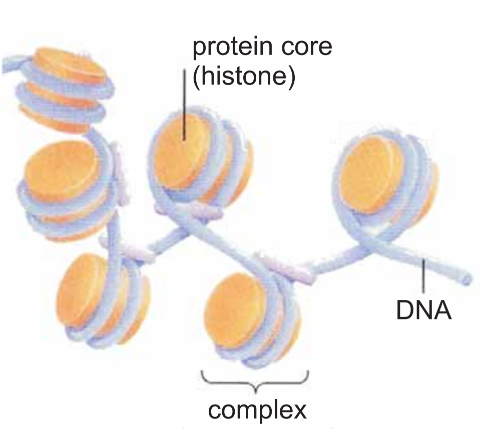

Polymers containing charges like DNA belong to a special class of molecules, called polyelectrolytes. In solution, electrostatic attraction between oppositely charged polyelectrolytes will induce polyelectrolyte complexes. In many areas like biology, medicine, biotechnology and materials science, single polyelectrolyte complexes become more and more important [3].

Furthermore, a molecular-level understanding of polyelectrolyte complexation is expected to have a strong impact on our views of, e.g., DNA complexation, non-viral gene transfection, the structure of nucleosomes, and the fabrication of thin polyelectrolyte films using layer-by-layer deposition. In addition, controlling the polyelectrolyte complexation becomes of special interest since in many processes the efficiency generally correlates with the packing density and structure of the complex [4].

In this study, a new model system for oppositely charged polyelectrolyte interaction is introduced: Negatively charged DNA molecules and positively charged dendronized polymers. The physicochemical properties of the latter include high surface charge density and water solubility, providing the potential for electrostatic interaction with DNA. Other outstanding properties of this special kind of polymers are its high stiffness (persistence length) and high molar mass [5].

Due to the electrostatic attraction between the two oppositely charged polyelectrolytes, they will form complexes. In this complexation process there are many factors partially competing like charge density and stiffness of the polyelectrolytes as well as ionic strength of the solution. Thus, the influence of theses parameters are also investigated for the special DNA/dendronized polymer complex, taken as a model system for polyelectrolyte interaction.

The structure analysis of single DNA molecules, dendronized polymers and complexes thereof was carried out by scanning force microscopy. Here, the ability of the scanning force microscope was used to measure three dimensional profiles with nanometer resolution [6]. Furthermore, it has been shown that the scanning force microscope became a powerful tool to determine molecular characteristics of macromolecules as molar mass distributions and chain stiffness [7]. For investigation, the molecules and the complex are adsorbed onto modified solid substrates.

In the next chapter, the motivation of this thesis is presented by introducing the high potential of the used biological and chemical systems (chapter 2). The technique of the scanning force microscope is also described in chapter 2. Furthermore, the chapter introduces important chemical and physical properties of polyelectrolytes and the theory of their interaction in aqueous solutions in general. The specific characteristics of the materials used in this study is given in chapter 3 and the chapter also includes an overview of the experimental setup, the preparation techniques as well as the data analysis. Finally, the results are summarized in chapter 4. Each result section also includes the final discussion. Chapter 5 completes the thesis with the conclusions and perspectives.

Chapter 2

Basics and Theory

Fundamental research into the properties of molecules of life is based on chemistry, biology and physics. In this chapter the biological and chemical systems which are not only of fundamental interest but also the motivation for this study will be introduced. First (section 2.1), the molecular and physical structure of Deoxyribonucleic Acid (DNA) and proteins are given. The second section 2.2 focuses on biological interactions in nature mainly driven by electrostatic forces resulting in highly ordered and specific structures. Polymers which have the potential to mimic biological structures are discussed in section 2.3. Also an overview of the synthesized polymers is given that are used in this study. Finally the last section 2.4 presents results on the interaction between polymers into complexes which have been obtained so far.

Furthermore, this chapter concentrates on the background concerning the experimental setup as well as the analysis used in this thesis. Thus, the concept of the scanning force microscope is described in section 2.5. In section 2.6 fundamental characteristics of polymers are introduced, whereas in section 2.7 the unique properties of polyelectrolytes in aqueous solution are discussed. An overview of polyelectrolyte adsorption is given in the last section 2.8.

2.1 Biological Macromolecules

2.1.1 DNA

In 1962 the Nobel prize was awarded to J. D. Watson and F. H. C. Crick for the three-dimensional structure of DNA. They revealed the double-helical structure of DNA through their interpretation of X-ray diffraction data.

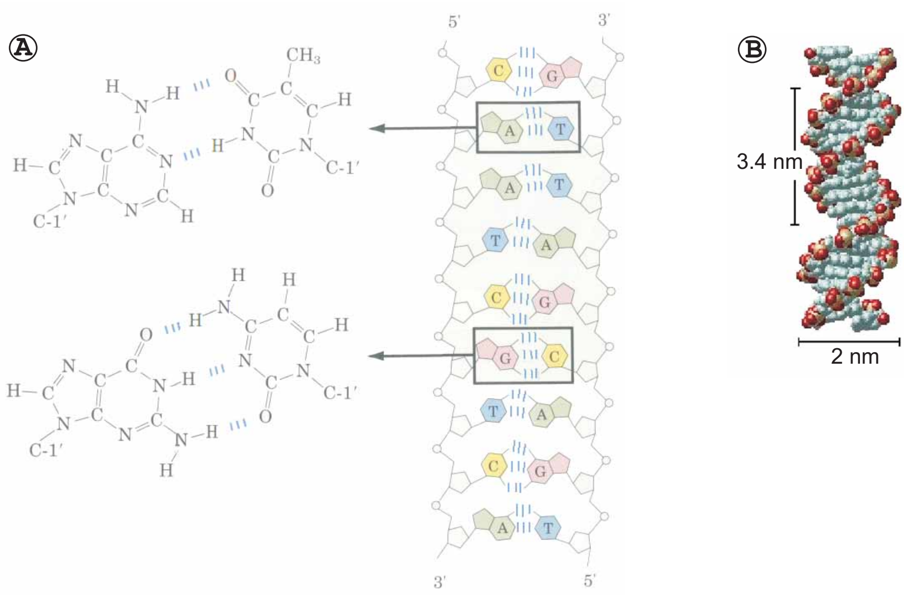

Figure 2.1: B-DNA. A) Stick diagram of the chemical structure of double-helical DNA [8]. Base-paired bases in blue (Thymine T) and green (Adenine A), in red (Guanine G) and yellow (Cytonsine C), and hydrogen bonds between the bases. A zoom shows the specific hydrogen bonds between the base pairs. The covalent backbone structure is indicated by alternating pentose (5 carbons) and phosphate groups (rings). The free hydroxyl group is at the 3' end and the free phosphate group at the 5' end. The orientation of the two strands is antiparallel. B) Model of B-DNA [9].

Chemical structure. The basic monomer unit of double-stranded DNA is the nucleotide. The nucleotide consists of one of four bases (**A**denine, **G**uanine, **T**hymine or **C**ytosine), a sugar, and one or more phosphate groups. For the polymerization of nucleotides to form a single strand of DNA, a 3'-5' phosphodiester bond is built. Two associated nucleotide strands form the structure of a double bounded helix. Not every combination of base pairing is favored. In the Watson-Crick base pairing, A is connected by two hydrogen bonds to T, and G by three hydrogen bonds to C. (Fig. 2.1a). The sugar-phosphate backbone of DNA is characterized by tow negatively charged phosphate groups per base pair (bp) at physiological acidity (pH 7-8). Thus, there are two negative charges per base pair. Using a molar mass of 649 g/mol per bp, 1 ng DNA contains 1.9 $\times 10^{11}$ negative charges.

Physical structure. DNA consists of two complementary strands where the base pairs are oriented inward and the sugar-phosphate backbone is on the outside (Fig. 2.1b). This structure is determined by the fact, that DNA has hydrophobic and hydrophilic residues. While the backbone is hydrophilic, the bases are hydrophobic. Thus, the DNA double-helix is held together by the hydrophobic attraction between adjacent bases and the hydrogen bonding between complementary bases. Overall, The backbone is highly charged and flexible. The most common form of DNA in cells is B-DNA. This form is characterized by a helical right-handed turn every 10 basepairs (bp) where each bp has a hight of 0.338 nm. The diameter of the DNA helix is 2 nm. In addition, DNA might also occur in three different structures called A-, Z- and triple-helical DNA [10] by varying the environmental conditions. Nevertheless B-DNA is far the most important modification and dominant under the conditions used during these studies. In the following, B-DNA will always be referred to as DNA. Otherwise, it will explicitly named differently.

2.1.2 Proteins

There are 20 different essential monomers (amino acids) that are used by nature to construct the biopolymers, called proteins. Only, when the protein is in the correct three-dimensional structure, it is able to function efficiently. The three-dimensional structure of each protein is coded by its amino acid sequence. The 20 amino acids differ only in their side chain (R) (Fig. 2.2) that can be neutral or charged, hydrophobic or hydrophilic, acidic or basic.

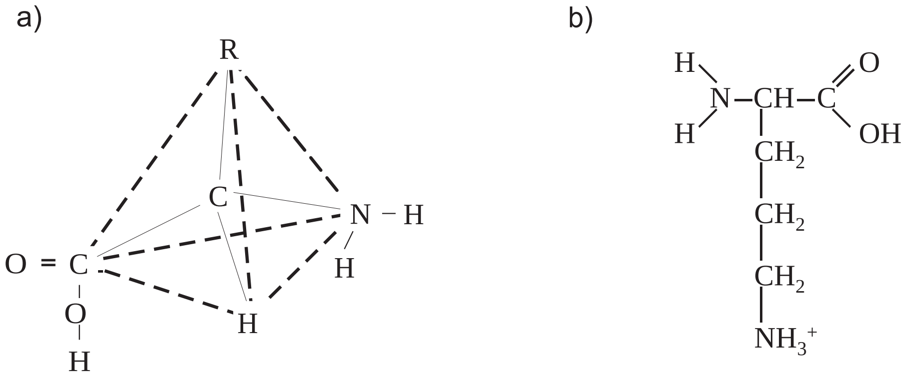

Figure 2.2: Amino acids. a) Amino acids have the form of a tetrahedron with a carbon atom at the center. The four vertices are occupied by a hydrogen atom (H), an amino group (NH_2), an acidic carboxyl group (COOH) and different side chains (R). b) Chemical structure of poly-L-ornithine. Poly-L-ornithine for example is a positively charged amino acid with R equal to -$(CH_2)_3NH_3^+$

.

A protein is a polymer made from amino acids where a covalent bond (peptide bond) between the amino group of one amino acid and the hydroxyl group of another amino acid is formed with the release of a water molecule.

The sequence (*primary structure*) of a protein starts with an amino end (N-terminus) and ends with a carboxyl group (C-terminus). The structure of a protein is largely determined by two driving forces. The first one is the establishment of hydrogen bonds between an oxygen atom of one residue and the C-H or N-H group of another residue. This stabilization leads to what is known as the *secondary structure* of a protein. Two different typical conformations are formed by hydrogen bonding: a helical polypeptide string (α-helix) and a straight polypeptide strand conformation (β-sheet). The second driving force are, hydrophobic interactions which will play a key role for the overall three-dimensional conformation (*tertiary structure*) of the protein.

An enzyme is a special class of proteins which catalyzes a specific reaction necessary for the maintenance of life. Here, special attention is drawn to restriction endonucleases, which are bacterial enzymes that recognize and bind to specific DNA sequences resulting in cleavage of the DNA molecule [11]. This reaction usually involves the aid of a special cofactor. Thousands of different restriction enzymes are known which cut at different sequences corresponding to the recognition site of the enzyme. However, the reaction mechanism of many of these enzymes is not fully understood. An example is the restriction enzyme *Eco*P15I, which cleaves DNA [12], [13].

2.2 Biomacromolecular Interaction

Electrostatics provides the basis in many biomacromolecular interactions. In nature, on the one hand, DNA and other important biopolymers are negatively charged which prevents unwanted complexation between them. On the other hand, oppositely charged biopolymers will interact with each other. This paragraph will focus on cases in which the electrostatic interactions between DNA and an oppositely charged polymer play an important role.

2.2.1 Collapse and Complexation of DNA

The length of DNA increases with the complexity of a species (Fig. 2.3). Almost 2 m DNA has to be stored in a human cell nucleus of about 5 μm in diameter. However, the mechanisms of DNA organization depend on the species. In bacteria, DNA is complexed with positively charged polyamines and proteins into a comparatively simple and random structure, while in eukaryotic cells, i.e. cells that contain a nucleus, DNA is associated with proteins

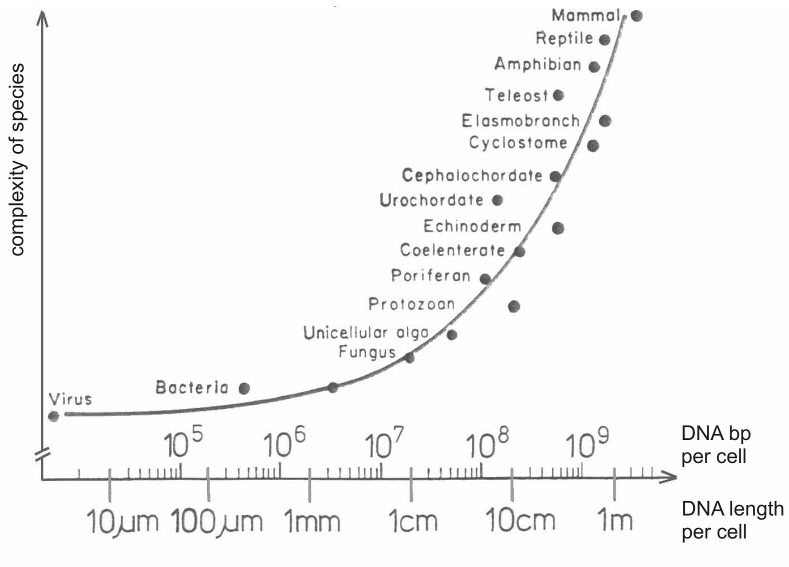

Figure 2.3: Length of DNA of different species [17].

in a highly compact and structured complex called chromatin. The smallest subunit of the chromatin is called the nucleosome core particle. Its structure was already determined by X-ray cystallography in 1997 (Fig. 2.4) [14]. This structure reveals, that 146 bp of DNA wrap around the core histone octamer in 1.65 turns with a pitch of 2.65 nm and a radius of 4.25 nm [15]. The core histone octamer consists of two copies each of histones H2A, H2B, H3, and H4, that are highly positively charged, due to their positively charged terminal regions of the protein. Thus, electrostatic interaction between the core histone octamer and the DNA phosphates occurs. Overall, the nucleosome is negatively charged [16].

Condensation beyond the nucleosome core particle into the chromosome is depicted in Fig 2.5. First, the DNA between two nucleosomes is called the linker segment which gives unfolded chromatin a bead-on-a-string structure. The linker histone H1 binds to the linker DNA and helps to compact the structure further into a 30-nm fibre. Since the arrangement of nucleosomes and linker DNA in the condensed 30-nm fibres has never been fully resolved experimentally, there is no consensus of its internal structure. A variety of models that explain the structure of the complex exist including the solenoid model [18], the crossed-linked model [19], and two-angel model [20]. Nevertheless, it is known that the electrostatic interaction between DNA, histone proteins, as well as free ions play a major role [18], [21], [22]. Furthermore, the structure of the chromatin plays a key role for the transcription and replication mechanism

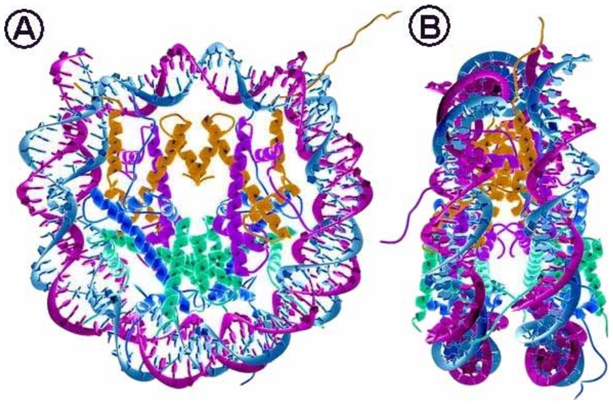

Figure 2.4: Crystal structure of the nucleosome core particle at 2.8 Å resolution. The structure reveals the atomic model [14] in which 146 bp DNA (blue and magenta) are wrapped around the eight histone proteins (yellow: H3, violet: H4, dark blue: H2A, green: H2B). A) The view is down the DNA superhelix axis and in B) perpendicular.

of DNA [23].

Condensation beyond the 30-nm fibre is even less well understood. A model for the packing in the interphase chromosomes is suggested [9], where the 30-nm fibres loop out from extended scaffolds, and finally organize again into a helical configuration as shown in Fig. 2.5.

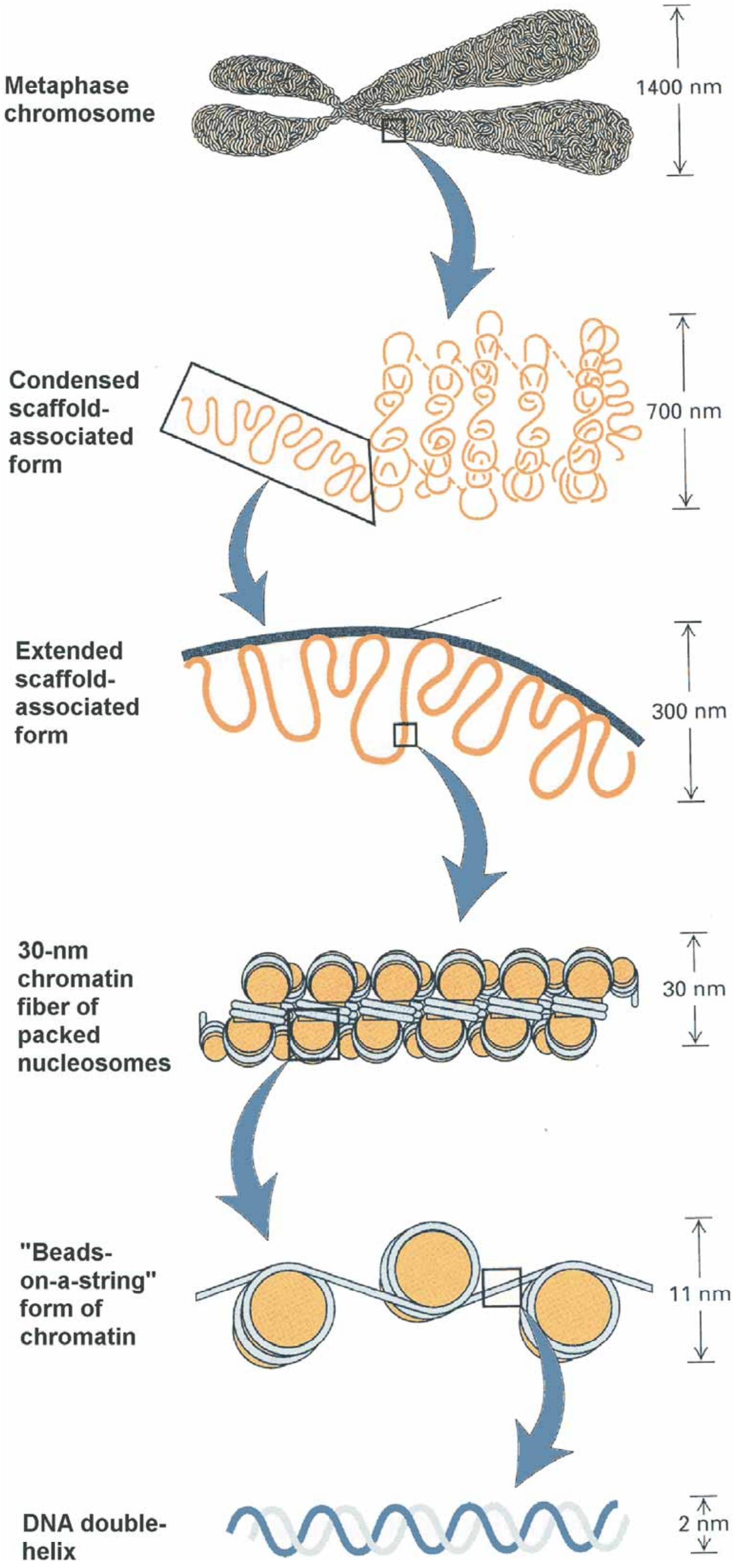

Figure 2.5: Model for packing of chromatin and the chromosome scaffold in metaphase chromosomes [9].

Again, electrostatic effects are known to play a central role not only for the stability of the nucleosome but also in the condensation of the fiber. Thus, the interaction of the nucleosome particles can be studied by varying the salt concentration. Recent studies show that the conformation and interaction of the nucleosome particles change due to the salt concentration [24]. These changes may be related to those causing accessibility of chromosomes to transcription and replication [25] and may be the origin of a dynamic structure model as proposed by Polach and Widom [26]. Interestingly, Kunze and Netz [27] showed numerically that for salt concentrations close to the physiological value (100 mM NaCl), the DNA is tightly wrapped around the histone octamer whereas for high salt concentrations a strongly discontinuous dewrapping occurred. Furthermore, for high salt concentrations DNA is released from the histone octamer [28], [29]. This unwrapping was also proposed by Marky and Manning [30].

In addition, due to the electrostatic charge, DNA tends to form complexes with oppositely charged objects like multivalent cations, polyelectrolytes, colloidal particles, dendrimers, proteins, and even surfactant aggregates like micelles [1]. The morphologies of these complexes are different. DNA molecules condense into toroids and rods in the presence of multivalent cations [31] or polyamines [32], [33], [34] but the resulting structures are not resolved on the molecular level yet. Also in complexes formed with cationic polymers [35], [36], [37], [38], [39], and cationic dendrimers [40], [41], [42], the molecular structure of these so called polyplexes remains unclear, while X-ray diffraction on complexes formed from DNA and cationic lipids (lipoplexes) reveals multilammellar structures [43].

Most of the synthetic cationic agents forming these complexes and aggregates are developed for potential use as DNA carriers (vectors) in novel gene therapies. The precise nature of the complexes depends on physicochemical parameters like charge density, radii and flexibility of the interacting molecules as well as the ionic strength and temperature of the surrounding medium.

2.2.2 Gene-Transfection

Transfection is the introduction of foreign DNA into the nuclei of eukaryotic cells [44]. There are different kinds of techniques for transfecting cells. Here, the focus is on the carrier mediated transfection method also called nonviral gene delivery method. Although viral-based gene delivery is currently the most efficient way for transfection, many studies show alternatives of nonviral gene delivery systems [45], which overcome disadvantages of viral-based gene

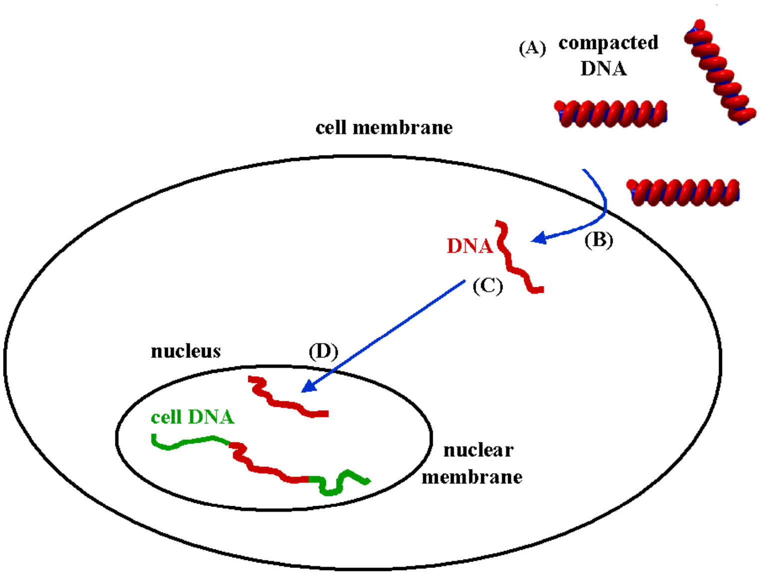

Figure 2.6: Model of transfection mechanism. (A) Compacted DNA. (B) Bypass the membrane barrier by either endocytosis, fusion with, or forced disruption of the membrane. (C) Release from the endosome. (D) Entering the nucleus.

delivery systems such as immunological response, fatal infections or DNA restriction. In nonviral gene delivery systems, the DNA is compacted by cationic agents like dendrimers or surfactants as mentioned above, to protect it from enzymatic attack. A schematic overview of this nonviral gene delivery method is given in Fig. 2.6.

The goal of nonviral gene delivery is to deliver the DNA both efficiently and selectively to a given cell type [45]. A well known promising example for such an agent is the spherical poly(amidoamine) (PAMAM) dendrimer [46]. Recent studies report on efficient gene transfer using this dendrimer [47], [48]. Furthermore, the structure of its complex with DNA can influence the in vivo interactions with the biological material and therefore affect the efficiency of transfection, which depends in particular on structure, size and charge density of the dendrimers [4]. But again, the structure of this self-assembled nonviral gene delivery system is not well understood [49].

In addition, other examples for efficient nonviral gene transfection are cationic surfactants [50], [51] and even more pronounced Gemini surfactants (see also section 2.3.3).

2.2.3 DNA/Protein Interaction

Although DNA/protein interaction is mainly specific, the underlying process of quickly finding the special site for the protein on the DNA is often dominated by long-range electrostatic forces. In the electrostatically nonspecific complex the protein slides along the DNA to its final specific side. This sliding model has been proposed for several enzymes like the restriction enzyme *Bam*HI [11] and the tumor suppressor protein p53 [52].

As an example for the studies of DNA/protein interaction, in a cooperation with S. Reich (Institute of Virology, Group of Dr. Reuter, Humboldt University Medical School (Charité), Berlin, Germany), the interaction of the restriction enzyme *Eco*P15I [12] was investigated using SFM. It could be shown that *Eco*P15I binds specifically to the DNA molecule and forms loops in order to cleave it [53]. Fig. 2.7 shows stages of different DNA/*Eco*P15I complexes.

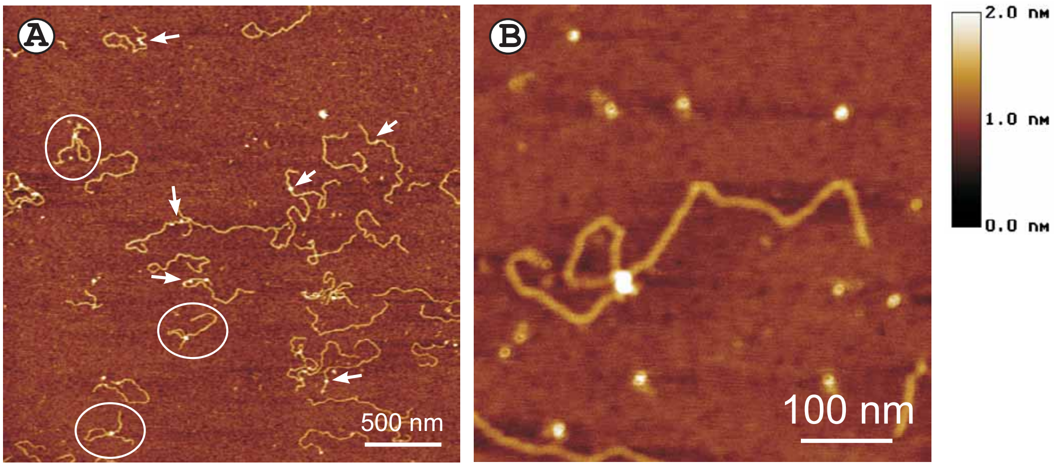

Figure 2.7: SFM study of DNA/*Eco*P15I interaction. A) Specific binding of *Eco*P15I to DNA molecules (indicated by arrows) and induced loop formation of the DNA molecule by the DNA/*Eco*P15I interaction (circles). B) High resolution image of the induced loop formation. The *Eco*P15I is placed on top of the DNA crossing [53].

2.3 Synthetic Polyelectrolytes

The chemically synthesized polyelectrolytes that are used in this thesis are dendronized polymers, which combine the properties of dendrimers and polymers. On the one hand, according to the unique architecture of dendrimers they posses a high molar mass [54] and rigidity [55] (section 2.3.1). On the other hand, their terminal groups can be easily functionalized with charges [56]. Polymers that contain charges are called polyectrolytes and are introduced in sections 2.3.2 and 2.3.3.

2.3.1 Dendrimers

During the last 10-15 years dendrimer chemistry was one of the most rapidly expanding areas in chemistry. Dendrimers belong to a special kind of macromolecules which posses a highly ordered structure (Fig. 2.8). The name *dendrimer* comes from the two words: *dendron* and *meros*. *Dendron* (Greek: tree, tree-like structure) evokes the highly branched structure of these macromolecules, and *meros* (Greek: part) the unit repitition. For increasing dendron generation steric effects lead to a sphere shaped molecule. Dendrimers allow the precise control of size, shape, and placement of functional groups [54].

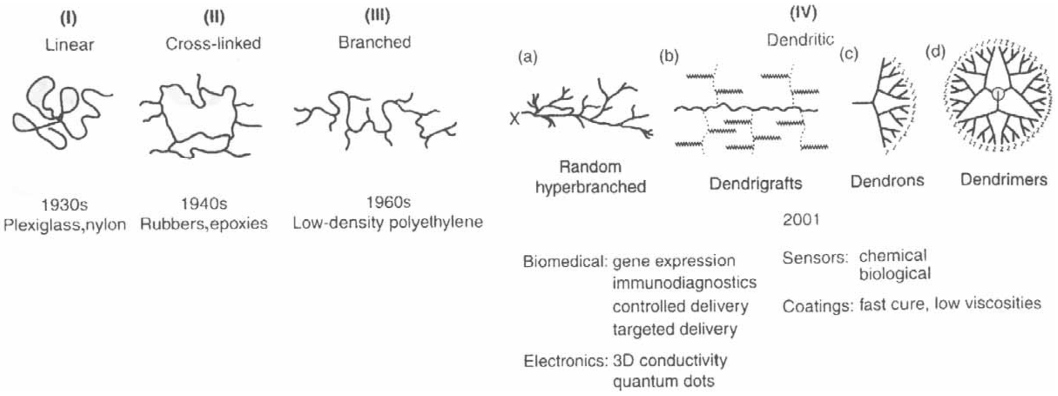

Figure 2.8: Classes of macromolecular architecture [57].

Due to the architecture, dendrimers of higher generations have molar masses up to the millions, while their molar mass distribution is very narrow [58]. On the one hand, the highly branched nature results in a large number of chain ends which can be modified chemically. On the other hand, the sphere´s interior which is shielded from the exterior environment can be used for different applications. Due to these possibilities, dendrimers are of interest in many fields of application like molar mass and size standards, molecular containers, gene transfection agents (see section 2.2.2) or catalytic agents. Especially because of their closed contour and size they match to many proteins and bioassemblies (Fig. 2.9). In life science, one of the most promising areas for the application of dendrimers are as carriers in drug and gene delivery systems.

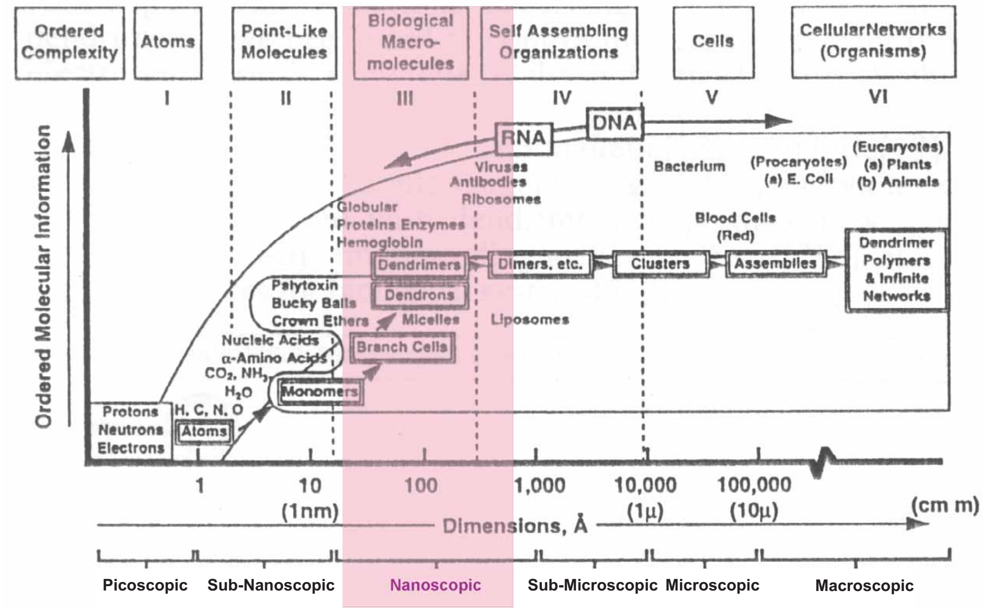

Figure 2.9: Dimensional hierarchy of organic matter [59].

Although the dendritic structure of dendrimers suggests a radial distribution, an increasing number of generation (G) will lead to strong sterical interaction especially of the end groups. While the number of end groups increases exponentially ($\sim 2^{G+1}$), the surface area only increases with the square of generation ($\sim G^2$) and the volume of the dendrimer with $\sim G^3$. Nevertheless, there exists some controversy in the literature concerning the radial density distribution of such dendrimers. While in an analytical calculation by de Gennes and Hervet [60] a minimum of the density profile in the center is predicted. More recent theories using both Monte Carlo and molecular dynamics simulation as well as a self-consistent mean field model report on density profiles with a maximum in the center [61]. The latter predictions are confirmed by experimental results by small-angle neutron scattering [62]. Here, the amount of backfolding increases with the number of generations. Of course these findings and theories depend strongly on the solvents and on the kind of dendrimers and models they used like long flexible spacers versus stiff spacers, solvent properties, electrostatic repulsion, and dendron generation.

2.3.2 Dendronized Polymers

Dendronized polymers (Fig. 2.10) are a new class of polymers which possess similar unique features as spherical dendrimers but appear in a cylindrical

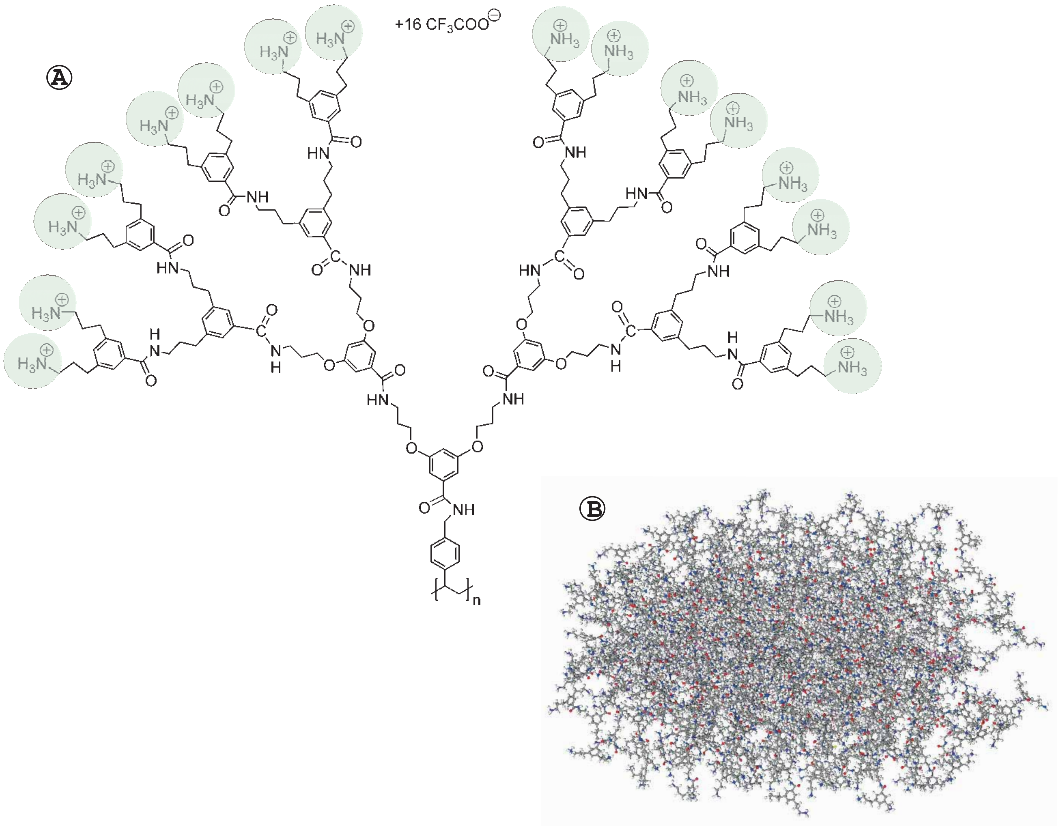

Figure 2.10: PG4. A) Chemical structure of a repeat unit of fourth generation dendronized polymers (PG4). B) Bulkiness of a PG4, generated by MD simulation (PCFF). Colour code: (H:white), (C:grey), (N:blue), (O:red), (backbone:purple).

rather than spherical shape.

To obtain this kind of structure, the inner focal initiator point is replaced by a linear backbone. From this linear backbone side chains being dendrons go off (Fig. 2.10). One unique property of these dendronized polymers is the stiffening of the backbone caused by steric repulsion between the dendrons. The stiffness of polymers can be characterized by the persistence length (section 2.6.2). The dendritic layer around the backbone results in a cylindric shape of the polymer [63]. The synthesis of the dendronized polymers of high molar mass which were used in these experiments, was carried out by Shu et al. [64]. The repeat units of the polymers are styrenes functionalized with dendrons carrying protonated amine groups at the periphery. In addition to the steric repulsion of the dendrons, also the electrostatic repulsion of the end groups might enhance the stiffening of the polymer backbone. In Fig. 2.10a the repeat unit of a fourth generation dendronized polymer (PG4) is given and

Fig. 2.10b shows the bulkiness of a PG4 in a molecular minimization simulation of 80 repeat units, i.e. 22122 atoms with a total number of 5000 iterations, using the DISCOVER Molecular Simulation Program, Materials Studio^{TM} [65]. All minimization simulations used a Polymer Consistent Force-Field (PCFF) (InsightII package) that is intended to be used for the simulation of polymers.

Dendronized polymers with functionalized surfaces for chemical modification can be inverstigated on solid substrates by scanning force microscopy (SFM). For example alkylated fourth generation dendronized polymers are shape resistent while moving the polymer with the SFM tip across a surface [5]. Such experiments lead to a bottom-up approach for a molecule based nanotechnology. Another promising experiment uses dendronized polymers with end groups of azide active ester. The intermolecular connection induced by UV-C light is proven by mechanically challenging the connected molecules with an SFM tip. A breakage at the junction did not take place [66]. However, the potential of dendronized polymers in biomedical application remains to be explored.

2.3.3 Gemini Surfactant

In contrast to conventional surfactants with one single hydrocarbon tail connected to an ionic or polar headgroup, a gemini surfactant consists of at least two tails Fig. 2.11a, [67].

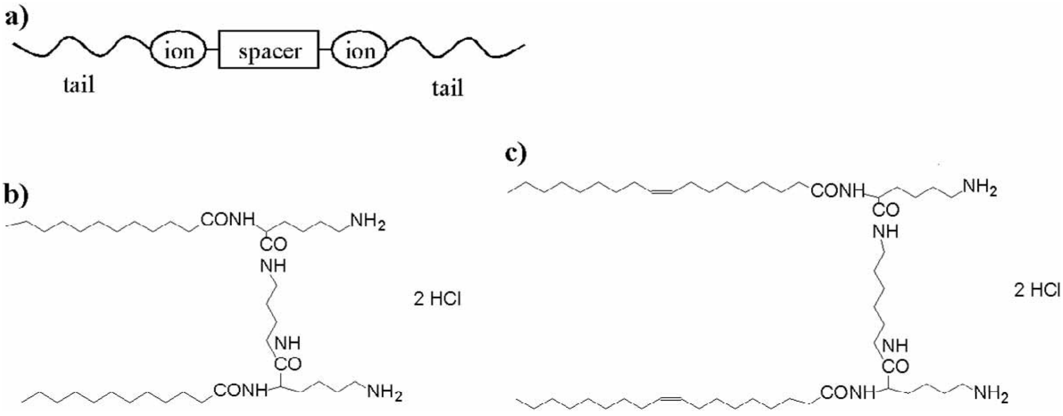

Figure 2.11: Gemini surfactant. a) Schematic structure of the gemini surfactant. b) Chemical structure of GSN11 and c) GSN14.

The gemini surfactants used in this project were synthesized by the group of Prof. M. C. Feiters, Nijmegen, Netherlands. Both, GSN11 and GSN14 are positively charged molecules due to their two amine headgroups (Fig. 2.11b,c).

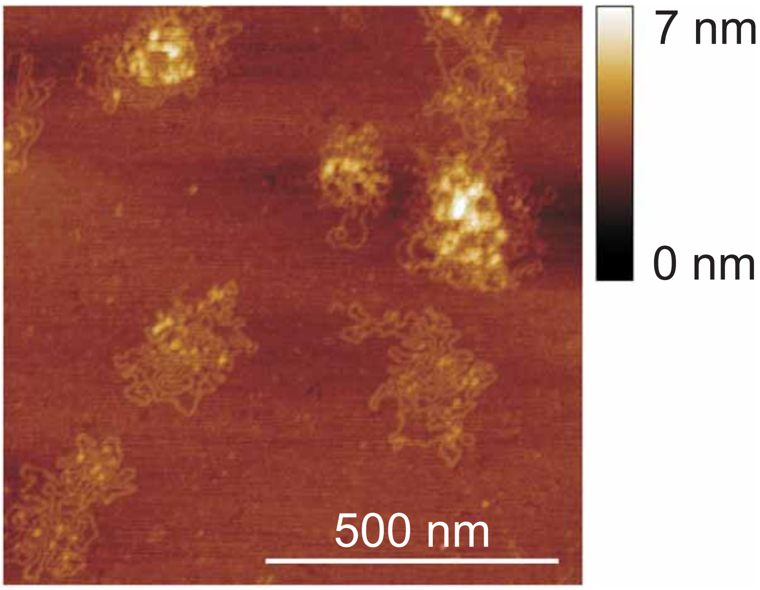

Figure 2.12: SFM on Gemini surfactant/DNA complexes of charge ratio (1:1) on poly-L-ornithine coated mica. GSN14/DNA complex, very high transfection efficency.

2.4 Polyelectrolyte Complexes

Polyelectrolyte complexes are formed by oppositely charged polyelectrolytes. Aside from the biological and medical aspects (section 2.2), the molecular structure of polyelectrolyte complexes may be used to improve our general understanding of polyelectrolyte interactions. Moreover, during the last years, polyelectrolyte complexes have demonstrated an enormous potential for technological applications, like paper production, purification processes, and producing pigment coating [68].

One example of polyelectrolyte complexes which have been already used for gene transfection (section 2.2.2) were investigated in a cooperation with Prof. M. C. Feiters, Nijmegen, Netherlands. They showed that complexes of DNA formed with GSN11 and GSN14 (Fig. 2.11b, c) are very little and very highly efficient, respectively, for non-viral gene transfection systems. The morphologies of the complexes were examined by SFM and vary depending on the gemini surfactant used. The comparison between the complex structure and their gene transfection efficiency lead to the conclusion that the globular complex of GSN14/DNA (Fig. 2.12) lead to a successful transfection, whereas rodlike and highly compacted morphologies of GSN11/DNA complexes (Fig. 2.13) characterize poor transfection efficiency.

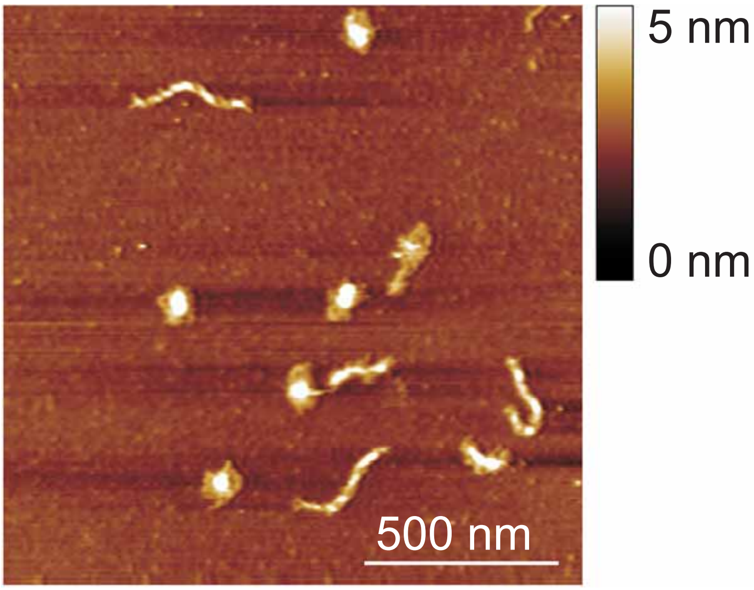

Figure 2.13: SFM on Gemini surfactant/DNA complexes of charge ratio (1:1) on poly-L-ornithine coated mica. GSN11/DNA complex, very low transfection efficency.

In addition, polyelectrolyte adsorption on charged, flat surfaces or spheres (i.e. layer-by-layer adsorption [69]) has been a focus in experimental and theoretical studies [70], [71]. Also theoretical models of the structure of complexes formed between a stiff charged cylinder and oppositely charged flexible or semiflexible polymers have been investigated [72], [73]. However, it remains a challenge to deduce the molecular structure of single polyelectrolyte complexes experimentally [74].

2.5 Scanning Force Microscope (SFM)

The SFM, also known as the atomic force microscopy, belongs to the family of scanning probe microscopies (SPM). The SPM technique relies on mechanically scanning a sharp tip over a sample surface to sense different types of interaction with the surface. The SFM was invented in 1986 by G. Binnig, C. F. Quate and Ch. Gerber [75]. Here, a three-dimensional profile with nanometer resolution can be imaged by measuring the forces acting between a tip and the sample (see section 2.5.1). The tip is mounted to a spring like cantilever that obeys Hook's law. Its displacement is detected by a deflection beam at the cantilever surface (optical method) [76]. Unlike the case of scanning tunneling microscope (STM) (Nobel Prize in Physics in 1986 by G. Binnig and

H. Rohrer), also insulating samples can be imaged. Furthermore, imaging is possible with the tip immersed in fluid [77]. These advantages led the SFM up to the present state-of-the-art instrument for electrochemistry, surface science, and biology (see section 2.5.7). Currently, increasingly effort has been put into the development of SFM used for cantilever-based sensors of chemical and biological reaction [78], force measurements [79], also for new high density storage [80], and quantum dot fabrication devices [81]. Another promising combination which can be achieved by SFM is the visualization and manipulation of single macromolecules on a surface [5], a crucial step for molecular nanotechnology [66].

2.5.1 Classification of Forces

The physical basis for SFM is the detection of interatomic forces, i.e. ideally between tip-atom and surface-atom. The forces can be classified into *short range* like interatomic repulsion and friction and *long range* forces like van der Waals, capillary, electrostatic forces. A detailed overview on intermolecular forces is given in the book of J. Israelachvili [82]. Here, the most relevant forces for SFM operation are selected:

Interatomic Repulsion. At interatomic distances that are smaller than the equilibrium distance of two atoms, the electron clouds overlap. This leads to incomplete screening of the charges of the nuclei and Coulomb repulsion occurs. The repulsive potential can be described by a power law $U(z) \propto (1/z)^n$, where $n > 9$, or by an exponential. Here, z is the intermolecular distance.

Capillary. Depending on the relative humidity as well as the physico-chemical nature of the samples water can condense on the surface and forms a water layer. Consequently, a miniscus is formed between the tip and the sample. At ambient humidity, this effect begins at a sample/surface separation of 10-200 nm.

Electrostatic. Electrostatic forces due to coulombic interaction are relevant over a few to thousands Ångströms. They can either be attractive or repulsive depending on the materials.

Van der Waals. Van der Waals forces are significant for distances of a few to a few hundred Ångströms. The most important contribution to the long-range van der Waals force is the dispersion force, which is always present between two polarizable atoms. Furthermore, between polar molecules two additional types of forces contribute to the van der Waals force: the induction force and the orientation force. Thus, the van der Waals potential can be written as $U_{VDW} = -[C_{ind} + C_{orient} + C_{disp}]/z^6 = -C_{VDW}/z^6$. Here, C_{VDW} stands for the energy coefficients and z is the intermolecular distance.

The total intermolecular pair potential is obtained by summing the attractive and repulsive potentials. A special kind of the total intermolecular pair potentials is the Lennard-Jones potential $U_{LJ}(z) = C_1/z^{12} - C_{VDW}/z^6$, drawn in Fig. 2.14. The parameters C_1 and C_{VDW} depend on the interacting particles. For the interaction of two atoms they are: $C_1 = 10^{-134}$ Jm^{12} and $C_{VDW} = 10^{-77}$ Jm^6 [82]. The first term of the Lennard-Jones potential describes the repulsive ion-ion potential and the second term the attractive van der Waals potential. The force is given by $F = -dU_{LJ}(z)/dz$ and also depicted in Fig. 2.14.

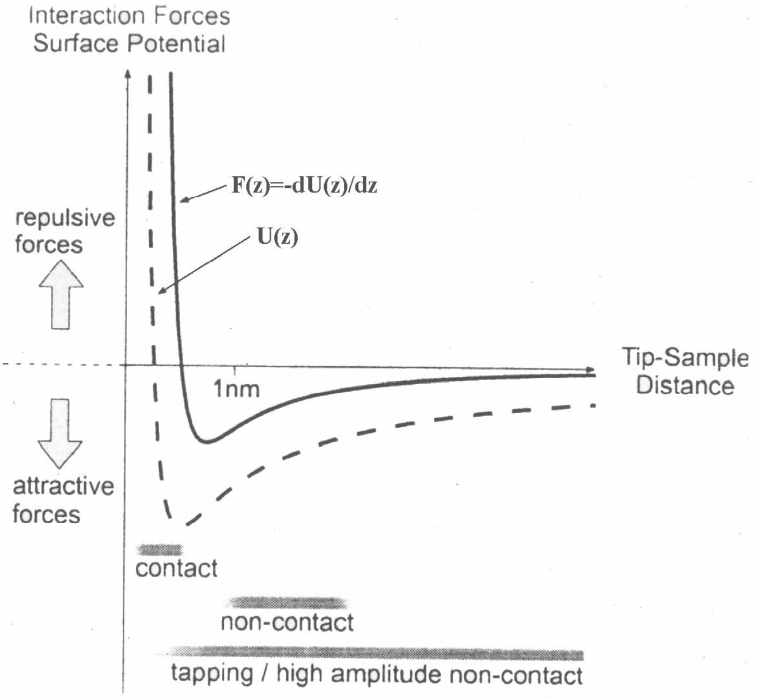

Figure 2.14: Lennard-Jones potential. Energy and force between the atoms as function of their separation [83]. The distances correspond to the different SFM modi that are described in section 2.5.3.

2.5.2 Setup of the SFM Apparatus

Fig. 2.15 gives an overview of the working principle of the scanning force microscope (SFM).

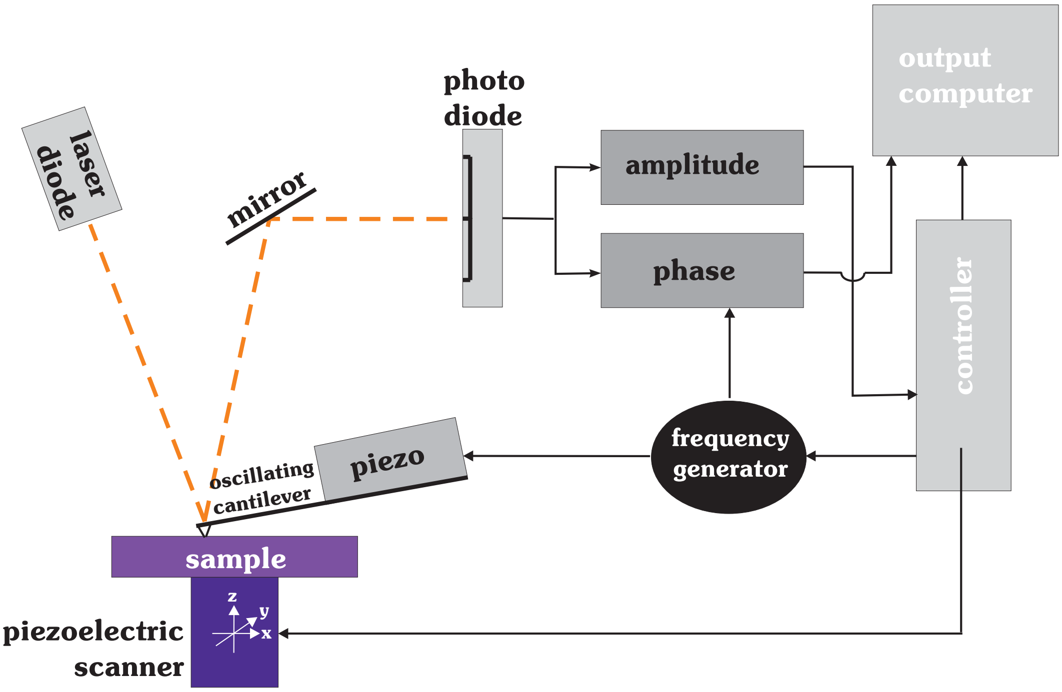

Figure 2.15: Setup of the SFM.

The tip mounted on top of the cantilever is fixed in close proximity to the sample surface to probe the interaction forces between tip and sample. The force acting on the tip will cause the cantilever to bend, according to Hook's law $F = k\Delta z$, where k is the spring constant and Δz the vertical displacement of the cantilever. The movement of the cantilever Δz is recorded by the reflecting laser beam at the back of the cantilever by a 4-segment photo diode (*Beam Deflection* Detection). Thus, by measuring these deflection one can infer the interaction force and therefore also the distance between tip and sample.

Under the tip, the sample is glued to a magnetic sample holder and mounted onto a three-dimensional piezoelectric scanner, i.e. the x,y,z scanner. When a homogeneous sample surface is scanned in x and y direction, the tip deflection is the result of the changes in the z-direction, i.e. the topography. The measured signal from the photo diode is sent to the computer and a feedback loop modulates the position in z direction of the sample to keep the force acting on the tip at a constant level (*constant force mode*).

2.5.3 Operation Modes of SFM

The SFM can be operated in different modes. The three main classes are *contact mode, non-contact mode* and *tapping mode.*

Contact mode. The basic mode of SFM operation is contact mode, in which the topographical image is deduced from the deflection of the cantilever as the tip scans the sample while maintaining in contact with its surface and thus, in the repulsive regime of the Lennard-Jones potential (Fig. 2.14). This operation mode can be very destructive due to the lateral forces applied by the tip to the sample. Molecules can be dragged along the surface or even cut during scanning. Of course this manipulation can be used on purpose [66]. However, for imaging, this problem can be overcome by reducing the tip sample interaction, i.e. by using non-contact or tapping mode, or by operation in a fluid cell.

Tapping mode. In the tapping mode, also known as intermittent-contact mode, the cantilever oscillates close to its resonance frequency and the tip taps the surface only periodically [84]. Thus, it operates for a short fraction of its vibration period in the repulsive regime but most of the time in the attractive regime of the Lennard-Jones potential (Fig. 2.14).

The cantilever motion can be described by an oscillator in a non-linear potential with damping and the equation of motion of the cantilever is given by

$$m_e \ddot{z} + \alpha \dot{z} + kz + F(z) = F_0 \sin(\omega t), \tag{2.1}$$

with m_e the effective mass, α the damping constant, k the spring constant, F_0 drive amplitude, ω drive frequency, and $F(z)$ is the sum of repulsive and attractive forces acting between tip and sample [85], [86].

One advantage of tapping mode SFM is that lateral forces are significantly reduced. The reduction of the lateral forces as well as the periodical contact with the surface enables imaging of soft samples and with high resolution simultaneously. Thus, this is the most commonly used mode for biological specimens and also used in the experiments described in this thesis.

The tapping mode also enables to measure the phase between the driving oscillator of the cantilever and the actual cantilever oscillations. The phase imaging may provide information on surface properties like stiffness [87], [88].

Non-contact mode. In this mode the cantilever oscillates close to its resonance frequency but with a smaller amplitude compared to tapping mode. The swing of the amplitude is so small that the tip is always operating in the attractive regime of the Lennard-Jones potential (Fig. 2.14). The advantage of this mode is the very small disturbance of the sample by the tip. On the other hand, the resolution is limited and the tip can be easily caught by adhesion forces, e.g. due to a water layer on the sample.

Cantilever. A crucial component of the SFM for the different operation modes is the cantilever. In order to detect low forces (0.1 nN) the spring constant of the cantilever should be as low as possible to obtain a large displacement of the cantilever. On the other hand, its resonance frequency should be high enough (10-300 kHz) to minimize the influence of background noise like vibrations of the building ($\sim$ 100 Hz). In addition, background vibrations are damped by placing the SFM apparatus onto a granite plate that hangs on soft bungee cords. This suspension has for the set-up used for this thesis a resonance frequency for vertical and pendulum oscillations below 0.5 Hz [89].

2.5.4 Tapping Mode in Liquids

There are many advantages to operate the SFM while the tip is immersed in fluid. For example, the elimination of adhesion forces, and minimization of friction and van der Waals forces [90] as well as the ability to study technological or biological processes at liquid solid interfaces in vivo (see section 2.5.7). For tapping mode operation in solution the cantilever is excited through oscillations of the entire glass fluid cell via a piezoelectric ceramic. Thus, the inertial mass of the liquid leads to a large damping of the oscillation of the resonance frequency of the cantilever. In addition, due to acoustic resonances of the fluid cell a lot more resonances can be seen in the frequency spectrum.

For operation, the cantilever is totally immersed in the fluid. The fluid cell is used either with or without O-ring (Fig. 2.16). The O-ring is a O-shaped rubber ring used to seal the fluid in the fluid cell as depicted in Fig. 2.16a. In this case, a defined volume is captured between sample, O-ring, and fluid cell, that can be easily exchanged using the ports of the fluid cell. In the latter case, the liquid is held in place by the miniscus between fluid cell and sample. To avoid air bubbles in the fluid cell, it is easier to mount the fluid cell without the O-ring.

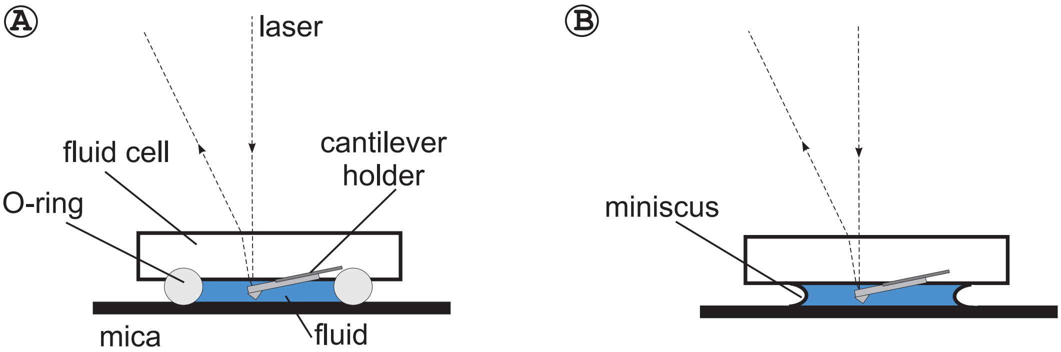

Figure 2.16: Model of the fluid cell. The cantilever is totally immersed in the fluid. A) with O-ring B) without O-ring.

2.5.5 Q-Control

In order to improve the conditions of scanning soft and loosely bound samples in tapping mode SFM, the interacting forces between tip and sample should be as small as possible. Furthermore, the lateral resolution of soft samples also depends on the forces exerted on the sample. A recent development, called Q-Control, promises high sensitivity in tapping mode SFM and thus, smaller interaction forces due to the reduction of the damping of the dynamic system. This is achieved by an increase of the effective quality factor Q_{eff} of the resonance curve.

Definition of $\mathbf{Q_{eff}}$. The resonance curve of the cantilever can be characterized by its quality factor $Q_{eff} = \omega_0/\Delta\omega$. Here, ω_0 is the resonance frequency and $\Delta\omega$ is the width of the resonance curve.

To understand the operation of the Q-Control, following mechanisms of the tip-sample interaction have to be considered:
While the tip approaches the surface (distance z), attractive interaction forces lead to a decrease of the effective spring constant k_{eff}, because of $k_{eff}(z) = k + d^2U/dz^2$ [91]. This results in a shift of the resonance curve to lower frequencies since $\omega = \sqrt{k/m}$. Thus, if the cantilever is oscillating at its resonance frequency the amplitude decreases and therefore the average tip-sample distance increases. Simultaneously, on the other hand, the tip approaches the surface due to the feedback loop. The tip starts tapping the surface, when the decrease of the amplitude is compensated by the smaller tip-sample distance. This indicates the transition from the attractive to the repulsive part and determines the onset of the intermittent regime (Fig. 2.14). This onset depends on the strength of the derivative of the attractive forces (i.e. $d^2U/dz^2 = dF/dz$)

and the slope of the resonance curve, i.e. the quality factor Q_{eff}. Thus, for equal derivatives of attractive forces, the onset of the intermittent regime can be delayed or even suppressed by increasing the quality factor Q_{eff}. The SFM can even continuously be operated in the regime of net-attractive interaction forces [92].

Experimentally, the increase in the quality factor can be realized by an additional feedback circuit, called Q-Control. This additional feedback circuit amplifies, phase shifts, and then feeds the cantilever signal back into the cantilever excitation. This can be realized by adjusting an additional phase shift of $\phi = \pm\pi/2$ to the system. Thus, the equation of motion (2.1) can be rewritten as

$$m\ddot{z}(t) + \alpha\dot{z}(t) + kz(t) + F(z) = F_0 \sin(\omega t) + Ge^{\pm i\frac{\pi}{2}} z(t), \tag{2.2}$$

assuming a stable cantilever motion ($z(t) \approx F_0 e^{i(\omega t - \varphi)}$).

Furthermore, by using $e^{\pm i\pi/2} z(t) = \pm\dot{z}(t)/\omega$ as well as $\alpha_{eff} = \alpha \pm G/\omega$, (2.2) becomes

$$m\ddot{z}(t) + \alpha_{eff}\dot{z}(t) + kz(t) + F(z) = F_0 \sin(\omega t). \tag{2.3}$$

Thus, this circuit can be used to adjust the effective damping α_{eff} of the system, in order to increase the quality factor $Q_{eff} = m\omega_0/\alpha_{eff}$ i.e. an increased slope of the resonance curve of the cantilever [92].

Promising results are obtained for using Q-Control in liquids. The two main limitations of tapping in liquids are on the one hand the detection of the main resonance frequency of the cantilever from the frequency spectra due to frequency modes of the fluid cell geometry. On the other hand there is the low quality factor due to damping. To overcome these limitations, Q-Control can be used successfully to increase the quality factor and thus, amplify the resonance of the cantilever as well as decrease the forces [93].

2.5.6 Tip-Sample Interaction Effects

Height measurements. After calibration of the SFM in z direction, height measurements should be very precise. However, tip-sample interactions cannot be neglected. Height reduction was observed for biomolecules such as DNA [94] as well as synthetic molecules [95]. Here, the height reduction is attributed to the compression of the soft materials by the tip, i.e. tip indentation [96]. It is also known, that humidity influences height measurements due to adhesion [97] or swelling of the molecules [98].

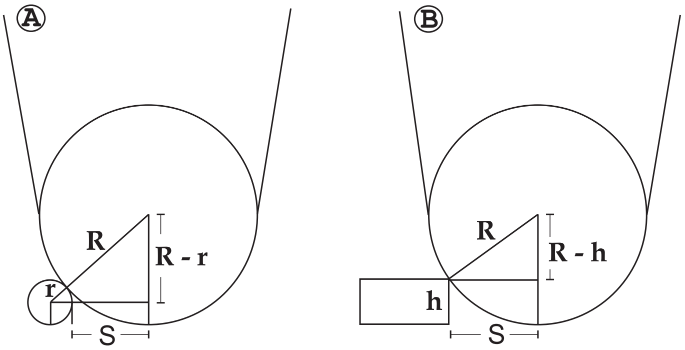

Figure 2.17: Geometrical models for tip broadening. R is the tip radius. A) Sample approximated as a sphere with radius r and B) as a rectangle of height h. The effective broadening $2S$ results in Eq. (2.4) and Eq. (2.5), respectively.

Geometric Tip Effect. In the case of particles with radii smaller than the radius of the tip, only the tip itself determines the diameter of the particles [99], [100]. Assuming a spherical tip ($R = 7.5$ nm [101]) the broadening S can be calculated depending on the geometry of the sample to be

$$2S = 2\sqrt{r(2R - r)} - r. \tag{2.4}$$

$$2S = 2\sqrt{h(2R - h)}. \tag{2.5}$$

R is the radius of the tip and r and h the radius and height of the particle, respectively (Fig. 2.17).

2.5.7 Applications in Biology

The high potential of SFM in biology is due to the combination of high resolution imaging of single molecules as well as the ability to image samples in aqueous conditions [102]. Thus, SFM opens a new approach to study biological structures and processes on a nanometer scale [103], [104]. For example, protein-DNA interactions [105] as well as enzyme activity [106] have been imaged successfully.

2.6 Chemical and Physical Properties of Polyelectrolytes

Polyelectrolytes (PE) are a special class of polymers containing electrostatic charges along their chain. Due to their charges, PEs are water soluble and therefore PEs become of fundamental interest for applications in industry and biology. Interestingly, most biopolymers like DNA and proteins are PEs.

In addition, the PEs that are introduced in this thesis in chapter 3, are rather semiflexible in contrast to most synthetic, flexible polymers. Here, semiflexible polymers characterize polymers between rigid rods and flexible chains. Thus, the models that are introduces in the following sections describe the interactions of semi-flexible charged polymers.

2.6.1 Molecular Contour Length Distribution

One major parameter to characterize a polymer is its degree of of polymerization, that denotes the number of repeat units in a polymer. Depending on the kind of synthesis, the polymer may or may not be monodispers, i.e. all molecules may or may not possess the same degree of polymerization. The polydispersity can be described by the distribution of the degree of polymerization.

Since a polymer chain with i repeat units has a degree of polymerization of i and a molar mass of M_i, it can also be defined using its contour length l_{C_i}. The number of molecules of size l_{C_i} is denoted by N_i.

Averages[107]. The number average molecular length $< L_n >$ is given by

$$< L_n >= \frac{\sum N_i l_{C_i}}{\sum N_i}, \tag{2.6}$$

whereas the weight(mass) average molecular length $< L_w >$ is defined by

$$< L_w >= \frac{\sum N_i l_{C_i}^2}{\sum N_i l_{C_i}}. \tag{2.7}$$

The polydispersity PD is defined as

$$PD = \frac{< L_w >}{< L_n >}. \tag{2.8}$$

These length averages can now easily be transformed into weight averages using the molar Mass M_i and length of a repeat unit a of the polymer in order to get:

$$W_{w,n} = \frac{L_{w,n}}{a} M_i. \tag{2.9}$$

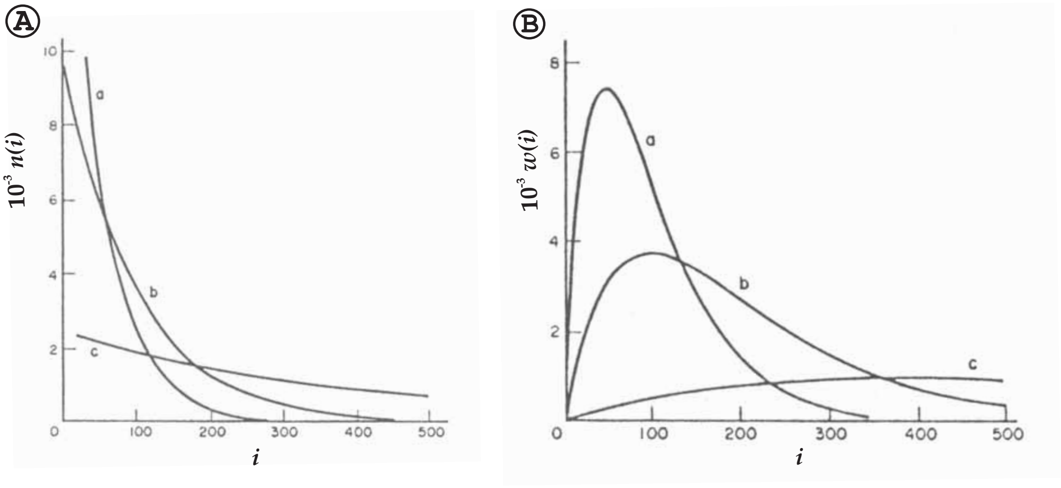

Figure 2.18: Schulz-Flory distributions of chain lengths for polymers a) $\bar{i} = 50$, b) $\bar{i} = 100$, c) $\bar{i} = 400$: A) Number distribution $n(i)$, B) weight (mass) distribution $w(i)$ [107].

Distributions[107]. The molar mass distribution of polymers is described in the case of radical polymerization synthesis by the Schulz-Flory also known as the *most probable* distribution. The number distribution is defined by Eq. (2.10) and the weight (mass) distribution by Eq. (2.11) [107], [108].

$$n(i) = \gamma^{(i-1)} \ln \gamma, \tag{2.10}$$

$$w(i) = i\gamma^{(i-1)} (\ln \gamma)^2, \tag{2.11}$$

where, γ defines the probability of propagation and i the degree of polymerization. If the repeat unit a of the polymer is known, the degree of polymerization i will be directly proportional to the contour length of the polymer $l_C = ai$. Therefore a chain of i units must propagate exactly $(i-1)$ times. In most of the textbooks, the expression $(\ln \gamma)$ is Taylor expanded to $(1-\gamma)$ [34].

The number distribution $n(i)$ and the weight (mass) distribution $w(i)$ of different chain lengths for polymers are displayed in Fig. 2.18.

2.6.2 Statistical Chain Parameters

The worm-like chain (WLC) model, also referred to as Kratky-Porod model describes semiflexible polymers like DNA. A characteristic quantity in this model is the persistence length. It determines the stiffness of the chain and is defined as the distance over which the memory of the initial orientation of the polymer persists [58]. The bare or intrinsic persistence length (l_0) due to monomer structure and non-electrostatic interactions of the polymer is defined

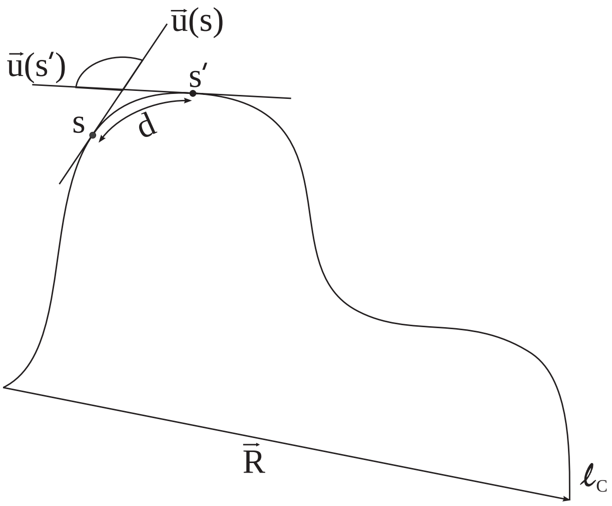

Figure 2.19: Sketch of a worm-like chain. Their contour length l_C, unit vectors $\vec{u}(s), \vec{u}(s')$ tangental to the chain at position s, s', bend angle τ between unit vectors $\vec{u}(s), \vec{u}(s')$, and end-to-end vector $\vec{R}$ are indicated.

as [58]:

$$l_0 = \frac{d}{1 + \cos\tau} \tag{2.12}$$

d is the segment length between s and s', τ the angle between two adjacent unit vectors tangential to the chain at position s and s' (see Fig. 2.19).

However, in the case of PEs, the persistence length is increased due to electrostatic repulsion between monomers. Thus, the theoretical description of the persistence length should include this effect. This leads to an additional contribution to the persistence length, the electrostatic persistence length l_{OSF} due to intrachain repulsion [109]. Thus, the effective persistence length l_{eff} is given by

$$l_{eff} \cong l_0 + l_{OSF}. \tag{2.13}$$

The index OSF stands for the theoreticians Odijk, Skolnick, Fixman who derived the electrostatic persistence length l_{OSF} for a monovalent salt [109], [110]

$$l_{OSF} = l_B \tau^2/(4\kappa^2) \tag{2.14}$$

with the line charge density τ, the Debye screening length κ^{-1}, and the Bjerrum length l_B. The latter parameters are discussed later in subsection 2.7.2. For high salt concentration the bare or intrinsic persistence length l_0 dominates, because l_{OSF} decreases with increasing ionic strength κ. However, the model fails for multivalent ions.

To give an example, the effective persistence length of DNA is determined to be 53 nm [111], while the intrinsic persistence length of DNA is around $l_0 = 45$ nm [112].

For completeness, other statistical parameters which are derived from the WLC model are mean-square end-to-end distance $\langle R \rangle$, mean directional cosine of the molecule $\langle \cos \tau \rangle$ and contour length l_C (depicted in Fig. 2.19).

2.7 Polyelectrolytes in Aqueous Solutions

The charge density along the PE leads to interesting properties in solutions that are discussed below.

In solution PEs, or in general ions, cannot be treated as isolated charges. Although the overall charge of the PE solution should be electrically neutral, in the vicinity of the charged PE, oppositely charged ions, the so-called counterions are present. The electrostatic interaction of macroions in aqueous monovalent salt solutions can be described by the classical mean-field treatment of electrostatic interaction, the Poisson-Boltzmann (PB) equation, that is discussed in the following.

2.7.1 Poisson-Boltzmann (PB) Equation

The Poisson-Boltzmann (PB) equation can be derived from the Poisson equation, where the electrostatic potential $\varphi(\vec{r})$ is connected with the charge density $\rho(\vec{r})$ as:

$$\nabla^2 \varphi(\vec{r}) = -\frac{1}{\varepsilon} \rho(\vec{r}). \tag{2.15}$$

Here, ε is the dielectric constant of the solution (e.g. water). At any point within the potential $\varphi(\vec{r})$ the electrostatic energy of an ion is determined by $eZ\varphi(\vec{r})$. The probability to find an ion within this potential is proportional to the Boltzmannfactor $\exp(-Ze\varphi(\vec{r})/k_B T)$. Therefore the charge density $\rho(\vec{r})$ in Eq. (2.15) can be written as:

$$\begin{aligned} \rho(\vec{r}) &= \rho_m(\vec{r}) + eZc_0 e^{-eZ\varphi(\vec{r})/k_B T} - eZc_0 e^{eZ\varphi(\vec{r})/k_B T} \\ &= \rho_m(\vec{r}) - 2eZc_0 \sinh(\frac{eZ\varphi(\vec{r})}{k_B T}), \end{aligned} \tag{2.16}$$

where ρ_m is the immobilized charge density of the macroion, Ze is the charge of the ions and c_0 the salt concentration for vanishing potential. Eqs. (2.15) and (2.16) lead directly to the classical non-linear Poisson-Boltzmann equation:

$$\nabla^2\varphi(\vec{r}) = \frac{2eZc_0}{\varepsilon}\sinh(\frac{eZ\varphi(\vec{r})}{k_BT}) - \frac{1}{\varepsilon}\rho_m(\vec{r}). \tag{2.17}$$

The mean field approximation assumes pointlike ions in thermodynamic equilibrium and ignores contributions from fluctuations as well as ion correlation effects [82]. The PB equation (2.17) can only be solved exactly in the case of a charged planar surface [82]. For other geometries this equation can be solved directly within the Debye-Hückel approximation.

2.7.2 Debye-Hückel (DH) Approximation

In the Debye-Hückel (DH) regime the electrostatic interaction energy is much smaller than the thermal energy. Thus, for these low potentials, $eZ\varphi(\vec{r}) < k_BT$, the charge density $\rho(\vec{r})$ in Eq. (2.16) can be Taylor expanded

$$\begin{aligned}\rho(\vec{r}) &= \sum_i c_{0i}Z_ie\exp(-Z_ie\varphi(\vec{r}))/k_BT + \rho_m(\vec{r}) \\ &= \underbrace{\sum_i c_{0i}Z_ie}_{=0,n_+=n_-} - \sum_i c_{0i}Z_i^2e^2\frac{\varphi(\vec{r})}{k_BT} + \rho_m(\vec{r})\end{aligned}$$

such that the Poisson-Boltzmann Eq. (2.17) can be linearized and reduces to the Debye-Hückel equation:

$$\begin{aligned}\nabla^2\varphi(\vec{r}) &= \frac{e^2}{\varepsilon k_BT}\sum_i c_{0i}Z_i^2\varphi(\vec{r}) - \frac{1}{\varepsilon}\rho_m(\vec{r}) \\ &= \kappa^2\varphi(\vec{r}) - \frac{1}{\varepsilon}\rho_m(\vec{r}) \qquad (2.18)\end{aligned}$$

where the Debye screening length κ^{-1} appears as the characteristic decay length of the potential. It is defined by

$$\kappa^2 = \frac{e^2I}{\varepsilon k_BT} = 4\pi l_BI$$

Here, $I = \sum_i c_{0i}Z_i^2 = 2Z^2c_0$ is the ionic strength and $l_B = e^2/(4\pi\varepsilon k_BT)$ is the Bjerrum length. The Bjerrum length is defined as the distance at which the electrostatic interaction between elementary charges e equals the thermal energy k_BT. In water $l_B = 0.8$ nm. In table 2.1 the screening length κ^{-1} is

Table 2.1: Screening length κ^{-1} for different NaCl solutions.

[NaCl] (mM)	κ **(nm^{-1})**	κ^{-1} **(nm)**
5	0.23	4.34
50	0.73	1.37
100	1.03	0.97
600	2.52	0.40
1000	3.25	0.31
2000	4.59	0.22

given for different salt concentrations. Under physiological conditions, i.e. at about 100 mM, the Debye screening length amounts to $\kappa^{-1} \approx 1$ nm.

If the electrostatic potential becomes larger than $k_B T$, in principle one has to solve the full non-linear PB equation (2.17). On the other hand, it has been shown that there is a wide range of salt concentrations where the DH approximation is valid [113]. It is therefore applied to the systems discussed in this thesis.

However, the solution of the DH Eq. (2.18) for an immobilized pointlike charge ($\rho_m(\vec{r}) = e\delta(\vec{r})$) is given by

$$\psi_{DH}(\vec{r}) = \frac{e\varphi(\vec{r})}{k_B T} = \frac{l_B e^{-\kappa|\vec{r}|}}{|\vec{r}|} \tag{2.19}$$

where $|\vec{r}|$ is the distance between two charges. Thus the electrostatic potential depends on the distance of the charges and the Debye screening length κ^{-1}. Hence, for vanishing salt concentrations, $\kappa \longrightarrow 0$, the DH-potential becomes the Coulomb potential again, which is the solution of the Poisson-Eq. (2.15). On the other hand, for higher salt concentration (increasing κ) the electrostatic interaction becomes more and more screened and therefore weaker. For distances $|\vec{r}| > \kappa^{-1}$ the electrostatic interaction even becomes negligible (Table 2.1).

In general, the interaction of any charge distribution $\rho_{general}(\vec{r})$ in the DH-theory can be calculated by superposition [114]:

$$\psi_{DHgeneral}(\vec{r}) = \int d\vec{r'} \psi(|\vec{r} - \vec{r'}|)\rho_{general}(\vec{r'}) \tag{2.20}$$

Using Eq. (2.20) the potential of a charged surface carrying the surface charge density $\rho_{general}(r) = \sigma e \delta(z)$ can be calculated to be

$$\psi_{DHsurf}(z) = 2\pi l_B \sigma \kappa^{-1} e^{-\kappa z}. \tag{2.21}$$

The potential of a line charge density τ at a distance r, where the charge distribution is given by $\rho_{general}(\vec{r}) = \tau e \delta(x)\delta(y)$, is

$$\begin{aligned} \psi_{DHlin}(r) &= -2l_B \tau K_0[\kappa\sqrt{x^2+y^2}] = -2l_B\tau K_0[\kappa r] \\ &= 2l_B \tau \ln(\kappa r), \end{aligned} \tag{2.22}$$

where the Bessel function $K_0[x]$ becomes $-\ln x$ for $x < 1$ as discussed below.

Bessel function. The solutions of the following differential equation

$$x^2 \frac{d^2u}{dx^2} + x\frac{du}{dx} - (x^2 + \nu^2)u = 0 \tag{2.23}$$

are the Bessel functions $K_\nu[x]$ and $I_{\pm\nu}(x)$ [115]. Eq. (2.23) is very similar to the DH-equation (as it can be seen from Eq. 2.43) and the solutions are given by the Bessel functions $K_0[x]$ and $K_1[x]$ of first and second order, respectively. For small arguments ($x < 1$) the Bessel functions become

$$\begin{aligned} K_0[x] &= -\ln(x) \\ K_1[x] &= \frac{1}{x}. \end{aligned} \tag{2.24}$$

2.7.3 Manning Condensation

In the presence of a solution of mobile monovalent salt ions, the situation of a macroion containing a charge Ze can be described as follows: Let the number of ions that lie at a certain distance from the macroion be Z'. In this region the DH approximation is still valid. However, the remaining ions $(Z - Z')$ are condensed on the macroion having a local concentration that is higher than in the surrounding salt concentration. Thus, the effective charge of the macroion becomes screened to $Z'e$ [116].

In the case of a cylindrical geometry with a charge per unit length of $\tau_C = e/f$, where f is the spacing per elementary charge, also a certain amount of ions condense on the charged cylinder. Thus, the effective charge per unit length becomes

$$\tau_C' \equiv e/l_B \tag{2.25}$$

in the region $|\tau_C| > |\tau'_C|$ [117]. This region corresponds to the region in which the dimensionless charge density (also known as the *Manning Parameter* ξ) becomes larger than 1. The Manning Parameter is defined as

$$\xi \equiv \frac{l_B|\tau_C|}{e} = \frac{l_B}{f}. \tag{2.26}$$

It defines the ratio of the electrostatic energy $eZ\varphi$ to the thermal energy k_BT. Thus, the counterion condensation threshold is given by $\xi \approx 1$. In the region $\xi > 1$, the electrostatic energy dominates over the thermal energy and the DH approximation fails (see section 2.7.2).

However, far from the cylinder surface, the potential decreases and the electrostatic energy is small compared to the thermal energy. Thus, the DH equation (2.18) becomes valid again, but the macroion charge is screened by the counterions. Using the effective charge τ'_C instead of τ_C, the electrostatic interaction at large separations can be calculated within the DH approximation.

If two oppositely charged macroions are brought into close contact with each other, their condensed counterions can be released into the solution. The released counterions will gain entropy that will favor the formation of the complex. This release is referred to as the entropic counterion effect.

2.8 Adsorption of Polyelectrolytes

The solution of the DH Eq. (2.18) depends strongly on the geometrical models like planar surfaces, spheres or cylinders. These simplified models stand for realistic situations like membranes, proteins or stiff PEs, respectively. The following section concentrates on the adsorption of PE on two model systems: planar surface and cylinder.

2.8.1 Charged Planar Surface

There is a wide range of experimental studies of polyelectrolyte adsorption onto charged planar surfaces like charged membranes [118], or in multilayer adsorption [69]. For all these cases the driving force is the electrostatic interaction. Therefore, the adsorption process can be modulated by parameters like the charge densities of polymers or substrates [119]. Another way to modify the interaction is to change the ionic strength of the solvent [120]. Furthermore, Rojas et al. [121] report on the desorption of PEs by increasing the salt concentration of the solution.

Theoretically, the electrostatic interactions in these adsorption processes have been described on the Debye-Hückel level [122]. Here, the adsorption process of a semiflexible PE on an oppositely charged planar surface is discussed on the basis of the balance between electrostatic attraction between substrate and polymer, electrostatic repulsion between nearest polymer neighbors, and the entropic repulsion due to the confinement of the polymer strands [123]. The electrostatic energies change upon varying the line charge density of the PE, τ_P, the surface charge density of the substrate, σ, and the salt concentration of the solution ($c_0 \sim \kappa$). However, the driving force for adsorption is the potential $\psi_{DHsurf}(z)$ created by the constant surface charge density $\rho_{general}(r) = \rho_{surf}(z) = \sigma e \delta(z)$ that is derived in Eq. (2.21).

Electrostatic adsorption. The electrostatic adsorption energy density f_{attr} of a cylinder with line charge τ_P and radius r, within the surface potential given by Eq. (2.21) is according to [122], always in units of k_BT

$$f_{attr} = -2\pi l_B \sigma \tau_P e^{-\kappa\delta} \kappa^{-1} b^{-1} I_0[\kappa r], \tag{2.27}$$

where δ is the vertical polymer-surface distance. In the adsorbed case $\delta = r$. b is the PE-PE distance and $I_0[z]$ the Bessel function.

In the limit of low and high salt concentrations in the solution, Eq. (2.27) becomes

$$f_{attr} \simeq \begin{cases} -2\pi l_B \sigma \tau_P b^{-1} \kappa^{-1} & \text{for} \quad r \ll \kappa^{-1} \\ -\sqrt{4\pi} l_B \sigma \tau_P \kappa^{-3/2} r^{-1/2} b^{-1} & \text{for} \quad r \gg \kappa^{-1} \end{cases} \tag{2.28}$$

Noteworthy, in the experiments described in this thesis, the radius of the PE r is always smaller than the Debye screening length κ^{-1}. Thus, in the following only $r \ll \kappa^{-1}$ will be considered.

Electrostatic repulsion. The repulsive electrostatic free energy density between neighboring PE each with the line charge density τ_P and a line potential given by Eq. (2.22) can be calculated to be

$$f_{rep} = \frac{2 l_B \tau_P^2}{b} \sum_{j=1}^{\infty} K_0[j\kappa b], \tag{2.29}$$

In the limit $b \ll \kappa^{-1}$, i.e. the neighboring distance is much smaller than the screening length, the sum becomes an integral. On the other hand, for high salt concentrations, $b \gg \kappa^{-1}$, i.e. the distance between PEs becomes much larger than the screening length, the first term in the sum of Eq. (2.29) dominates. Thus, Eq. (2.29) becomes in the limits

$$f_{rep} \simeq \begin{cases} 2l_B\tau_P^2 b^{-1}\int_{s=0}^{\infty} K_0[s\kappa b]ds = \pi l_B \tau_P^2 b^{-2}\kappa^{-1} & \text{for} \quad b \ll \kappa^{-1} \\ \sqrt{2\pi} l_B \tau_P^2 e^{-\kappa b} b^{-3/2}\kappa^{-1/2} & \text{for} \quad b \gg \kappa^{-1} \end{cases} \tag{2.30}$$

using the Bessel function introduced in Eq. (2.24).

Considering Eq. (2.30) it can be seen, that if the PEs are further apart than the screening length ($b \gg \kappa^{-1} \Leftrightarrow b\kappa \gg 1$), the repulsive electrostatic free energy density will be screened.

Entropic repulsion. Additional to the electrostatic repulsion, in the adsorbed state, the polymers feel an entropic repulsion due to their confinement. The entropic free energy density due to the steric interaction between the PEs is shown by Odijk [124] to be:

$$f_{ent} \sim b^{-5/3} l_{eff}^{-1/3} \ln(l_{eff}/b). \tag{2.31}$$

Here, l_{eff} denotes the effective persistence length of the PE.

Total free energy. Finally, the total free energy density is given by the sum of Eqs. (2.28), (2.30), and (2.31)

$$f_{tot} \simeq f_{attr} + f_{rep} + f_{ent}. \tag{2.32}$$

Comparing the different energy contributions (Eqs. 2.28, 2.30, 2.31), they depend differently on the PE-PE distance b as well as on the salt concentration κ. Therefore, different regimes are discussed in detail. For the following a characteristic length b^* is introduced.

$\boldsymbol{\kappa^{-1}} < b^* < b$. Starting with the regime in which the characteristic length b^* is smaller than b, the repulsive contributions are dominated by the entropic part and the effective free energy density f_{tot} in Eq. (2.32) can be written as the sum of Eq. (2.28) and Eq. (2.31)

$$f_{tot,h} \simeq -\frac{l_B \sigma \tau_P}{b\kappa} + l_{eff}^{-1/3} b^{-5/3} \ln(l_{eff} b^{-1}). \tag{2.33}$$

In this regime, the balance between the electrostatic attraction and the entropic repulsion determines the mean PE-PE distance b_{ent} [122]

$$\begin{aligned} f_{attr} + f_{ent} &= 0 \\ \Rightarrow b_{ent} &\sim \left(\frac{\kappa}{\tau_P \sigma l_B l_{eff}^{1/3}} \ln\left(\frac{\tau_P \sigma l_B l_{eff}}{\kappa}\right)\right)^{3/2}. \end{aligned} \tag{2.34}$$

For increasing salt concentration (i.e. increasing κ), the mean PE-PE distance b_{ent} will also increase ($b_{ent} \sim \kappa^{3/2}$). This result has been found experimentally by Fang and Yang [120].

$\boldsymbol{\kappa^{-1}} < b < b^*$. For this situation the repulsive energy contribution is dominated by the electrostatic energy (Eq. 2.30). Neglecting the steric contribution (Eq. 2.31), the effective free energy density f_{tot} in Eq. (2.32) becomes:

$$f_{tot,l} \simeq -\frac{l_B \sigma \tau_P}{b\kappa} + \frac{l_B \tau_P^2}{e^{\kappa b} b^{3/2} \kappa^{1/2}}. \tag{2.35}$$

In this regime, the mean PE-PE distance b_e is determined by the balance between the electrostatic attraction and repulsion [122]:

$$\begin{aligned} f_{attr} + f_{rep} &= 0 \\ \Rightarrow b_e &\sim \kappa^{-1} \ln(\kappa \tau_P \sigma^{-1}). \end{aligned} \tag{2.36}$$

In contrast to b_{ent} in Eq. (2.34), the electrostatically stabilized PE-PE distance b_e will decrease for increasing salt concentration ($b_e \sim \kappa^{-1}$).

In summary, if the intermolecular spacing b is larger than the characteristic length b^*, the PE interstrand distances will be stabilized through the Odijk repulsion (Eq. 2.34). In this case the PE-PE distance will increase for increasing salt concentration. On the other hand, if the distance between neighboring PEs is smaller than b^*, the PE interstrand distances will be electrostatically stabilized (Eq. 2.36). Here, the intermolecular spacing will decrease for increasing salt concentration. Overall, the increase of salt concentration does not lead to a linear increase of the PE-PE distance b but rather contains a minimum as depicted in Fig. 2.20. This minimum can be explained by the fact, that for increasing salt concentration the electrostatic repulsion becomes screened while the entropic repulsion stays the same.

Furthermore, the desorption threshold in the adsorption process can be calculated. Here, the layer thickness δ is defined as the PE-PE distance in the vertical direction, i.e. the calculations of the horizontal PE-PE distance in Eq. (2.27) to Eq. (2.34) can now be considered for the vertical case. Thus, the PE-PE distance b is replaced by the PE-surface distance δ, i.e. the thickness of the PE layer on the surface. In the case of $\delta < \kappa^{-1} < l_{eff}$, minimizing the total free energy of the system Eq. (2.33) with respect to the layer thickness $\partial(f_{attr} + f_{ent})/\partial\delta = 0$, the maximal layer thickness can be estimated [122]

$$\delta \sim \left(\frac{\ln(l_B \sigma \tau_P l_{eff}^2)}{l_B \sigma \tau_P l_{eff}^{1/3}} \right)^{3/5} \tag{2.37}$$

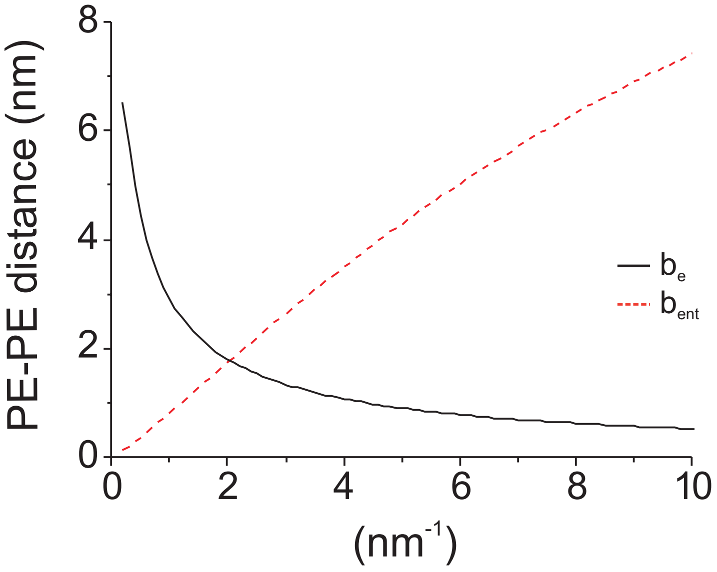

Figure 2.20: PE-PE distance versus salt concentration. Comparison between the PE-PE distance stabilized by entropic repulsion b_{ent}(dotted line, Eq. 2.34) and by electrostatic repulsion b_e (line, Eq. 2.36) for variable salt concentration ($\sim \kappa$). For the calculation $\tau_P \simeq 5.88e/\mathrm{nm}$, $\sigma \simeq 0.32e/\ \mathrm{nm}^2$, $l_B \simeq 0.7$ nm, $l_{eff} \simeq 45$ nm were chosen, and κ is taken from Table 2.1.

Using Eq. (2.37) the onset of desorption of the PEs can be estimated. Assuming a layer thickness δ of the order of the Debye screening length κ^{-1}, i.e. $\delta = \kappa^{-1}$ in Eq. (2.37), either the threshold of the surface charge or of the salt concentration c_0 ($c_0 \sim \kappa$) for the desorption process can be calculated:

$$\begin{aligned} \sigma &\sim \frac{\kappa^{5/3}}{\tau_P l_B l_{eff}^{1/3}} \\ \Leftrightarrow \kappa &\sim (\sigma \tau_P l_B)^{3/5} l_{eff}^{1/5}. \end{aligned} \tag{2.38}$$

2.8.2 Charged Cylinders

In the case of the adsorption of a semiflexible polyelectrolyte onto a charged cylinder, two approaches are discussed, which will be compared with the experimental results in section 4.4: First, the linear approach, in which all interactions between the charges are given by the DH-potential (Eq. 2.18) [73]. Second, the non-linear approach [72], in which the entropic counterion effect is directly taken into account. Both theories describe a helical conformation

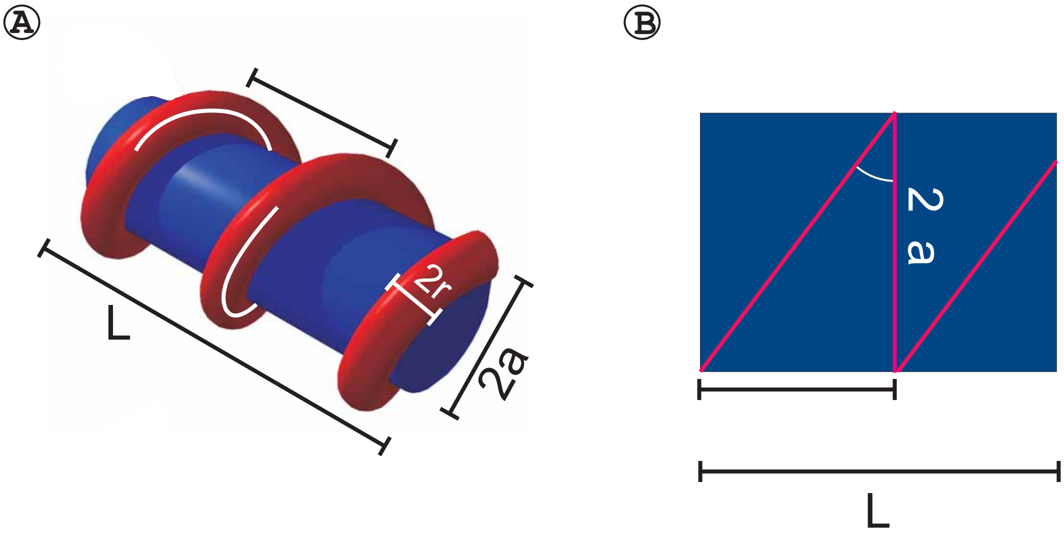

Figure 2.21: Wrapping model. The cylinder is characterized by its length L and radius a. The length of the wrapped PE is $l = n\eta\sigma$, where η is the wrapping parameter and σ the projected length on the cylinder. A) Helical conformation of the wrapped PE (red) around the cylinder (blue). B) Geometry of the wrapping parameters. PE counter length (red) on the flat cylinder area (blue).

in which the PE is wrapped around the cylinder as it is depicted in Fig. 2.21a. The first approach also considers the case of parallel alignment of the adsorbed PE onto the cylinder. In addition, an overcharging of the complex is predicted within both theories. While in the linear case this overcharging is due to electrostatic effect, for the non-linear approach, the overcharging can be explained by the balance of entropic effects (counterion release) and bending energy.

Nevertheless, in both theories, the total free energy of a complex of a semiflexible polymer and a rigid oppositely charged cylinder can be split into independent parts. First the attractive contribution between the oppositely charged semiflexible chain and the rigid cylinder, second the repulsive part, to which the electrostatic repulsion of the polymer chain as well as thirdly, the mechanical bending energy contributes. In the following, the different parts are derived separately with respect to the linear and non-linear case and finally added to obtain the total free energy of the system. First of all the line charge density of a cylinder is calculated:

Line charge density of a cylinder. The electric field E at the surface of a charged cylinder (number of charges N, radius a, length L, elementary charge e) can be calculated using Gauss‘s law:

$$\begin{aligned} \oint E dA &= \frac{Q}{\varepsilon} \\ \Leftrightarrow 2\pi a L E &= \frac{Ne}{\varepsilon} \\ \Leftrightarrow E &= \frac{\kappa N e}{2\pi\varepsilon x L}, \end{aligned} \tag{2.39}$$

with the dimensionless radius $x = \kappa a$.

Using the relations

$$E = -\tfrac{\kappa}{e} k_B T \tfrac{dy}{dx} \quad \text{and} \quad y = \tfrac{e}{k_B T}\Psi, \tag{2.40}$$

between the electric field E and the dimensionless electrostatic potential y, Eq. (2.39) can be rewritten as

$$\begin{aligned} E &= \frac{\kappa N e}{2\pi\varepsilon x L} = -\frac{\kappa k_B T}{e}\frac{dy}{dx} \\ \Leftrightarrow & \quad -\frac{x}{2}\frac{dy}{dx} = \frac{e^2 N}{4\pi\varepsilon k_B T L}. \end{aligned} \tag{2.41}$$

The right hand side is defined as the dimensionless linear charge density of the cylinder ξ (see also Eq. 2.26), assuming a linear distribution of charges, i.e the spacing per elementary charge $f = L/N$:

$$\xi = \frac{e^2 N}{4\pi\varepsilon k_B T L} = \frac{l_B}{f} = \frac{l_B \tau_C}{e}, \tag{2.42}$$

and the linear charge density of the cylinder is given by $\tau_C = e/f$.

Attractive electrostatic energy. The electrostatic interaction energy between the cylinder and the PE can be solved by the DH equation (2.18): Using cylinder coordinates, the dimensionless radius x, and the dimensionless electrostatic potential y as defined in Eq. (2.40), the DH equation becomes

$$\begin{aligned} \triangle\psi &= \frac{1}{r}\frac{d}{dr}\left[r\frac{d\psi}{dr}\right] = \kappa^2\psi \\ \Leftrightarrow & \quad \frac{1}{r}\frac{d\psi}{dr} + \frac{d^2\psi}{dr^2} - \kappa^2\psi = 0 \\ \Leftrightarrow & \quad \frac{d^2 y}{dx^2} + \frac{1}{x}\frac{dy}{dx} - y = 0 \end{aligned} \tag{2.43}$$

The solution of this differential equation is given by $y = CK_0[x]$, using the Bessel functions introduced in Eq. (2.24). Applying the Bessel function relation

$$\begin{aligned} \frac{dy}{dx} &= C\frac{dK_0[x]}{dx} = -CK_1[x] \\ \Leftrightarrow \quad & C = -\frac{1}{K_1[x]}\frac{dy}{dx} \end{aligned} \tag{2.44}$$

and $\frac{dy}{dx}$ from Eq. (2.41), the solution of Eq. (2.43) becomes

$$\begin{aligned} y &= -\frac{K_0[x]}{K_1[x]}\frac{dy}{dx} \\ &= \frac{K_0[x]}{K_1[x]}\frac{2l_B\tau_C}{x} \\ &= \frac{2l_B\tau_C}{\kappa a}\frac{K_0[\kappa a]}{K_1[\kappa a]}. \end{aligned} \tag{2.45}$$

The PE has a total length of $l = n\eta\sigma$, where η is the wrapping parameter, σ is the projection length on the cylinder, and τ_P is the linear charge density as depicted in Fig. 2.21. The wrapping parameter η is defined as the ratio between the contour length of the PE, $l = n\eta\sigma$, and the projection length on the cylinder, $L = n\sigma$. In Fig. 2.21b it is shown that the wrapping parameter can also be derived as $\eta = \sqrt{1 + (2\pi a/\sigma)^2}$. On the other hand, the oppositely charged cylinder has a total length of L and a linear charge density of τ_C (see Fig. 2.21a). Thus, the electrostatic attraction energy between the PE and the cylinder within the potential given by Eq. (2.45) is given by [73]

$$\frac{F_{attr}}{k_BT} = -\frac{\eta 2l_B\tau_C\tau_P K_0(\kappa a)}{\kappa a K_1(\kappa a)}, \tag{2.46}$$

In the limit of low salt concentration $\kappa a \to 0$, the Bessel functions in Eq. (2.24) can be applied and thus, Eq. (2.46) can be simplified in this limit to

$$\frac{F_{attr}}{k_BT} \cong -\eta 2l_B\tau_C\tau_P \ln(\kappa a). \tag{2.47}$$

Note that the attractive electrostatic energy part is independent of the geometry of the system.

Repulsive electrostatic energy. For the repulsive energy contribution two parts have to be considered: First, the repulsive electrostatic energy and second, the mechanical bending energy.

Starting with the electrostatics one has to define the geometry of the system as it is already done in Fig. 2.21a. The electrostatic energy is calculated by the integration of the DH-interaction (Eq. 2.20) using the charge density distribution of the helical conformation of the PE $\tau_P l$. For $\kappa \to 0$ the electrostatic repulsive energy contribution is shown by Kunze and Netz [73] to become

$$\begin{aligned}\frac{F_{rep}}{k_B T} &= l_B \tau_P^2 \eta(\eta-1) K_0[\kappa a] \\ &\cong l_B \tau_P^2 \eta(\eta-1)\ln(\kappa a).\end{aligned} \tag{2.48}$$

Here, the electrostatic repulsion of the PE was deduced by subtracting the self energy of a straight PE (same contour length) from the self energy of a PE in the helical conformation [73].

Mechanical bending energy. The second term which contributes to the repulsion energy of the total free energy of the system is the mechanical bending energy term. This energy originates from the mechanical bending rigidity of the semiflexible chain wrapped around the rigid cylinder. With the curvature radius of the polymer $\rho = \cos^2\alpha/a$ and the persistence length of the chain l_{eff} the bending energy reads

$$\begin{aligned}\frac{F_{bend}}{k_B T} &= \frac{l_{eff}}{2}\int_0^{\frac{L}{\sin\alpha}} \rho^2 ds \\ &= \frac{l_{eff}\rho^2 L}{2\sin\alpha} \\ &= \frac{l_{eff}L}{2a^2}\frac{\cos^4\alpha}{\sin\alpha} \\ &= \frac{l_{eff}L}{2a^2}\left(\frac{1}{\sin\alpha} - 2\sin\alpha + \sin^3\alpha\right)\end{aligned} \tag{2.49}$$

$$\begin{aligned}&= \frac{l_{eff}L}{2a^2}\left(\frac{\eta\sigma}{\sigma} - 2\frac{\sigma}{\eta\sigma} + \left(\frac{1}{\eta}\right)^3\right) \\ &= \frac{l_{eff}L}{2a^2}\frac{(\eta^2-1)^2}{\eta^3},\end{aligned} \tag{2.50}$$

where the length of the wound chain within one pitch is $\eta\sigma$ (see Fig. 2.21).

Free energy, linear approach. The complete free energy $F_{tot,lin}$ of the semiflexible PE wrapped around the stiff cylinder in the linear approach is the sum of electrostatic attraction (Eq. 2.47), electrostatic repulsion (Eq. 2.48), and bending energy (Eq. 2.50)

$$\begin{aligned}\frac{F_{tot,lin}}{k_BT} &= \frac{F_{attr}}{k_BT}+\frac{F_{rep}}{k_BT}+\frac{F_{bend}}{k_BT} \\ &= 2\eta l_B\tau_C\tau_P\ln(\kappa a)-\eta(\eta-1)l_B\tau_P^2\ln(\kappa a)-\frac{l_0L}{2a^2}\frac{(\eta^2-1)^2}{\eta^3}\end{aligned} \quad (2.51)$$

For vanishing salt concentration ($\kappa a \to 0$), an analytical solution can be given [73]. In this limit, also the bending energy (Eq. 2.50) becomes negligible, compared to the diverging electrostatic contributions. Therefore, minimizing the total free energy (Eq. 2.51) with respect to the wrapping parameter η (i.e. $\partial F_{tot,lin}/\partial\eta = 0$) leads to

$$\eta = \frac{\tau_C}{\tau_P}+\frac{1}{2} \quad (2.52)$$

The effective charge of the complex is given by

$$\begin{aligned}\tau_{eff} &= \tau_C-\eta\tau_P \\ &= -\frac{\tau_P}{2},\end{aligned} \quad (2.53)$$

using Eq. (2.52), such that an overcharging of the complex is favored and the wrapped PE dominates the effective charge of the complex. The effect of overcharging is solely caused by energetic contributions (compare with Eq. 2.51).

However, for finite κa the minimal energies are solved numerically [73]. The overcharging of the complex is shown in Fig. 2.22. Here, the wrapping parameter η as a function of κa is plotted. For increasing salt concentration (i.e. increasing κa) the wrapping parameter η also increases. Thus, the amount of the wrapped length of PE must increase for the same projection length σ on the cylinder for increasing salt concentration.

Although, Kunze and Netz [73] report besides the helical also on a parallel adsorption of the semiflexible PE on the cylinder, this parallel configuration was not observed in the experiments. It might be that the helical conformation is kinetically favored. A detailed description on the energy contributions for this parallel morphology can be found elsewhere [73].

However, for a better comparison of the linear to the non-linear case, the self energy of the bare cylinder $F_C/(k_BT) = -l_B\tau_C^2\ln(\kappa a)$ is added to the total free energy of the linear system. Thus, Eq. (2.51) can be rewritten in the linear

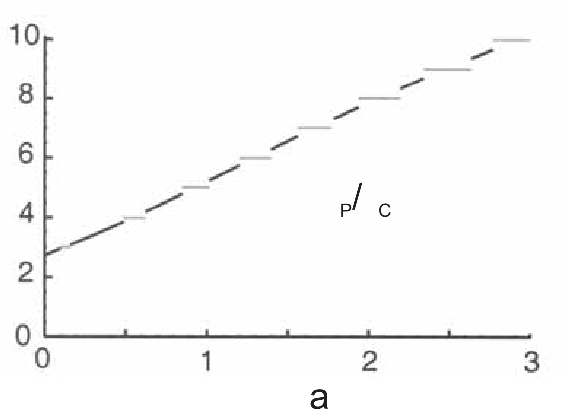

Figure 2.22: Wrapping parameter η as a function of the dimensionless radius of the cylinder κa [73]. Here, the helical conformation is indicated by the black lines, whereas the parallel conformation by the grey line. The charge ratio is fixed to $\tau_P/\tau_C = 0.5$, that is similar to the charge ratios in this thesis. For increasing salt concentration (increasing κ) the wrapping parameter also increases [73].

case as

$$\begin{aligned}
\frac{F_{tot}}{k_B T} &= \frac{F_{attr}}{k_B T} + \frac{F_{rep}}{k_B T} + \frac{F_C}{k_B T} \\
&\simeq 2\eta l_B \tau_C \tau_P \ln(\kappa a) - \eta(\eta - 1) l_B \tau_P^2 \ln(\kappa a) - l_B \tau_C^2 \ln(\kappa a) \\
&\simeq -(\tau_C - \eta\tau_P)^2 l_B \ln(\kappa a) + l_B \tau_P^2 \eta(\ln(\kappa x) + \ln(a/x)) \\
&\simeq \tau_{eff}^2 l_B \ln(1/(\kappa a)) + l_B \tau_P^2 \eta \ln(\kappa x) + l_B \tau_P^2 \eta \ln(a/x) \qquad (2.54)
\end{aligned}$$

The first term in Eq. (2.54) describes the capacitive charging energy of the complex (sum of electrostatic attraction energy, electrostatic repulsion energy, and self energy of the bare cylinder). The second and the third term describe the electrostatic self energy of the bare PE in the linear case and the difference of the self energy between the smeared out and helical charge distribution on the cylinder surface, respectively [73].

Free energy, non-linear approach. For the non-linear case the non-linear PB equation (Eq. 2.17) has to be solved (see also section 2.7.3). In fact, if the dimensionless linear charge density of the PE, ξ_P, is above counterion condensation threshold, i.e. $\xi_P > 1$, the electrostatic self energy of the PE will change. Now entropic counterion effects are dominant and the PE energy contributions become [72]

$$\frac{F_E}{k_B T} \simeq 2\xi_{eff} \ln(\xi_P/(\kappa x)), \qquad (2.55)$$

where ξ_{eff} is the dimensionless linear charge density of the complex system.

Park et al. [72] derived this electrostatic free energy contribution of the PE by solving the non-linear PB equation using the classic Lifson-Katchalsky approach [125].

Despite the different energy contribution for the PE in the linear and non-linear case, the capacitive charging energy of the complex stays the same, given in the first term of Eq. (2.54).

Additionally, the bending energy in Eq. (2.50) can be expressed in terms of dimensionless charge densities $\xi \equiv l_B \tau e^{-1}$, by following considerations: A certain length of the PE l' is needed to wrap around the cylinder in order to gain a neutral complex, $L\xi_C = l'\xi_P$, assuming that an additional length of the PE l'' having a charge of $l''\xi_P$ is wrapped around the cylinder, resulting in a complex of charge $\xi_{eff} = l''\xi_P/L$. Using Eq. (2.49), the bending energy can be expressed as

$$\begin{aligned}\frac{F_{bend}}{k_B T} &= \frac{l_{eff} L}{2a^2}\left(\frac{l'+l''}{L} - 2\frac{L}{l'+l''} + \left(\frac{L}{l'+l''}\right)^3\right)\\ &\simeq \frac{l_{eff} L}{2a^2}\left(\frac{l'}{L} + \frac{l''}{L}\right)\\ &\simeq \frac{l_{eff} L}{2a^2}\left(\frac{\xi_C}{\xi_P} - \frac{\xi_{eff}}{\xi_P}\right). \end{aligned} \tag{2.56}$$

Thus, the total free energy of the system of the non-linear case is the sum of the capacitive charging energy of the complex (first term in Eq. 2.54), the electrostatic free energy of the PE (Eq. 2.55), and the mechanical bending energy (Eq. 2.56)

$$\frac{F_{tot,non}}{k_B T} \simeq \xi_{eff}^2 \ln(1/(\kappa a)) + 2\xi_{eff} \ln(\xi_P/(\kappa x)) + \frac{l_{eff} L}{2a^2}\left(\frac{\xi_C}{\xi_P} - \frac{\xi_{eff}}{\xi_P}\right). \tag{2.57}$$

In comparison to the total free energy of the linear case (Eq. 2.54), the first term is the same but the second term is replaced by the self energy of the PE on the non-linear case (including the entropic counterion effects) and the bending energy term is not neglected [72]. Thus, minimizing the total energy in Eq. 2.57 with respect to the effective dimensionless charge density $\partial F_{tot,non}/\partial \xi_{eff} = 0$, the effective charge density of the system becomes

$$\xi_{eff} \simeq \frac{l_{eff} L/(a^2 \xi_P) - \ln(\xi_P/(\kappa x))}{\ln(1/(\kappa a))}. \tag{2.58}$$

Note that the denominator will always be positive, because $a < \kappa^{-1}$, and the electrostatic free energy of the PE in the numerator will also always be positive, because $\kappa x < 1 < l_B \tau_P e^{-1} = \xi_P$. Overall, the numerator determines whether the effective charge density of the system ξ_{eff} becomes *undercharged* (positive) or *overcharged* (negative). Thus, for smaller bending energy contributions compared to the electrostatic free energy term, the dimensionless charge density becomes negative such that the complex is overcharged. Overall, the charge of the complex in the non-linear case (Eq. 2.58) is defined by the balance of the flexibility and the entropy due to counterion release of the wrapping PE.

On the other hand, neglecting the bending energy due to the same arguments as in the linear case [73], the total free energy in the non-linear case can be written as

$$\frac{F_{tot,r}}{k_B T} \simeq -(\tau_C - \eta \tau_P)^2 l_B \ln(\kappa a) + \frac{2\eta\tau_P}{e} \ln\left(\frac{e l_B \tau_P}{\kappa a}\right). \tag{2.59}$$

In comparison to the linear case in Eq. (2.54), the first term stayed the same, whereas the second term of the self energy of the PE in the linear limit was replaced by the self energy including the entropic counterion effects (Eq. 2.55). Minimizing Eq. (2.59) with respect to the wrapping parameter η leads to

$$\eta = \frac{\tau_C}{\tau_P} + \frac{1}{e l_B \tau_P}, \tag{2.60}$$

and the effective charge of the complex in the non-linear case, neglecting the bending energy, can be calculated using again

$$\tau_{eff} = \tau_C - \eta \tau_P. \tag{2.61}$$

In summary, comparing the results of the free energy of the linear Eq. (2.54) and the non-linear case Eq. (2.57) both theories predict overcharging of a helical morphology of the resulting complex. For both cases the first term in Eq. (2.54) and Eq. (2.57) describes the capacitive charging energy of the complex (sum of electrostatic attraction energy, electrostatic repulsion energy, and self energy of the bare cylinder). In contrast, the self energy of the PE is different. The non-linear approach of Park et al. includes the counterion entropy whereas the linear approach of Kunze and Netz deduces the contribution in the DH regime. Nevertheless, Kunze and Netz stated that the electrostatic self energy of the PE given by Eq. (2.48) is in agreement to earlier studies that used also the dimensionless PE charge density ξ_P above the counterion condensation threshold ($\xi_P > 1$), such that the free energy (Eq. 2.54) of the linear approach is also valid at elevated salt concentrations. Therefore both theories are considered for the interpretation of the experiments discussed in section 4.4.5.

Chapter 3

Materials and Methods

3.1 DNA

Circular pUC19 (2686 bp) and circular pBR325 (5994 bp) plasmid DNA were purchased from MoBiTec GmbH, Göttingen, Germany. These DNA samples could be used for SFM measurements without additional purification. For the following preparations, both DNA samples are over 80% supercoiled. Note that during storage, plasmid DNA will slowly convert from supercoiled to relaxed circles[1].

Purified linearized pUC19 plasmid DNA (2682 bp) and linearized 213 bp DNA were courtesy provided by S. Reich (Institute of Virology, Group of Dr. Reuter, Humboldt University Medical School (Charité), Berlin, Germany). The plasmid was grown in Escherichia coli TG1 and purified using the QIAprep Spin Miniprep Kit (Qiagen, Hilden, Germany). The plasmid was linearized using BamHI (New England Biolabs, Frankfurt, Germany) and then extracted from gel with the QIAquick Gel Extraction Kit (Qiagen, Hilden, Germany), phenol/chloroform extracted, ethanol precipitated and resuspended in 10 mM Tris-HCl, pH 8. The homogeneity of the lengths of the linearized pUC19 plasmid was checked by electrophoresis on a 0.8 % agarose gel. The DNA concentration was determined by light absorbance at 260 nm.

All DNA samples were stored in a buffer solution [5 mM N-[2-hydroxyethyl] piperazine-N' [2-ethanesulfonic acid] (HEPES), NaOH at pH 7.5]. DNA samples of a concentration of 10 ng/μl were stored in the fridge (4^0 C) whereas at higher concentrations in the freezer (-20^0 C).

---

[1] Supplementary information given on the product sheet (MoBiTec GmbH, Göttingen, Germany.)

3.2 Poly-L-Ornithine

Amino acids are the primary components of proteins (see section 2.1). Besides the twenty well known alpha-amino acids there are many other naturally occuring amino acids. For example the poly amino acid poly-L-ornithine (Fig. 2.2b). Due to its positively charged side chain (i.e. $-(CH_2)_3NH_3^+$) this amino acid is a highly positively charged molecule. Poly-L-ornithine was purchased from Sigma, St. Luis, USA, with a molar mass of $30\ 000-70\ 000$ g/mol and stored in the fridge.

3.3 Dendronized Polymers

The dendronized polymers used in the experiments described below were synthesized by L. Shu in the group of Prof. A. D. Schlüter at the Free University, Berlin. Starting with the trimethylsilyl(ethyloxy)carbonyl (Teoc) protected peripheral amine functionalized dendronized polystyrene of generation one (PG1Teoc), higher generations (second (PG2), third (PG3) and fourth (PG4)) were obtained by the so called mixed "attach-to" approach (Fig. 3.1, [64]). To verify the complete reaction steps during the "attach-to" route in order to synthesize PG2, PG3, and PG4, the degree of coverage of the terminal amine groups was determined. This coverage was checked using 2,4-dinitrofluorobenzene (Sanger reagent) to react with unreacted amine groups (see Fig. 3.3). According to UV measurements the amount of reacted Sanger reagents was determined quantitively and amounted to less than 99.2% and 99.4% for PG2 and PG4, respectively [56]. With this, the successful synthesis of PG2 and PG4 was proven.

The molar mass distribution of the core dendronized polymer PG1Teoc was estimated by analytical gel permeation chromatography (GPC) measurements ($M_n = 290\ 000, M_w = 510\ 000$ and $PD = 1.77$) using polystyrene for calibration. For PG2, PG3 and PG4 each repeat unit has a molar mass of 1 285 g/mol, 2 539 g/mol and 5 089 g/mol, respectively. Besides the molar mass and steric congestion also the number of surface charges per repeat unit increases for increasing dendron generations up to 4 for PG2, 8 for PG3 and 16 for PG4 (Fig. 3.1). The latter leads to 1.9×10^{12} positive charges for 1 ng of dendronized polymers. By increasing dendron generation, the branched structures also increase, which leads to higher densely filled volumes. This effect will be referred to in the following as bulkiness. This effect can be demonstrated using the DISCOVER Molecular Simulation Program, Materials Studio^{TM} [65] to minimize the structure of 80 repeat units of the dendronized polymer of generation 2,3, and 4 (Fig. 3.2). The minimization was done in vaccuum

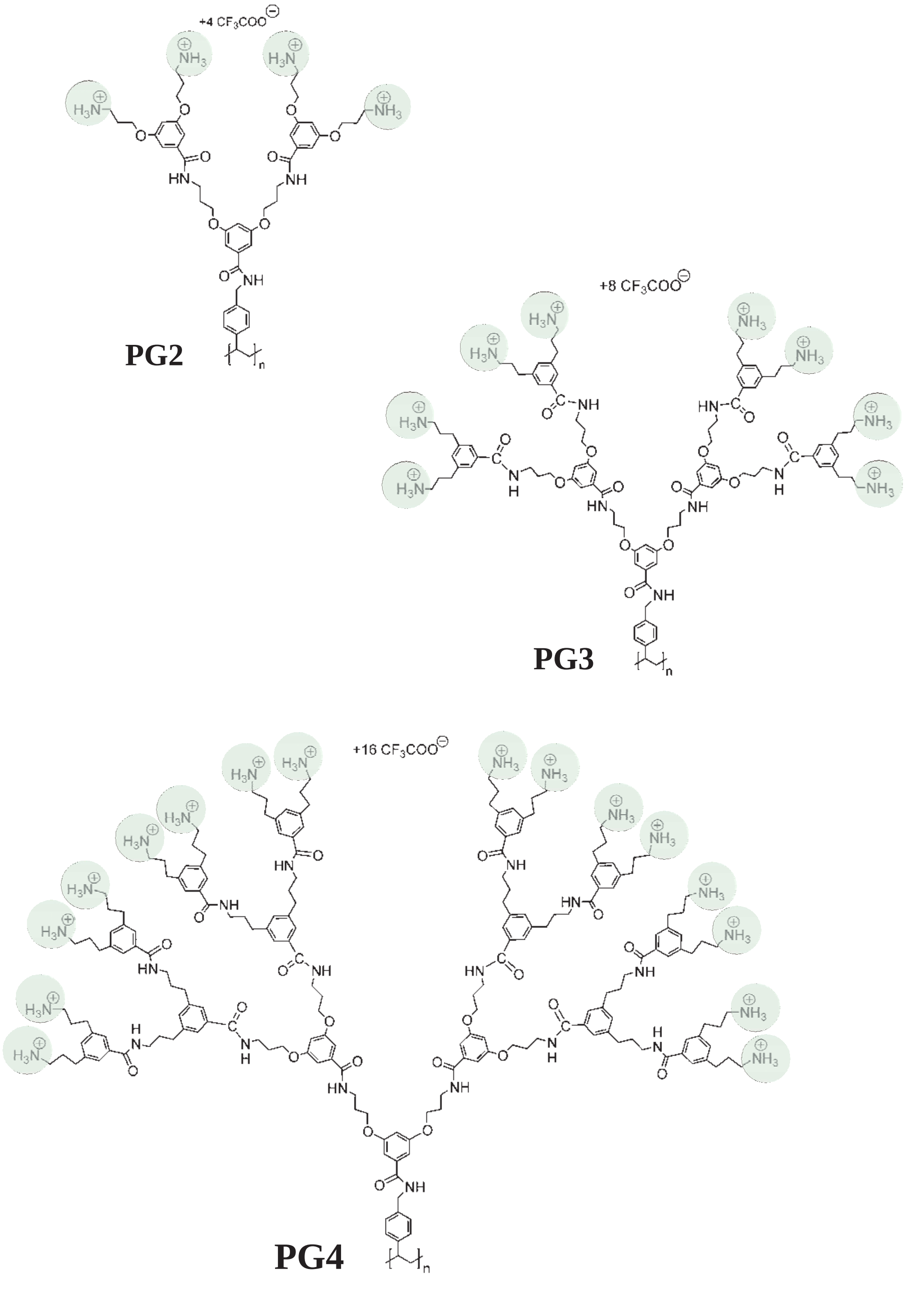

Figure 3.1: Chemical structure of the repeat unit of dendronized polymers of generation 2 (PG2), 3 (PG3), and 4 (PG4).

using the Polymer Consistent Force Field (PCFF) and the total number of iteration was 5000 for 5322, 10922, and 22122 atoms for generation 2, 3, and 4, respectively.

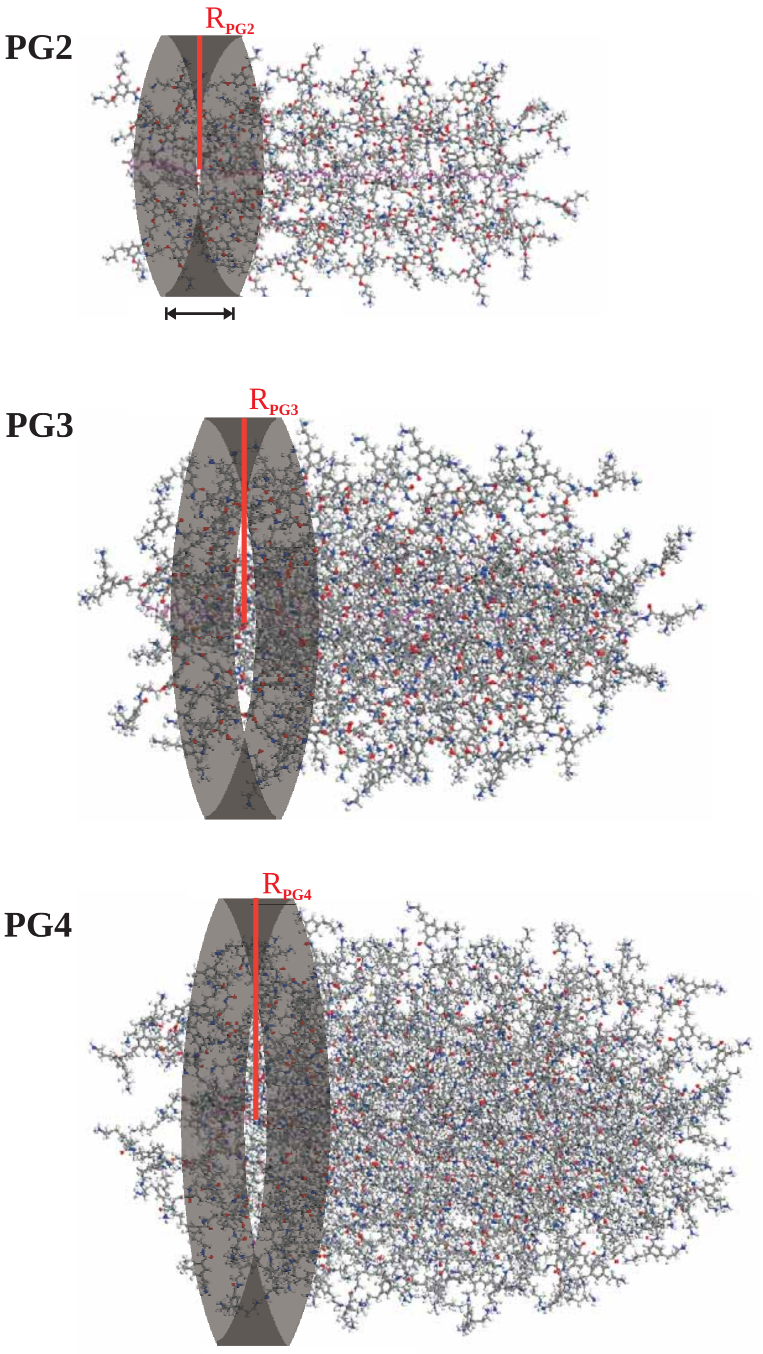

Figure 3.2: Dendronized polymers of generation 2, 3, and 4. PG2, PG3, and PG4 after a molecular minimization simulation (PCFF) of 80 repeat units show the increasing bulkiness for increasing generation. Colour code: (H:white), (C:grey), (N:blue), (O:red), (backbone:purple). A part of the dendronized polymers is covered by a grey cylinder with length Δ and radius R.

Based on the volume of the dendronized polymers and assuming an approximated density of a condensed dendronized polymer of $\rho_p = 1\text{g/cm}^3$ and using

$$\begin{aligned} V = \frac{M}{N_A \rho_g} &= \pi r^2 l \\ \Leftrightarrow r &= \sqrt{\frac{M}{N_A \rho_p \pi l}}, \end{aligned} \tag{3.1}$$

where N_A is the Advogadro′s constant, M the molar mass, and $l = 0.25$ nm the contour length of the repeat unit in the all-trans conformation, the radii can be estimated to (1.6 ± 0.2) nm, (2.3 ± 0.2) nm and (3.3 ± 0.3) nm for PG2, PG3 and PG4, respectively. These diameters are a lower limit, neglecting the artificial structure and swelling of the dendronized polmyers as discussed in section 4.5.3.

Assuming the contour length of the repeat unit $l = 0.25$ nm in the all-trans conformation, the surface charge of 10 repeat units of the cylinder surface ($\Delta = 10l = 2.5$ nm, indicated by the grey surface in Fig. 3.2) can be calculated to 0.62e/nm^2, 0.44e/nm^2, and 0.32e/nm^2 for PG4, PG3, and PG2, respectively. The surface charge density is highest for PG4 and reduces with descending generation.

Using the equilibrium reaction with respect to the terminal amine groups (pK_a=10.6) [10], the amine groups should be all charged at pH 7-8:

$$\begin{aligned} RNH_3^+ &\rightleftharpoons RNH_2 + H^+ \\ K_a &= \frac{[RNH_2][H^+]}{[RNH_3^+]} \\ \Rightarrow pH &= pK_a + lg\frac{[RNH_2}{RNH_3^+} \end{aligned} \tag{3.2}$$

All dendronized polymers were soluble in water and each generation was stored separately in a stock solution (5 mM HEPES, NaOH at pH 7.5) at a concentration of 12 ng/μl in the fridge.

3.3.1 Partially Deprotected Dendronized Polymers

In the case of partially deprotected dendronized polymers (up to 30 %) of generation two and four, the synthesise was also successfully carried out by L. Shu (Prof. A. D. Schlüter at the Free University, Berlin).

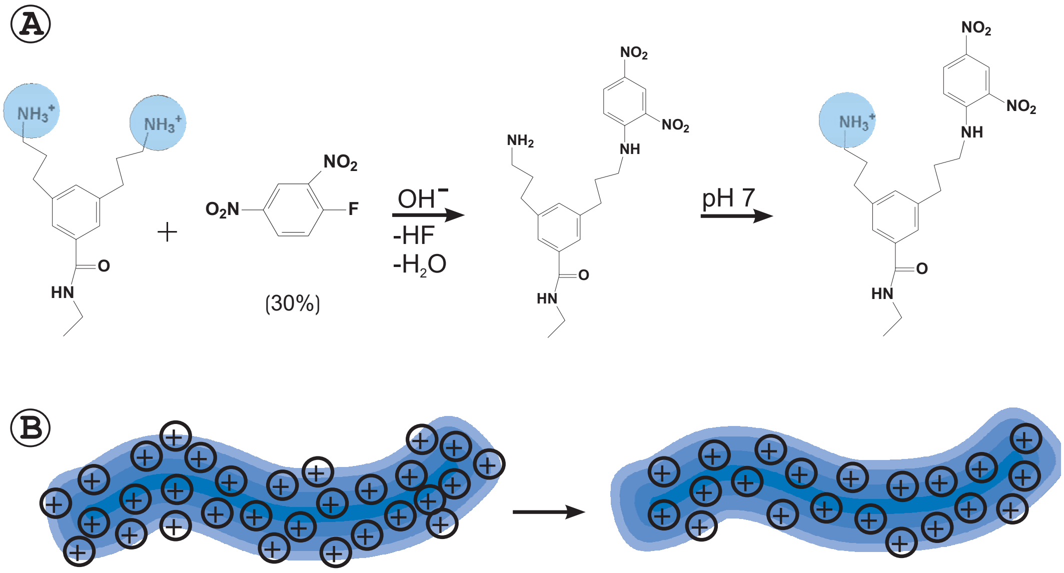

Figure 3.3: Partially deprotected dendronized polymers. A) Reaction of 2,4-dinitrofluorobenzene (Sanger reagent) with the terminal amine of the dendronized polymer. B) Reduction of surfaces charges along the dendronized polymer .

In order to obtain dendronized polymers that possess different linear charge densities but the same radii, the terminal charges on PG4 and PG2 were reduced. Several reaction steps have been carried out. At the end, the most successful method to reduce the charges of PG4 and PG2 was to react the Sanger reagent under basic conditions with the free amine (see Fig. 3.3), similar to the reaction that was carried out in order to determine the degree of coverage. Again, the reaction could be quantified by chromatography.

However, the maximum protection of terminal charges was 30% in aqueous solution. Otherwise, the dendronized polymers precipitated. Since the solubility of polymers in aqueous solution is charge dependent and the neutral counterparts of the dendronized polymers are not soluble in water but in organic solutions like chloroform [5].

3.4 SFM Apparatus

Scanning force microscopy (SFM) images were recorded using a MultiMode^{TM} Scanning Probe Microscope (Digital Instruments, Inc., Santa Barbara, CA) that was operated in tapping mode^{TM} [126]. Olympus etched silicon cantilevers possess a typical resonance frequency in the range of 200 − 400 kHz and a spring constant of 42 N/m.

In the experiments in this thesis, the NanoScope software is used for image analysis and presentation. The raw data were modified using the filter for flattening the images. This filter removes the vertical offset between scan lines (i.e. z-drift of the piezoelectric scanner). Here, the calculated least-square fit 0th order polynomial of each scan line is subtracted from its original scan line. Additionally, the use of higher order polynomials remove the tilt, the arch shaped, and the s-shaped bow in each scan line for 1st, 2nd, and 3rd order, respectively. Since the vertical offset between scan lines is removed, the information in y-direction of the image is not conserved. Thus, in order to make accurate cross sectional height measurements, the cross-sectional lines are only drawn along the scan direction (x-direction). The vertical profile along this line assures the accurate height measurement of the molecules [127].

3.4.1 Fluid Cell

The TappingMode^{TM} fluid cell (Digital Instruments, Inc., Santa Babara, CA) was used during all fluid SFM measurements. Here the O-ring was placed onto the sample and the polymer liquid was injected into the fluid cell. The volume of the included fluid was about 20 μl. The fluid cell was also used without O-ring. In this case the amount of the fluid varied. For all measurements in fluids, standard silicon nitride probes were used with a typical resonance frequency in the range of $5 - 20$ kHz and an approximate spring constants of 0.12 N/m.

3.5 Substrate

Substrates for SFM measurements should be atomically flat. Well known substrates are mica and highly orientated pyrolytic graphite (HOPG). While the surface of HOPG is highly hydrophobic, mica serves as commonly used surface for samples adsorbed from aqueous solutions [128].

Mica is characterized by its layered crystal structure. The mica structure is built from so called T-O-T (**T**etrahedral (Si, Al)$_2$O$_5$ - **O**ctahedral Al$_2$(OH)$_6$ - **T**etrahedral) layers. Between the adjacent T layers, an interlayer of cations is placed. In the case of muscovite mica these cations are K$^+$ ions. Between these layers the mica crystal can be easily cleaved using tape. The cleavage results in an atomically flat and clean basal plane over several hundreds of μm^2 [129]. The K$^+$ ions can be easily washed from the mica surface with water. Hence,

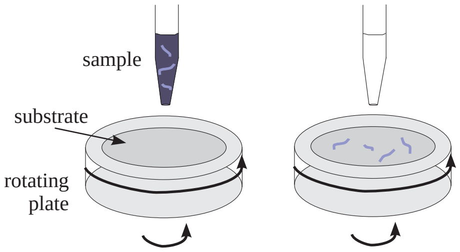

Figure 3.4: Spin coating.

the average cleaved surface of mica is negatively charged.

For substrates, freshly cleaved muscovite mica (PLANO W. Plannet GmbH, Wetzlar, Germany) or poly-L-ornithine coated mica were used throughout this study. For the coating, a freshly cleaved mica surface was placed onto a droplet of 5 μl of 0.1 mg/ml poly-L-ornithine solution for 5 minutes, rinsed three times with deionized water and then dried under a stream of N_2 gas. The coated substrates were used immediately. While freshly cleaved mica serves as a negatively charged surface [130], the polymer coated surface is positively charged [39].

3.6 Sample Preparation

There are different sample preparation techniques which are used in general in SFM experiments. In order to adsorb single molecules on the atomically flat substrate the following techniques had been used.

3.6.1 Spin Coating

This technique uses the balance of centrifugal force created by the spinning the substrate and viscous forces of the polymer solution. In the final stage, also evaporative forces have to be considered.

A droplet of sample solution is deposited onto a substrate which can be already spinning at a constant rate or is fixed and after some seconds accelerated into its final rotation speed (Fig. 3.4). The coating thickness depends on the rotation speed and the concentration of the sample solution. In all cases 50 rps was the predetermined rotation speed and the sample concentration was about 10 ng/μl to adsorb single macromolecules.

3.6.2 Droplet Adsorption

The substrate was placed onto a droplet of diluted stock solution for 5 minutes, rinsed three times with deionized water and then dried under a stream of N_2 gas (Fig. 3.5). The advantage of this technique is that the molecules are allowed to adsorb onto the substrate and are not expelled by spinning and thereby defractionated [7]. The deposition procedure was the same for all molecules:

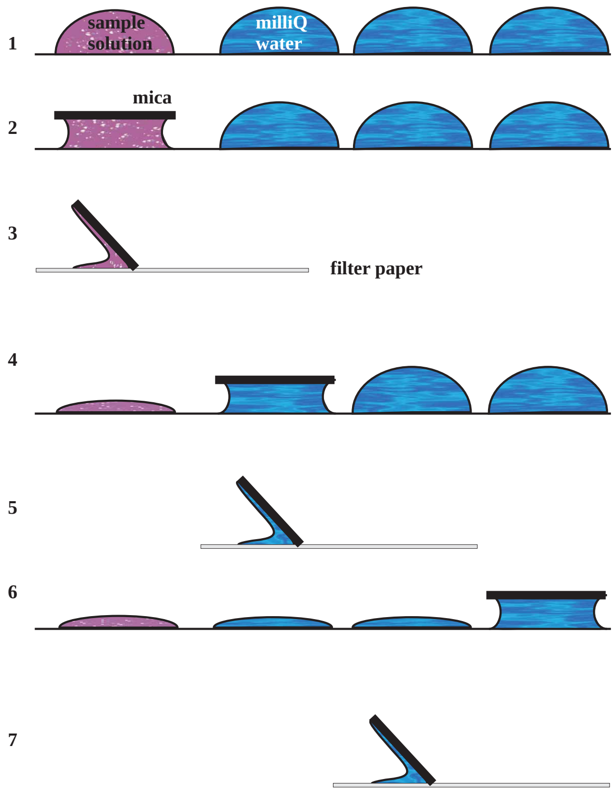

Figure 3.5: Droplet adsorption. Step 1: Droplets are placed onto a clean surface (parafilm). Step 2: Freshly cleaved mica or coated mica surface is placed for 5 minutes on top of the sample solution. Step 3: The solution is absorbed with a filter paper. Step 4: The surface is washed three times using droplets of MilliQ water and after each step the dispensable solution is absorbed with a filter paper again (steps 5-7). At the end the surface is gently dried under a stream of N_2.

- **Dendronized Polymers**
  For the deposition of isolated dendronized polymers, a freshly cleaved mica substrate was used and the stock solution was diluted to 3 ng/μl of dendronized polymers.

- **DNA**
  DNA molecules were deposited either onto poly-L-ornithine coated mica substrates from a buffer solution [5 mM HEPES, NaOH at pH 7.5] diluted to a DNA concentration of 1 ng/μl or on freshly cleaved mica surface. Here, the negative charges of mica and DNA were bridged by mobile Mg^{2+} ions from a $MgCl_2$ solution (5 mM $MgCl_2$, 5 mM HEPES, NaOH at pH 7.5).

- **Complexes of DNA and Dendronized Polymers (no NaCl)**
  DNA/dendronized polymer complexes were formed by adding an appropriately diluted dendronized polymer stock solution to a DNA solution [10 ng/μ l DNA in 5 mM HEPES, NaOH at pH 7.5]. This preparation is the same whatever type of dendronized polymer or DNA was used with respect to the different experiments. Using different dilutions of dendronized polymer solutions the requested charge ratios of DNA/dendronized polymer could be set to $1/10, 1/5, 1/1$ through 1/0.2, taking into account that 1 ng DNA contains 1.9×10^{12} negative charges and 1 ng PG2, PG3 and PG4 dendronized polymers contains 2.9×10^{12} positive charges (see section 3.3). The charge of partially protected PG4s and PG2s was decreased by 30 % (see section 3.3.1).

  After the addition of the dendronized polymer solution to the DNA solution, the mixed solution was shaken for 1 minute. Longer preparation times of about 10 minutes did not give different results. Each DNA/dendronized polymer solution was allowed to adsorb onto freshly cleaved and poly-L-ornithine coated mica substrate.

- **Complexes of DNA and PG2 (added NaCl)**
  $\mathbf{10, 50, 100, 300}$ and 600 mM NaCl. The PG2 solution was diluted using a NaCl solution such that the total volume of PG2 and linearized pUC19 DNA stock solution resulted in the requested NaCl concentration and charge ratio of 1/0.7. Then, the sample was prepared as described above.

  2.4 M NaCl. The PG2 stock solution was added to the DNA stock solution such that the charge ratio of 1/0.7 was obtained. Then, the DNA/PG2 solution was shaken for 1 minute and an appropriate NaCl solution was added to reach an overall concentration of 2.4 mM NaCl. The used volumes and concentrations were adjusted to reach the standard concentration of complexes without added NaCl that is described above. After incubation times of 30 and 60 minutes, the solution was allowed to adsorb on poly-L-ornithine coated mica substrates as described above.

3.7 Data Analysis

3.7.1 Contour length

For the quantitative determination of the contour lengths of single molecules SFM images were recorded with a resolution of 512×512 pixels for (1000×1000) nm^2 or (500×500) nm^2 (i.e. ranging from $1 - 2$ nm/pixel). Using the drawing program *sketch (www.sketch.sourceforge.org)*, the contour of each single molecule was divided into straight segments of 2-5 nm.

The measured lengths are corrected for the error due to the effect of tip broadening (section 2.5.6), assuming the calculated heights of the dendronized polymers and complexes (Equ. 3.1) and a tip radius of 7.5 nm [101].

3.7.2 Height Measurements

From the SFM images height measurements were based on the cross sectional profiles of the DI software as described in section 3.4.

Chapter 4

Results and Discussion

In the first section, this chapter characterizes the single components that are used for complex formation like dendronized polymers (section 4.1) and DNA (section 4.2) on their own. Then, the interactions between these components are discussed (sections 4.3 and 4.4). Finally section 4.5 summarizes the results obtained by the influence of salt on the complex formation. All sections end with a discussion of the results.

4.1 Dendronized Polymers

To characterize single dendronized polymers (PG1, PG2, PG3 and PG4), they were deposited onto freshly cleaved mica, visualized via SFM (Fig. 4.1 and Fig. 4.2) and analyzed by measuring their contour length distributions and heights. The sample preparation is described in section 3.6. All samples were measured at room temperature in air environment.

To make sure to work with optimized tapping conditions in order to receive high resolution images of dendronized polymers, the influence of Q-control was investigated (see section 2.5.5). Furthermore, knowing the systematic errors of SFM measurements (section 2.5.6), also cryo-TEM measurement on dendronized polymers were carried out. Therefore, a direct comparison between the diameters of the dendronized polymers was possible.

Discussing the influence of salt on the complex formation between dendronized polymers and DNA, the influence on the single components have to be investigated first. Therefore, experiments with dendronized polymers in high salt solutions have been carried out. The same argument holds for the characterization of partially protected dendronized polymers, that are discussed in this section. Finally, they will be used to study their influence on the complex

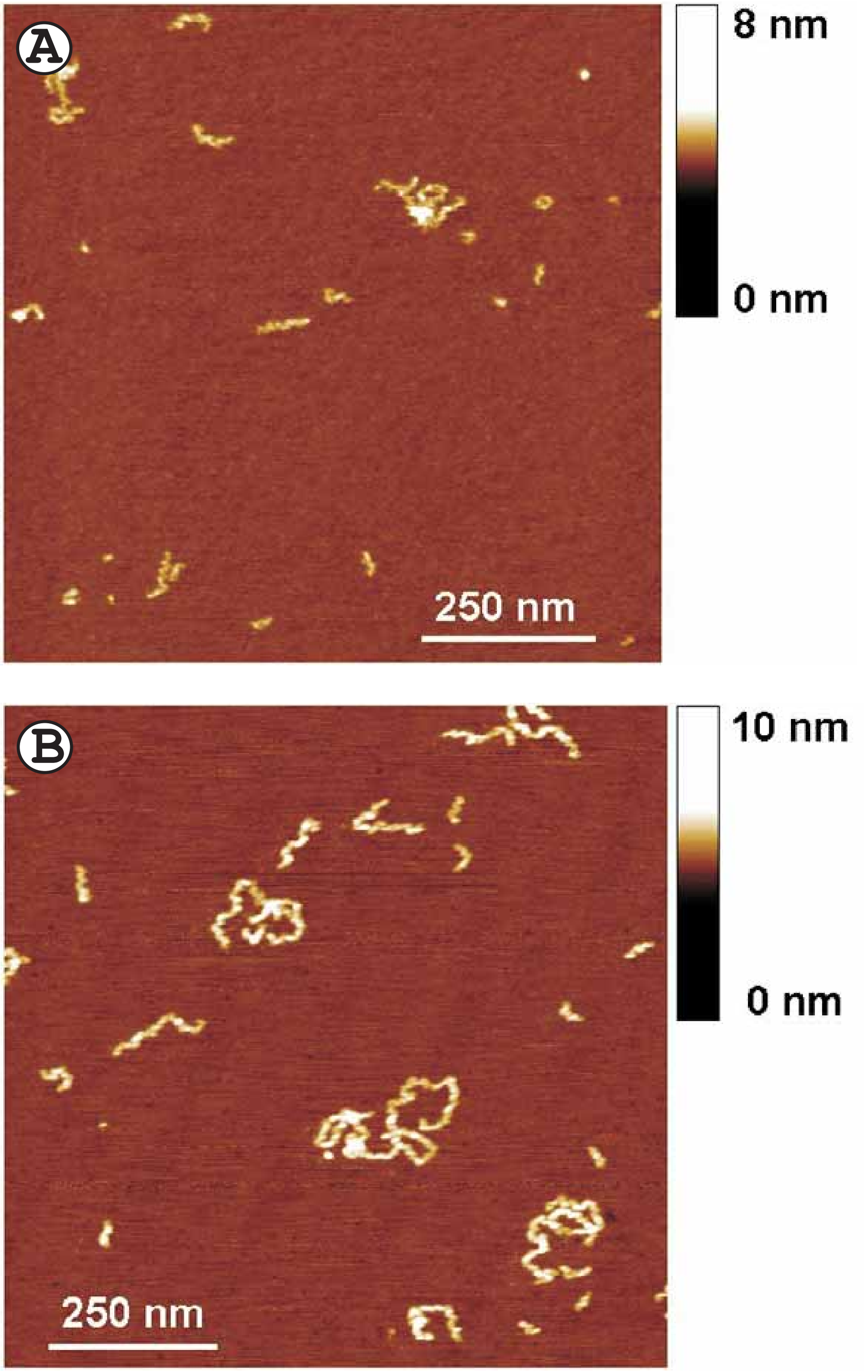

Figure 4.1: High resolution SFM images of dendronized polymers PG1 (A) and PG2 (B) deposited onto freshly cleaved mica.

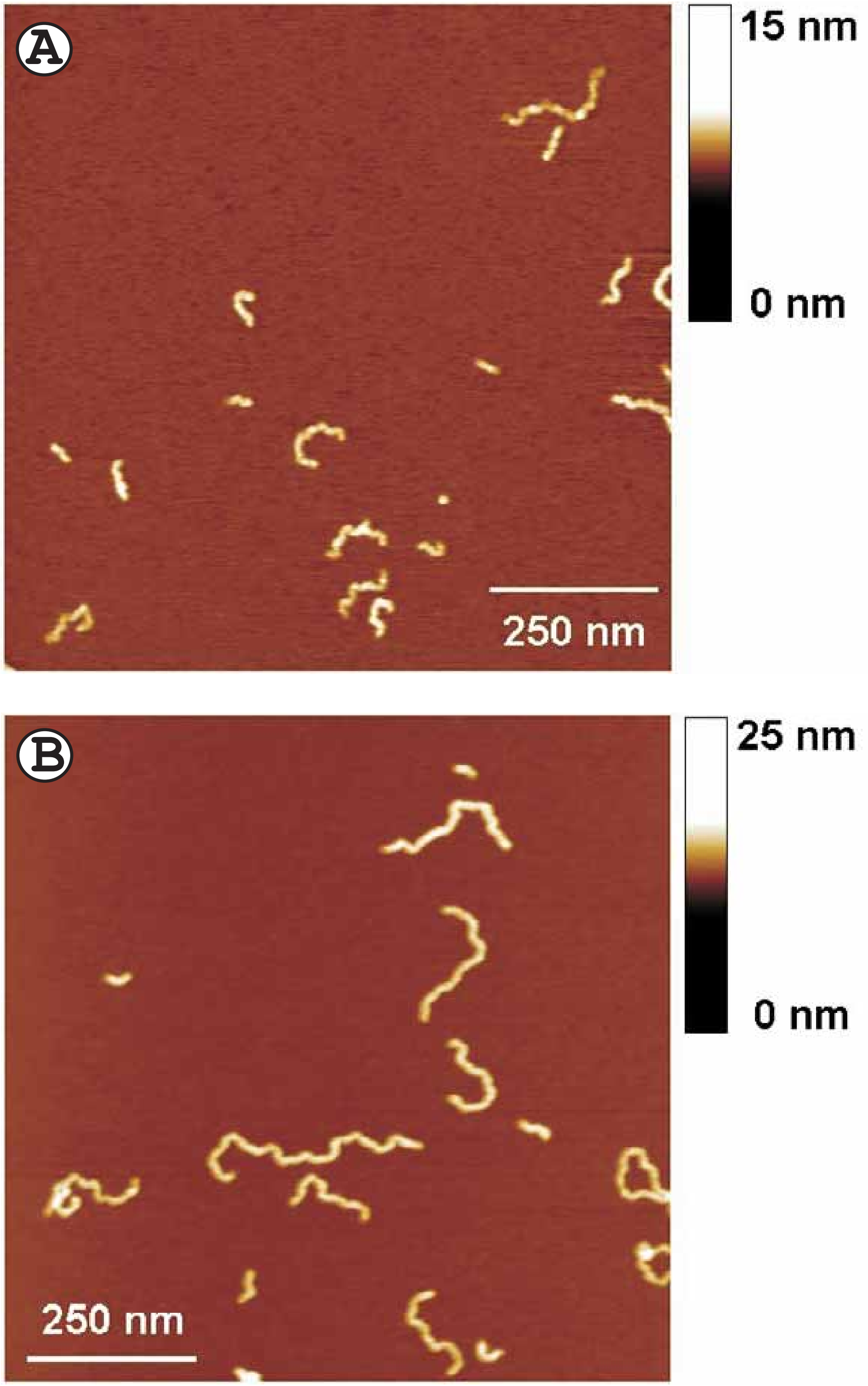

Figure 4.2: High resolution SFM images of dendronized polymers PG3 (A), and PG4 (B) deposited onto freshly cleaved mica.

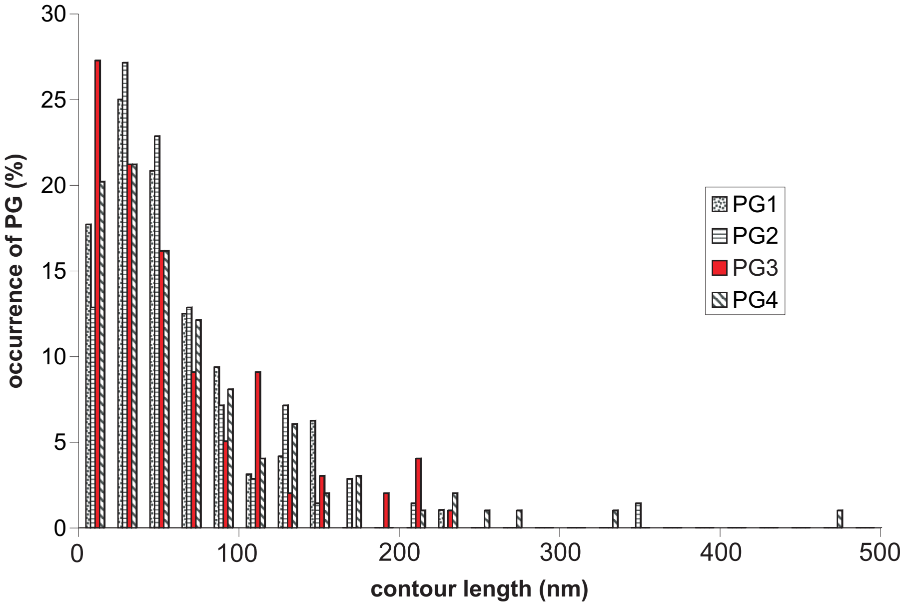

Figure 4.3: Contour length distribution of dendronized polymers of generation 1, 2, 3, and 4.

morphology of the complex with DNA.

4.1.1 Contour Length Distribution

For the analysis, only such molecules were selected which possessed two clearly recognizable ends. The histograms of the contour lengths of about 100 molecules of PG1, PG2, PG3 and PG4 are displayed in Fig. 4.3. For the definition of the counter length see section 2.6.2.

The fact that almost all distributions exhibit a decrease in the numbers of molecules in the smallest contour length interval, can be explained with the selection process mentioned above: If the molecules are smaller than 20 nm, it is very difficult to distinguish between really extended single molecules and coiled ones or any other contamination. Therefore most of these cases have not been considered which leads to a relatively high systematic error for the data in the first interval. Due to the finite resolution of the imaging, the procedure of vectorizing the contour of single molecules (see section 3.7.1) may underestimate the contour length. Since the bulkiness (see section 3.3) of the dendrons increases from generation 1 to 4, the resolution of the lightly meandred backbone image decreases (Fig. 4.1 and Fig. 4.2).

Table 4.1: The number averaged molecular length $< L_n >$, the weight averaged molecular length $< L_w >$ and the length polydispersity PD of all dendronized polymers.

System	$< \mathbf{L_n} >$ (nm)	$< \mathbf{L_w} >$ (nm)	$\mathbf{PD} = \frac{<\mathbf{L_w}>}{<\mathbf{L_n}>}$
PG1	57	88	1.54
PG2	64	110	1.72
PG3	60	119	1.98
PG4	73	152	2.08

The number averaged molecular length $< L_n >= \sum N_i l_{C_i} / (\sum N_i)$, the weight averaged molecular length $< L_w >= \sum N_i l_{C_i}^2 / (\sum N_i l_{C_i})$ and the length polydispersity $PD =< L_w > / < L_n >$ as defined in section 2.6.1 were calculated and listed in Table 4.1.

4.1.2 Height Measurements

The average height of PG2, PG3 and PG4 from tapping mode images was (1.8 ± 0.3) nm, (2.4 ± 0.4) nm and (3.0 ± 0.3) nm, respectively. A well known feature of the SFM is the underestimation of the original height of molecules (see section 2.5.6). Thus, these values have to be discussed rather in comparison to each other than as absolute values.

4.1.3 Q-Control

The Q-control was used in order to increase the image resolution as described in section 2.5.5 for example of PG4. PG4s were chosen because of their bulkiness due to their high generation (see Fig. 4.1 and Fig. 4.2). In Fig. 4.4 a direct comparison between DI-tapping mode and Q-control tapping mode images is given. In the high resolution images (Fig. 4.4b and e) cross sectional profiles show the height modulation of the meandred backbone with a period of about 11 nm in both cases (Fig. 4.4c and f). Thus, the resolution of PG4s obtained from tapping mode operation is comparable to Q-control experiments, using optimized scan parameters (small drive amplitude as well as slow scan speed).

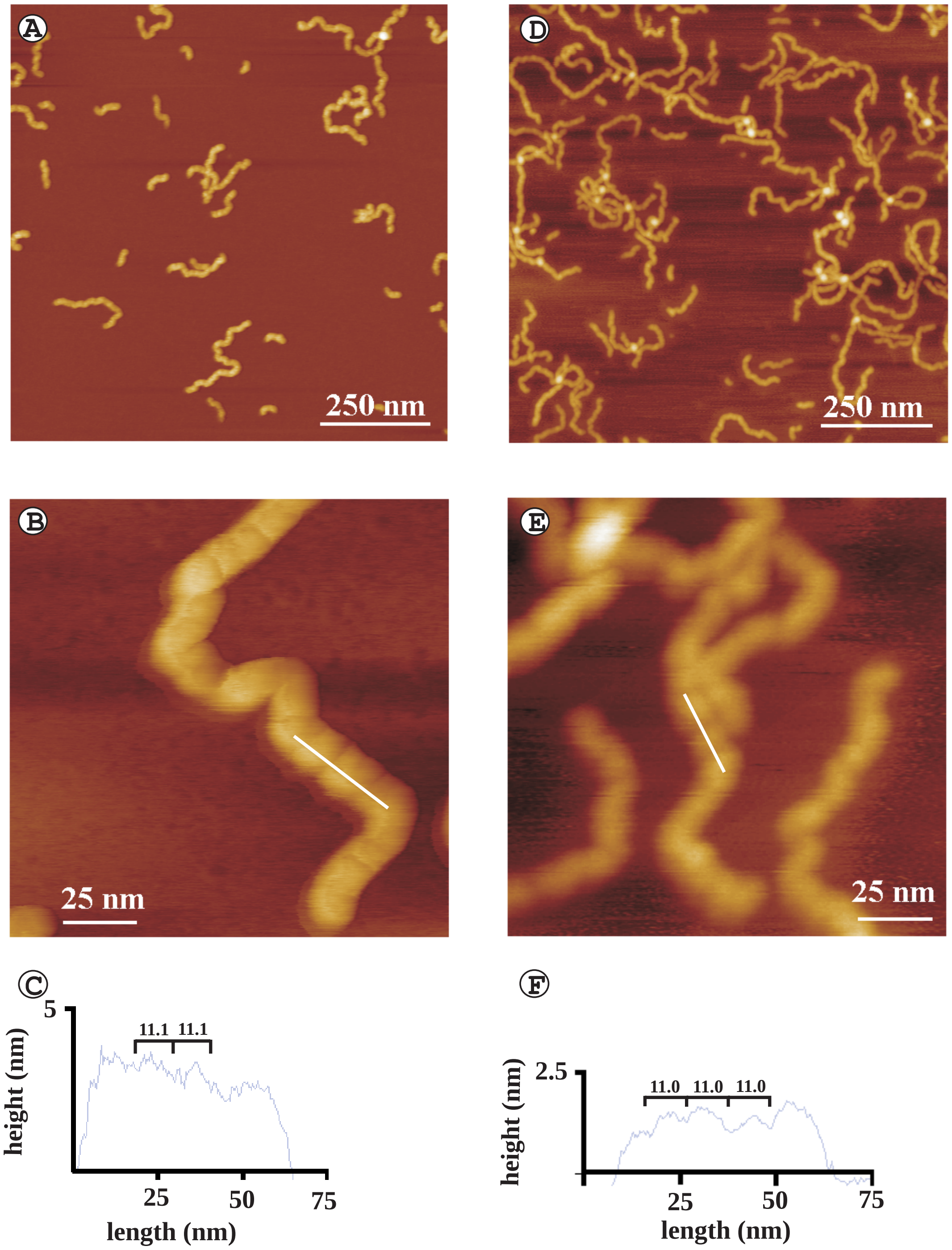

Figure 4.4: Comparison of tapping mode SFM and Q-control images. A) Tapping mode SFM image of PG4 molecules on mica using a small drive amplitude (<30 mV) and a scan rate of 1 Hz. B) High resolution SFM image with the same parameters. C) Line scan indicated in B). D-F) Corresponding images using Q-control.

4.1.4 Cryo-Transmission Electron Microscopy (Cryo-TEM)

Air dried and stained (1 % uranyl acetate), as well as cryo-electron microscopical examinations of PG2, PG3 and PG4 were performed by Dr. Ch. Böttcher and Dr. B. Schado, FU Berlin, Germany (Fig. 4.5). The molecular diameters were measured and summarized in Table 4.2. PG3 and PG4 were examined with both techniques. Depending on the different techniques the diameter of PG3 varied significantly whereas for PG4 the diameter stayed the same within the errors. Due to the staining and drying process of the sample an increase in the diameter of PG3 can be explained. In the case of PG4 this increase in the diameter due to the different preparation technique did not occur. Nevertheless, the diameter of PG3 and PG4 obtained from the cryo-micrographs is the more reliable one [131].

Table 4.2: Comparison of diameters of dendronized polymers obtained from air dried stained and cryo microscopical examinations, average heights from SFM measurements, and calculated diameters (Eq. 3.1).

System	Diameter Stain and Dried (nm)	Diameter Cryo (nm)	Height SFM (nm)	Diameter Theoretical (nm)
PG2	4.0 ± 1.0	–	1.8 ± 0.3	3.2 ± 0.3
PG3	6.5 ± 1.0	4.0 ± 1.0	2.4 ± 0.4	4.6 ± 0.5
PG4	7.9 ± 1.0	8.2 ± 0.5	3.0 ± 0.3	6.6 ± 0.7

4.1.5 Influence of NaCl

Single PG2s adsorbed from a 2.4 M NaCl solution only on poly-L-ornithine coated mica surfaces. In Fig. 4.6 a comparison to single PG2s from a buffer solution on mica using the same tapping parameters and the same tip is given. While the average height for PG2 from these images amounts to (1.8 ± 0.3) nm, the average height for PG2 at 2.4 M NaCl on poly-L-ornithine coated mica was a little bit higher (2.0 ± 0.4) nm, but the same within the errors. Since the aggregation between single PG2s at 2.4 M NaCl was relatively high, contour length measurements seemed to be not reasonable.

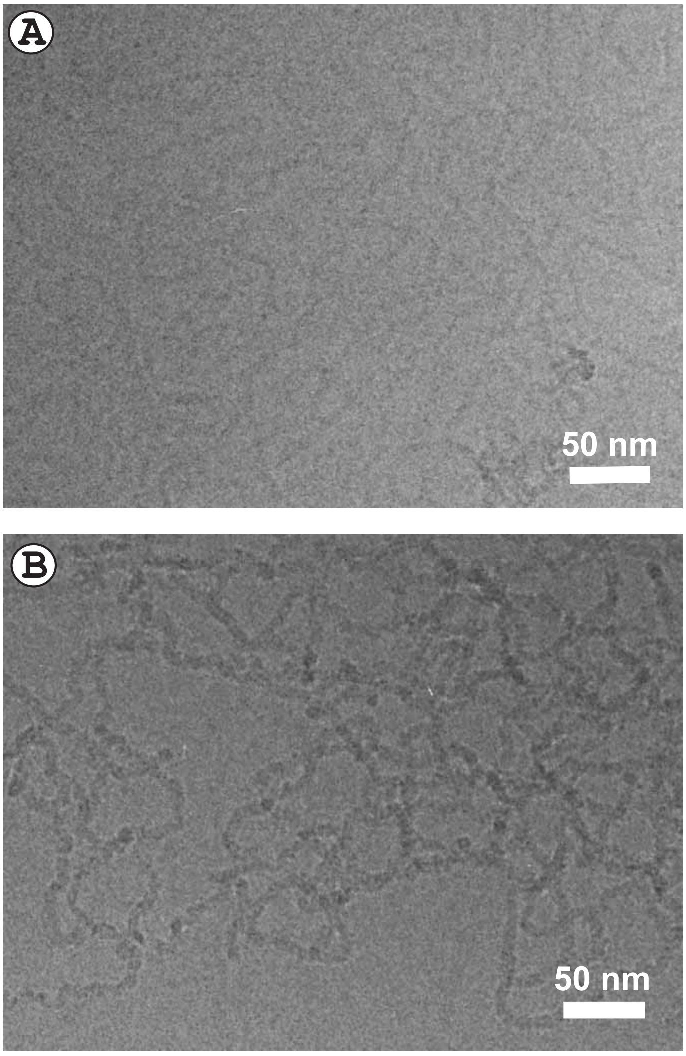

Figure 4.5: Cryo-TEM images of A) PG3 and B) PG4

4.1.6 Partially Protected Dendronized Polymers

Single 30% protected PG2s (PG2%) and PG4s (PG4%) are visualized on mica in Fig. 4.7. In general, the formation of aggregates of these partially protected dendronized polymers occurs more often compared to their fully charged counterparts. In addition, the highly meandred backbone seems to be highly enhanced, especially for the PG4%. The average height of PG2% amounts to (2.6 ± 0.7) nm and of PG4% to (8.7 ± 1.2) nm.

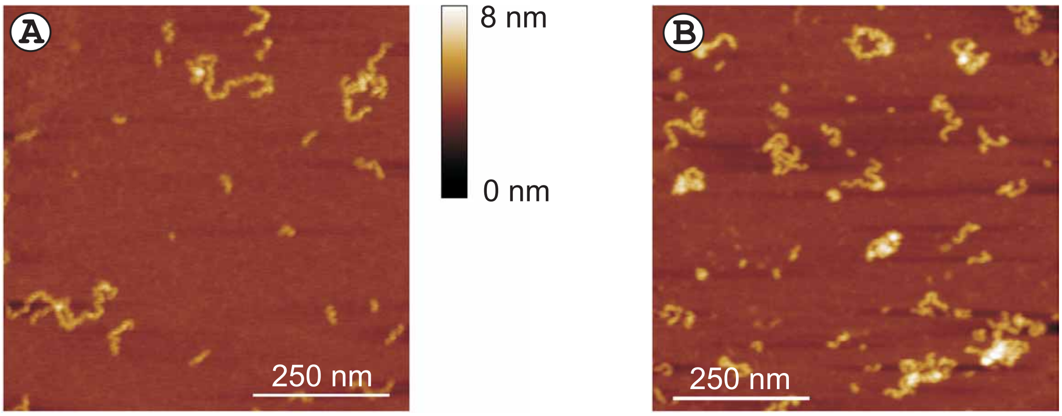

Figure 4.6: Comparison of single PG2s adsorbed from different NaCl concentrations. A) PG2 from 0 M NaCl on mica (see also Fig. 4.1b). B) PG2 from 2.4 M NaCl on poly-L-ornithine coated mica.

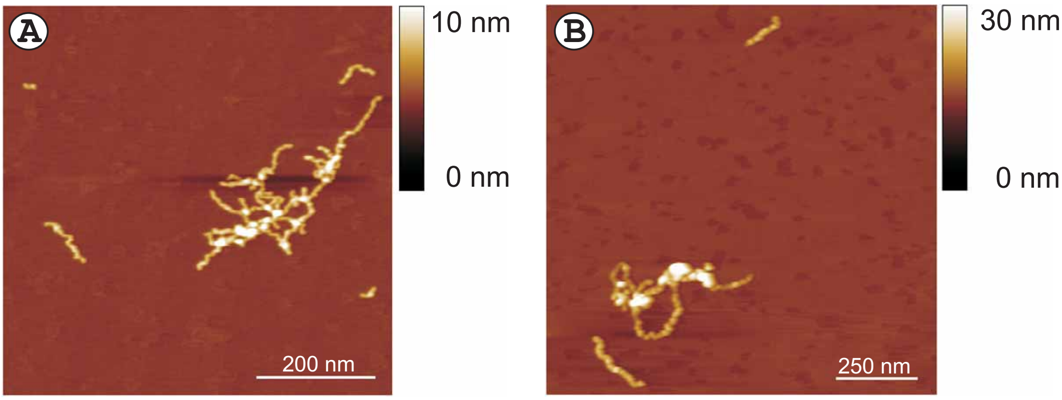

Figure 4.7: SFM images of single partially protected dendronized polymers. A) Single PG2% and B) PG4% adsorbed on mica surface.

4.1.7 Discussion on Dendronized Polymers

SFM is a powerful tool to determine the dimensions of macromolecules. The macromolecules can be directly visualized on a surface, while using techniques such as small-angle X-ray scattering or dynamic light scattering only model dependent size information is provided. Despite the advantages of SFM, one should be aware of the influences on the results caused by tip-sample and sample-substrate interactions (section 2.5.6).

Comparing the statistical distribution averages of dendronized polymers of generations 1, 2, 3, and 4, a quasi homologous series is found (Table 4.1). Thus, this result verifies the successful synthesis of PG2, PG3, and PG4 from the same core dendronized polymer PG1. The increase of $< L_w >$ with increasing dendron generations is mainly due to the occurrence of more very long molecules for the higher generations (Fig. 4.2). This observation may be explained by different reasons: First, the decrease of charge density on the dendrimer by decreasing dendron generations may cause preferred aggregation of the long low generation polymers which are therefore not resolvable as single molecules anymore. Second, since the supernatant solution is rinsed during preparation, long chains may be missing due to the faster adsorption kinetics for the smaller ones [132]. Nevertheless, fractionation of the molecules as it is reported by M. Gerle et al. [7] in the case of spin casting sample preparation for cylindrical brushes, is not observed in this case, since here, the droplet sample preparation was used. For the differences in these sample preparation techniques see section 3.6. On the other hand, due to the decreasing resolution of the backbone image with increasing dendron generation, the average contour length should also decrease. However, this influence could be almost excluded by artificially smearing the original SFM data in the case of lower generation.

The actual diameter of the dendronized polymers cannot be given exactly by either SFM height measurements nor TEM experiments. While in the first case the SFM underestimates the molecules dramatically (section 2.5.6), the air dried stained TEM experiments overestimate it slightly due to the preparation technique. Although the diameters measured with cryo-TEM are experimentally the most reliable ones, the measurement of PG2 is still under investigation. Thus, as a lower limit the volume based, theoretically estimated diameters that are also listed in Table 4.2 were taken for the analysis. An upper limit of the diameter, that includes the architecture and swelling of the dendronized polymers, is discussed in section 4.5.3.

Q-Control compared to tapping mode SFM results did not change for PG4 as the lateral resolution is concerned. However, for other systems in which the sample-substrate interaction is not as strong or for even softer samples, the use of Q-Control might increase the tapping conditions extremely [133], see section 2.5.5. Depending on the system it can be useful to use Q-Control or not [134]. Regarding the scanning conditions in the present case, the tip-sample compared to the sample-substrate interaction was not as strong as moving the molecules on the surface while scanning, and furthermore, the resolution did not increase by the additional use of Q-control. Thus, for further investigation, Q-Control was not used.

Single, partially protected dendronized polymers could be visualized on mica.

Contour length distributions were not measured, because of their strong aggregation. The measured averaged height of both generations is significantly increased compared to the fully deprotected counterparts. Additionally, the meandering of the backbone is much more pronounced, especially for PG4%. Thus, because the surface charge is reduced, the electrostatic repulsion between the charged endgroups gets also reduced. While the stiffening of the backbone of dendronized polymers is given by a steric as well as electrostatic repulsion, the electrostatic contribution gets weakened in the case of partially protected dendronized polymers. The stiffening, i.e. stretching, of the backbone gets reduced and thus, the backbone is allowed to shrink, which will result into the observed thicker polymers and pronounced meandering of the contour.

The theoretical diameter of the 30 % protected dendronized polymers can be estimated as followed: The linear charge density of the dendronized polymers is assumed to be fixed at $\tau_i = 16\mathrm{e}^-/0.25$ nm and $\tau_i = 8\mathrm{e}^-/0.25$ nm for $i = \mathrm{PG4}$ and PG2, respectively. In the case of 0 % protected charges, this equals the charges per repeat unit for the different generation (see section 3.3.1). Thus, for PG2 the 4 positive charges per repeat unit are reduced to 2.8 (70 %) and for PG4 the 16 charges to 11.2 (70 %). If 30 % of the charges are protected, a larger amount of the backbone length l'_i should fit into a given distance in order to maintain τ_i. Thus, the volume V_i (fixed distance l) will increase which is demonstrated in Fig. 4.8. On the other hand, the volume V'_i of the polymer with a length of the backbone of l'_i nm using Eq. 3.1 can be calculated. Fixing this volume V'_i to the length of $l = 0.25$ nm, the requested diameters $2r'_i$ become $V'_i = \pi l r'^2_i \Rightarrow 2r'_i = 2\sqrt{V'_i/(\pi l)}$.

The measured heights and calculated diameters of the different systems are summarized in Table 4.3.

Table 4.3: Measured average heights and calculated diameters of the different polymers. The diameters are calculated based on the theoretical volume in Eq. 3.1.

polymer	**0%** protected		**30%** protected		**100%** protected	
	diameter theoretical (nm)	height SFM (nm)	diameter theoretical (nm)	height SFM (nm)	diameter theoretical (nm) [135]	height SFM (nm) [135]
PG2	3.2 ± 0.3	1.8 ± 0.3	3.8 ± 0.4	2.4 ± 0.7	4.8 ± 0.5	1.8 ± 0.1
PG4	6.6 ± 0.7	3.6 ± 0.3	7.9 ± 0.8	8.7 ± 1.2	9.2 ± 0.9	2.4 ± 0.2

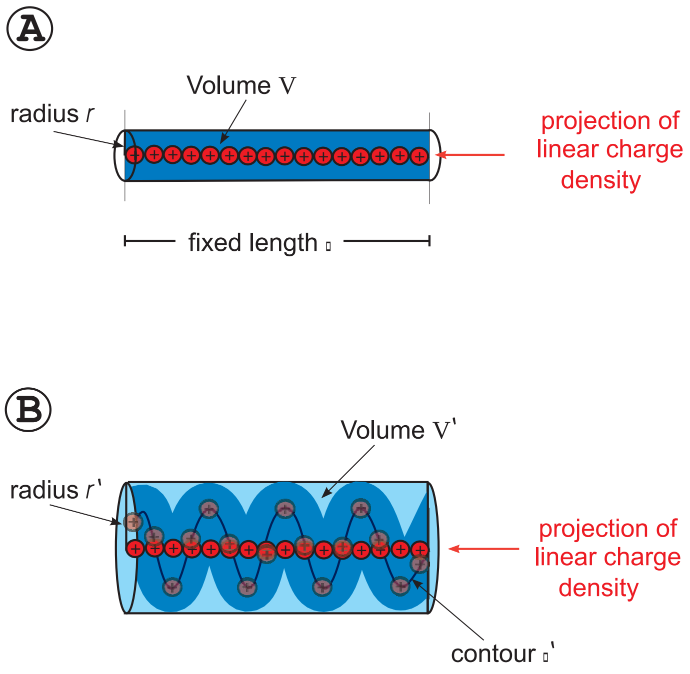

Figure 4.8: Model for 30 % protected dendronized polymers, demonstrated for PG4%. A) A fixed length l of PG4 with 0 % protected positive charges. B) Pronounced meandering of the PG4% results in the same linear charge density per given length l but increasing volume V'.

Additional, the data of 100% protected dendronized polymers that are investigated by Ch. Ecker [135] are listed. Here, the molecules are measured on HOPG from a tetra-hydrofuran (THF) solution and the theoretical diameter is estimated from the lamellar spacing of adsorbed molecules. In the case of PG2% the theoretical diameter is much higher than the measured one from the SFM data. In contrast, the theoretical diameter of PG4% is smaller than the measured height in the SFM. Because of tip/sample interaction, the height from the SFM should be smaller than the real diameter. Therefore, especially in the case of PG4% the meandering might be much more pronounced than according to the discussed model. In the case of 100 % protection, the theoretical diameter is even higher.

4.2 DNA

DNA has been investigated in many SFM studies [103]. On the one hand biologists are interested to visualize different DNA interactions [104]. On the other hand, DNA has been used to test adsorption theories as a well characterized semi-flexible polyelectrolyte using the SFM [111]. In the following, single DNA molecules are characterized as prepared by different techniques. Also the imaging of DNA in the fluid cell of the SFM is demonstrated.

4.2.1 DNA in Air

The contour length distribution of linear pUC19 and linear 213 bp DNA showed that the molecules were almost monodisperse with an average length of (844 ± 66) nm and (66 ± 10) nm (Fig. 4.9c). Due to mechanical stress during preparation steps a small amount of about 12 % of all DNA molecules was damaged in both samples.

The apparent persistence length of DNA molecules adsorbed onto mica substrates precoated with positively charged poly-L-ornithine was (15.4 ± 0.5) nm, as determined by a shape analysis [136]. It is smaller to that of DNA molecules adsorbed on untreated mica from a $MgCl_2$ - solution ($P = 53$ nm). In Fig. 4.9a, b the difference can be seen qualitatively. The difference suggests that DNA molecules adsorbed on poly-L-ornithine treated mica are kinetically trapped on the surface [111].

SFM images of circular pUC19 (2686 bp) as well as circular pBR325 (5994 bp) plasmid DNA showed relaxed DNA molecules (Fig. 4.10). Consequential, almost all supercoiled plasmid DNA molecules converted into open circular plasmids during storage [137] and preparation.

The height of the DNA molecules in tapping mode was (0.7 ± 0.1) nm, which is comparable to earlier experiments (e.g. [94]).

4.2.2 DNA in Fluids

DNA has been adsorbed from a $MgCl_2$ buffer onto a mica surface. During the scanning process, it can be observed that the DNA molecule is not tightly bound to the surface rather some loops are still moving. Fig. 4.11 shows two successive images of a circular plasmid DNA in the fluid cell. The whight arrow in Fig. 4.11a indicates a loop which seems to be sticking out into the fluid and in Fig. 4.11b already adsorbed to the surface. Whereas the grey arrow in Fig. 4.11b indicates a loop that was bound before but now is released.

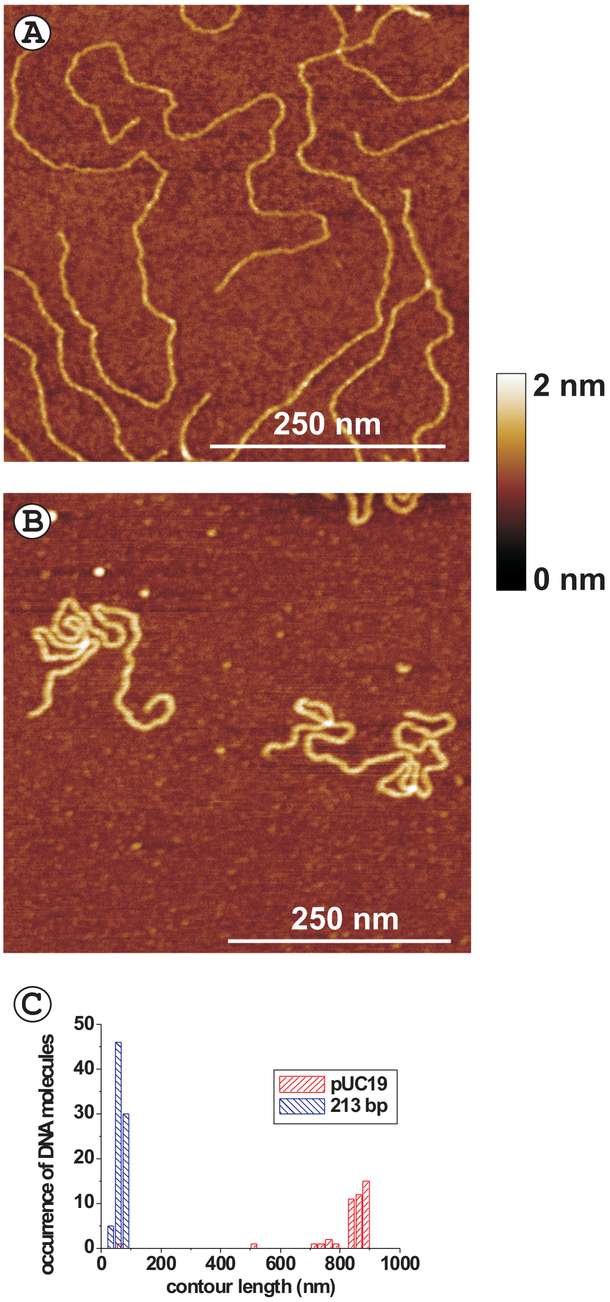

Figure 4.9: Comparison of different preparation techniques for DNA adsorption. A) Linear pUC19 precipitated onto mica from a $MgCl_2$ solution. B) Linear pUC19 adsorbed onto mica surface that was precoated with poly-L-ornithine. C) Contour length distributions of linear pUC19 and 213 bp DNA.

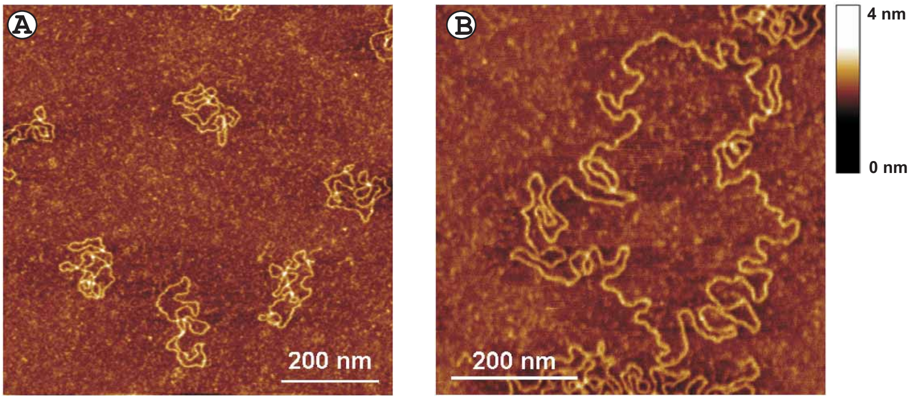

Figure 4.10: Open circular plasmid structures. A) Circular pUC19 plamid DNA and B) circular pBR325 adsorbed on a poly-L-ornithine coated mica surface. In both cases the circular plasmid DNA adsorbed in a relaxed rather than supercoiled form.

4.2.3 Discussion on DNA

The most commonly used substrate for imaging DNA in the SFM is mica. For the adsorption of negatively charged DNA on negatively charged mica (section 3.5) either divalent cations or positively coated mica surfaces are used. In the first case, the DNA molecules adsorb from a buffer solution containing 5 mM $MgCl_2$ that induces bridges between the negatively charged mica surface and the negatively charged DNA phosphates. The other possibility is to immobilize the DNA molecules on top of a layer of positively charged poly-L-ornithine on mica (see section 3.2).

During deposition, the conformation of DNA molecules reduces from three dimensions to two dimensions. Therefore, either the molecules can freely equilibrate, or they can adsorb without equilibration on the surface during the deposition process. In the latter case the molecules are kinetically trapped and it is difficult to distinguish between intrinsic conformations of the molecule and those induced by the surface adsorption. The determination of DNA persistence lengths in the experiments from a $MgCl_2$-buffer solution onto mica and onto poly-L-ornithine coated mica reveal an equilibrated and kinetically trapped deposition process, respectively. While the persistence length in the first case ($l_{eff} = 53$ nm) is in good agreement with values obtained by light scattering [138] and previous SFM studies [111], on poly-L-ornithine the persistence length of DNA molecules deviate ($l_{eff} = 15$ nm). Here, the molecular conformation resembles more a three dimensional projection on the surface rather than an equilibrated two dimensional state (see [111]). In order to avoid additional effects on complex formation due to divalent ions that will be

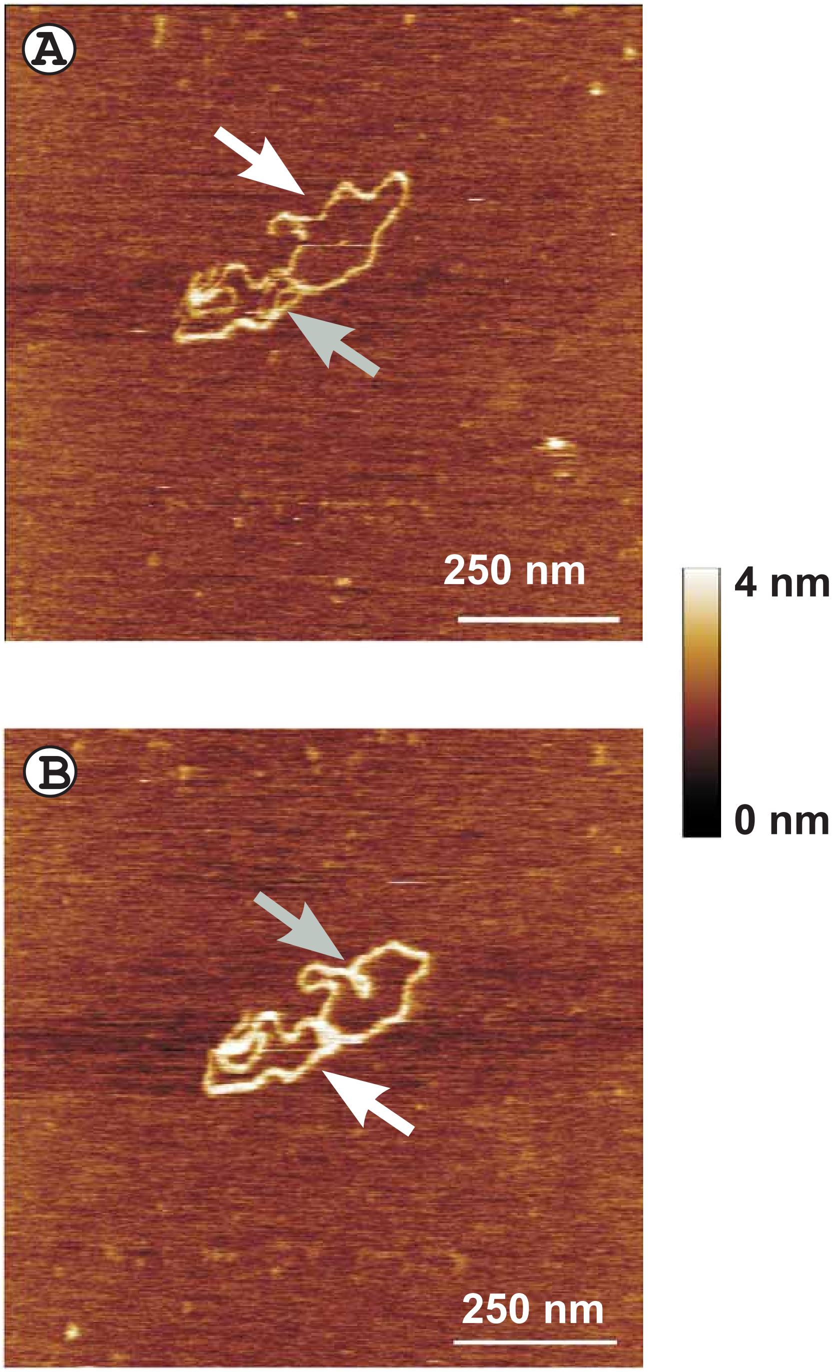

Figure 4.11: Fluid cell SFM measurements on DNA molecules. Sequence of two one after another SFM images of the same circular plasmid pUC19 molecule in the fluid cell. The arrows indicate loops of DNA that are occasionally adsorbed on the surface or released in the fluid.

present for experiments using a $MgCl_2$-buffer solution, poly-L-ornithine coated mica substrates are used. According to the experiments the molecules will be in a trapped configuration but the interfering influence of divalent ions during complexation is avoided.

According to 2682 bp of linear pUC19 and linear 213 bp DNA the calculated contour length should be 906 nm and 72 nm, respectively, using 3.38 Å/bp from section 2.1. The measured lengths amount to (844 ± 66) nm and (66 ± 10) nm, for linear pUC19 and linear 213 bp DNA, respectively. Both values are a little bit smaller than the predicted ones, but within the errors, the measured contour lengths are as expected and comparable to results obtained in the literature [139].

Fluid cell measurements show that DNA molecules are loosely bound to the mica surface in the case of a pure $MgCl_2$ solution but can be strongly fixed to the surface as soon as $NiCl_2$ is added to the solution [53]. It has been shown in previous studies, that the strength of the DNA adsorption on mica depends on the radius of the divalent cations in order to fit into the cavities in the mica lattice [140].

4.3 Adsorption of DNA on a Flat Dendronized Polymer Layer

Well known examples to immobilize DNA molecules for successful imaging via SFM are cationic lipid membranes [118] [119] [120], which fix the DNA molecules to the substrate through electrostatic attraction.

Similarly, the positively charged dendronized polymers and the negatively charged DNA molecules should interact through electrostatic forces with each other. To demonstrate this electrostatic attraction in aqueous solution experimentally, DNA was adsorbed onto a dendronized polymer coated mica surface in the fluid cell (Fig. 4.12a).

DNA molecules adsorb on top of a layer of dendronized polymers in the fluid cell Fig. 4.12b-d. Once adsorbed to the polymer coated surface, the DNA molecules did not change their overall conformation for long scan times nor high resolution imaging, but they were hard to visualize (Fig. 4.12b-d). The noisy structures of the DNA molecules in the image are well known features for molecules which are moving. In these experiments, the movement of the DNA strands might be local fluctuations x- and y-direction and also in z-direction

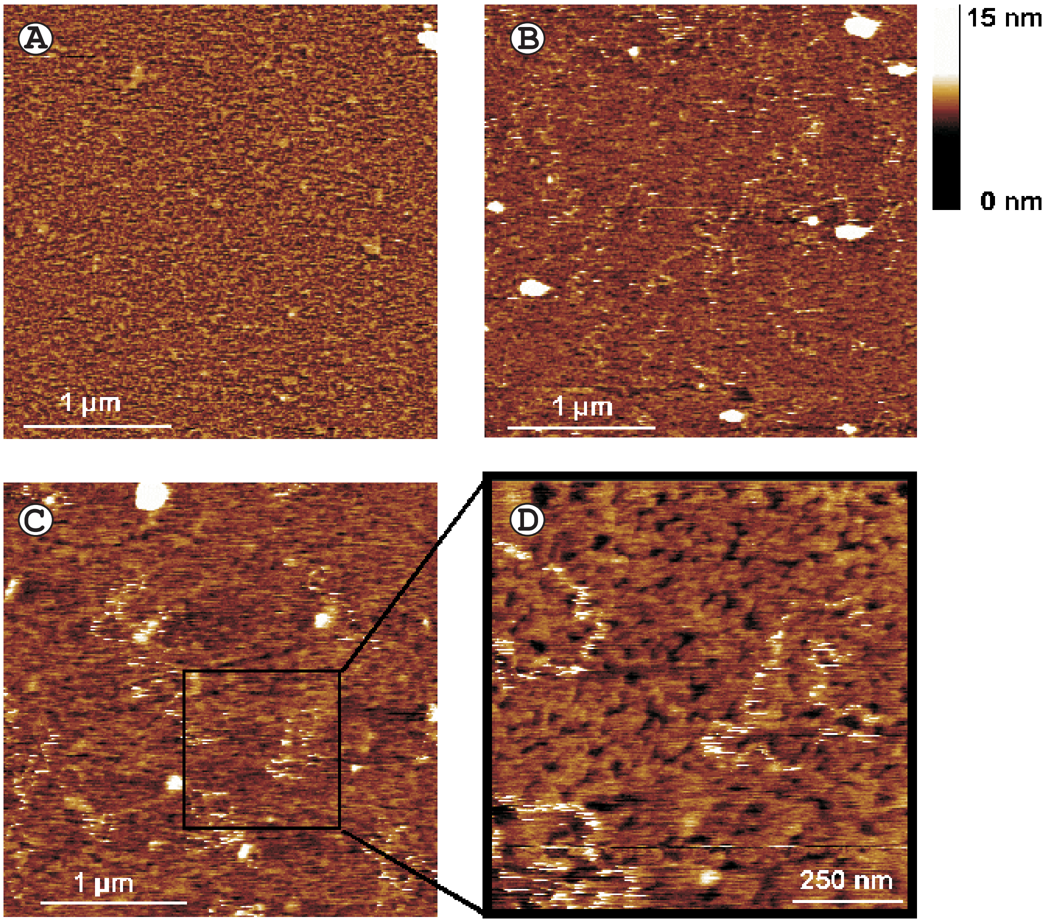

Figure 4.12: Fluid cell measurements of DNA on a PG2 layer. A) Adsorbed layer of PG2 on freshly cleaved mica. B) Deposition of linearized DNA onto the PG2 layer. C) Plasmid DNA on PG2 layer. D) Zoom of C).

because of the soft surface layer composed of the bulky, dendronized polymers. Therefore the tip does not feel a resting DNA molecule but vertically moving molecules.

4.3.1 Discussion on the Adsorption of DNA on a Flat Dendronized Polymer Layer

Using mica as a substrate, the negative surface charge can be bridged by a self-assembled cationic monolayers [39], or in the presence of divalent cations [140]. Thus, DNA molecules can be fixed to the substrate through electrostatic attraction for successful imaging with the SFM. In the present experiment it could be demonstrated that negatively charged DNA molecules can be immobilized on a layer composed of positively charged dendronized polymers for fluid cell SFM imaging. The DNA molecules must be fixed to the substrate through electrostatic attraction as it is already known in the above mentioned cases.

While the surface charge on mica, in the absence of counterions, is of two negative charges per nm^2 [140], under the present experimental conditions, the negative charge has been compensated by the positively charged dendronized polymers. On average, the positive amine groups on PG2 have a spacing of 0.25/4 nm and the phosphate groups on DNA have a spacing of 0.3 nm. Hence, the monolayer of PG2 should provide an excess of positive charges to immobilize DNA molecules strongly. This electrostatic binding can be verified in the experiment although the imaging quality was not satisfactory due to the roughness of the monolayer of the dendronized polymers.

4.4 Complex Formation of DNA Molecules and dendronized polymers - NaCl-free solution

Since the electrostatic attraction of DNA and dendronized polmyers has been demonstrated in the last section, their interaction in solution is further investigated in the following. Different parameters of the molecules themselves and the solution were changed in order to investigate the interaction process and the complex structure. For the analysis of DNA/dendronized polymer complexes experiments with generation 2 and 4 were carried out.

4.4.1 Complexes of Linear Plasmid DNA Molecules and Dendronized Polymers

When linear pUC19 DNA was mixed with dendronized polymers, different complexes were formed upon varying the DNA/dendronized polymer concentration and with it the charge ratio from $1/10, 1/5, 1/2.5$, and 1/1 through 1/0.1. The complexes are allowed to adsorb on mica or poly-L-ornithine coated mica surfaces as it will be mentioned.

DNA/dendronized polymer complexes with charge ratios of $1/10, 1/5$ and 1/2.5 adsorbed only onto freshly cleaved mica and not onto the positively charged, poly-L-ornithine coated mica substrates (Fig. 4.13). However, these adsorbates were too aggregated for further investigations via SFM.

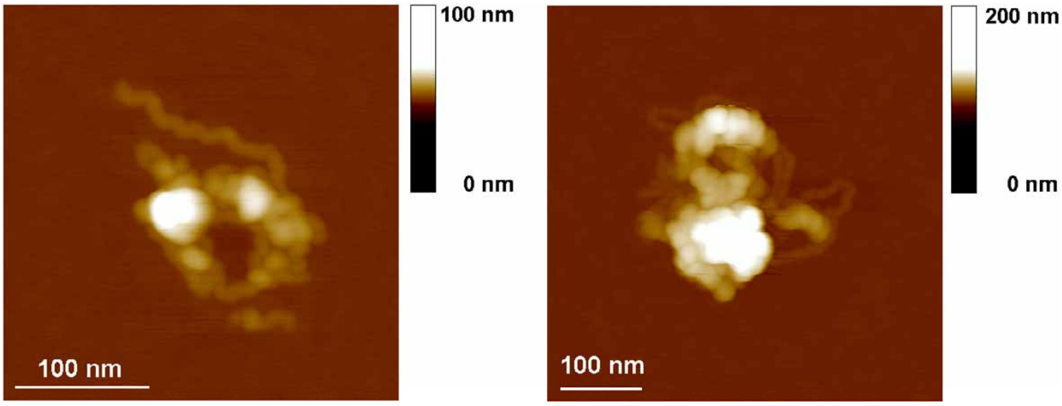

Figure 4.13: High resolution SFM images of bulky complexes on freshly cleaved mica. Charge ratio DNA/dendronized polymer 1/5.

In contrast, DNA/dendronized polymer complexes with charge ratios of 1/1 through 1/0.1 adsorbed only onto poly-L-ornithine coated mica substrates. Complexes with a charge ratio of 1/1 through 1/0.7 on poly-L-ornithine coated mica were the most suitable complexes for SFM analysis. Fig. 4.14 shows common types of complexes. For their analysis only those complexes were chosen which exhibited a constant height along their contour, and where the single DNA strands that came out of this complex belonged clearly to the complex (indicated by arrows in Fig. 4.14).

For contour length measurements, more highly resolved images of single complexes were used (Figs. 4.15a-f). There are different types of complexes. While for the complex in Figs. 4.15b,c,e and f clearly one DNA molecule is used, in Figs. 4.15a and d more than one DNA molecule must be involved, since the length of the DNA coming out of the complexes is longer than one DNA contour length. The contour of each complex was traced and analyzed as described in section 3.7.1.

For further analysis, also the average heights were measured, which amounted to (4.0 ± 0.3) nm for DNA/PG2, and (5.5 ± 0.6) nm for DNA/PG4. While the absolute height value depended on the generation of the dendronized polymer, the increase in height for all DNA/dendornized polymer complexes with respect to the bare dendronized polymers was the same, i.e. (2.4 ± 0.5) nm.

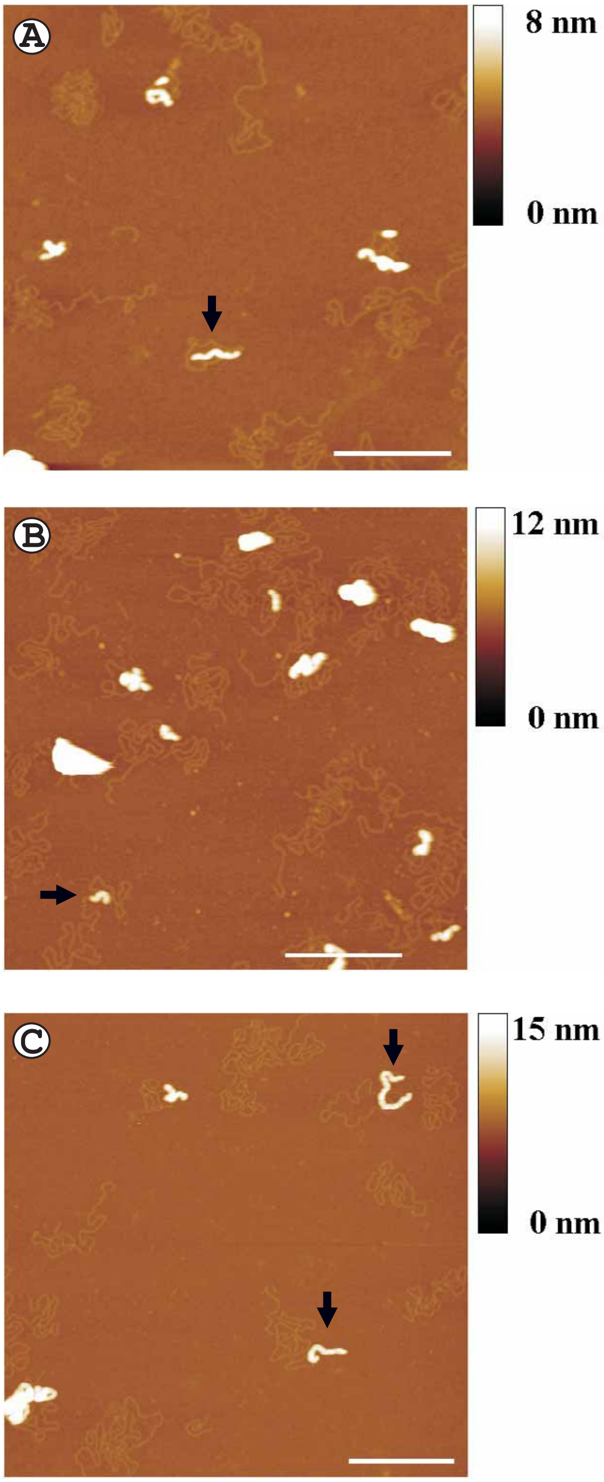

Figure 4.14: DNA/dendronized polymer complexes of charge ratio 1/0.7 precipitated onto poly-L-ornithine coated mica. (A) DNA/PG2, (B) DNA/PG3, and (C) DNA/PG4. The scale bare is 250 nm.

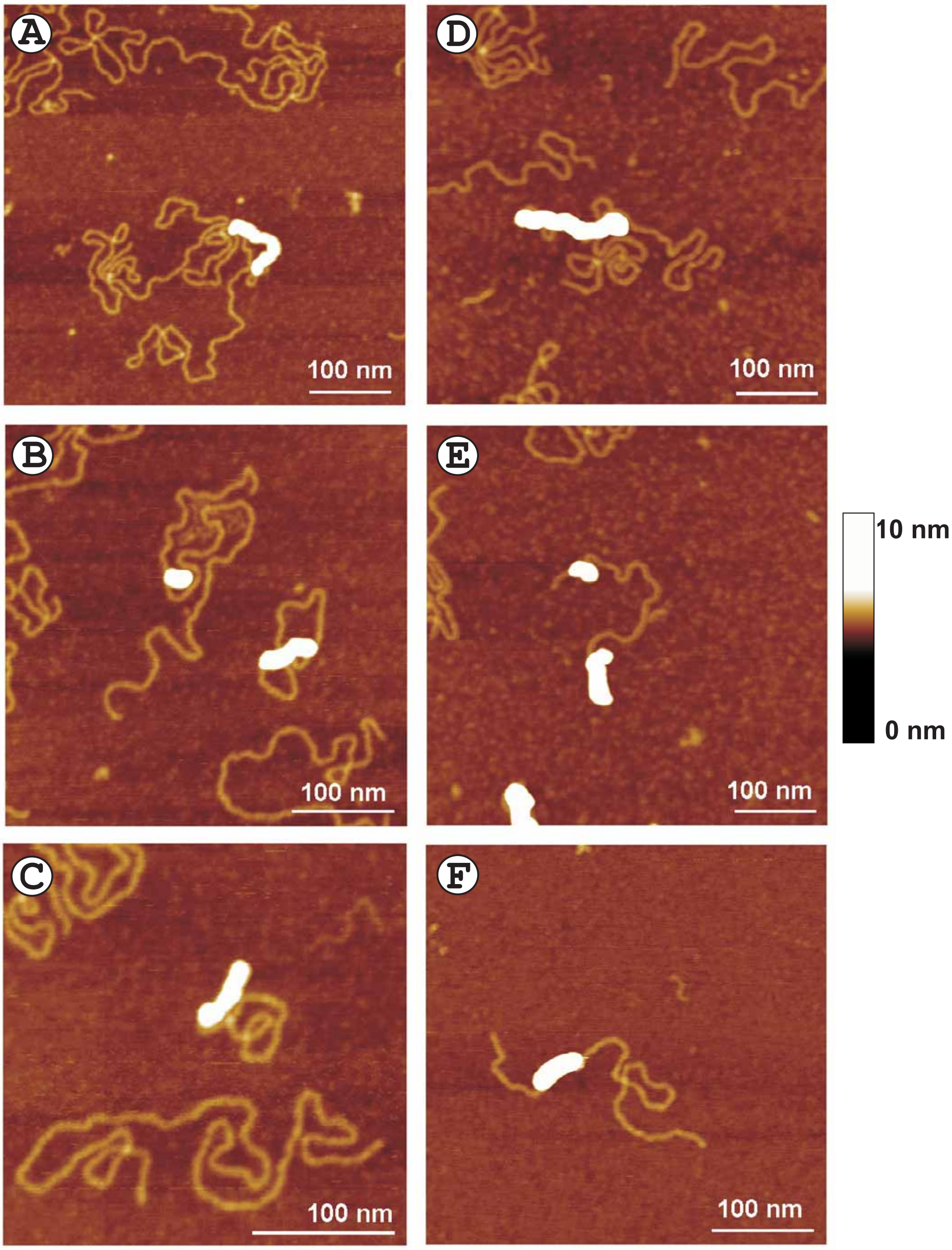

Figure 4.15: High resolution SFM images. Complexes of charge ratio 1/0.7 precipitated onto poly-L-ornithine coated mica. (A-C) DNA/PG2 (D-F) DNA/PG4 complexes.

4.4.2 Complexes of Circular Plasmid DNA Molecules and Dendronized Polymers

Complexes with a charge ratio of 1/1 through 1/0.5 using circular pUC19 DNA and PG4 exhibited the same structures compared to the DNA/PG4 complexes (Fig. 4.16) on poly-L-ornithine coated mica surface. The DNA molecules which came out of the complexes were relaxed as the uncomplexed circular plasmid DNA. The average height of circular DNA/PG4 complexes was (5.9 ± 0.3) nm.

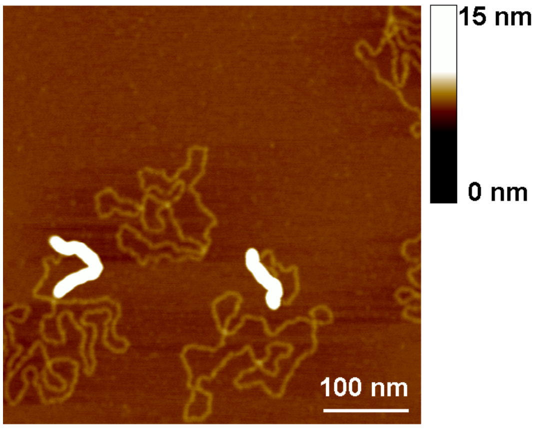

Figure 4.16: Complexes of circular pUC19 plasmid DNA and PG4.

4.4.3 Complexes of Short DNA Molecules and Dendronized Polymers

27 nm DNA is required for one turn around PG4 (for the calculated diameter of PG4 see Table 4.2). To distinguish the difference between a wrapped part and bare PG4, short DNA strands (213 bp $\approx$ 72 nm) have been used in order to wrap around the PG4 just for 3 times. The resulting complexes were allowed to adsorb on mica, to distinguish between parts of the bare PG4 and DNA wrapped PG4. Unfortunately, because of the tip broadening, it is not straight forward to deduce any additional information on the wrapping. Furthermore, the parts of wrapped DNA are also very often a link for other PG4s.

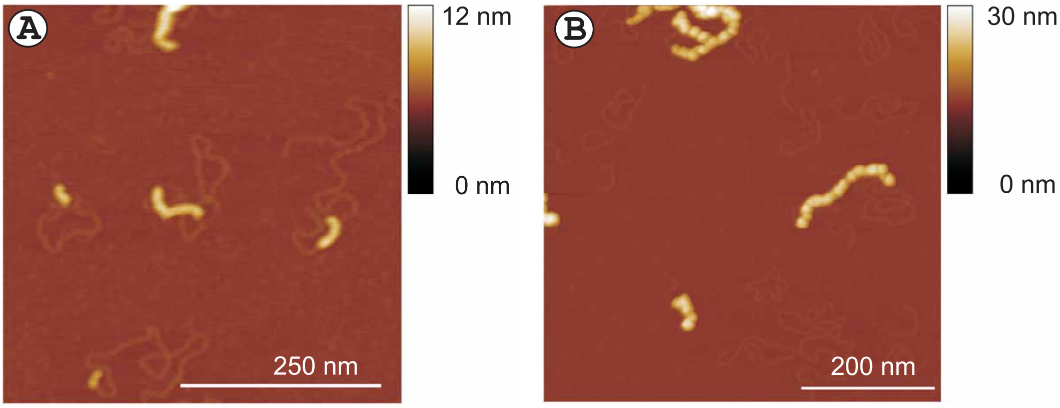

Figure 4.17: Complexes of partially protected dendronized polymers and linearized DNA. (A) Partially protected PG2 and (B) PG4 is used and adorbed on poly-L-ornithine coated mica. The height scale is chosen to demonstrate rather the blobb structure of the complex than the outcoming DNA.

4.4.4 Complexes of Linear Plasmid DNA Molecules and Partially Protected PG4 and PG2

Also the same structures of complexes formed with partially protected PG4% instead of PG4 or partially protected PG2% instead of PG2 and linear pUC19 DNA were observed on poly-L-ornithine coated mica surfaces for charge ratiso of 1/0.8 through 1/0.5 (Fig. 4.17). The average height of the complexes DNA/PG2% and DNA/PG4% was (4.0 ± 0.3) nm and (9.4 ± 1.3) nm, respectively.

4.4.5 Discussion on Complexes in Salt-free Solution

The comparison of the contour length distributions of the bare dendronized polymers and their complexes with DNA are shown in Fig. 4.18.

Fig. 4.18 shows that the Schulz-Flory distributions (section 2.6.1) of the data obtained for the DNA/PG2 and DNA/PG4 complexes compared to PG2 and PG4, respectively, and the corresponding statistical distribution averages (section 2.6.1) showed no differences within the errors (Table 4.4). From the similarity of the distributions of the bare polymers and the complexes it was concluded that the contour length of the complexes is defined by the bare dendronized polymers.

On the other hand, the length of the DNA that contributes to the complex

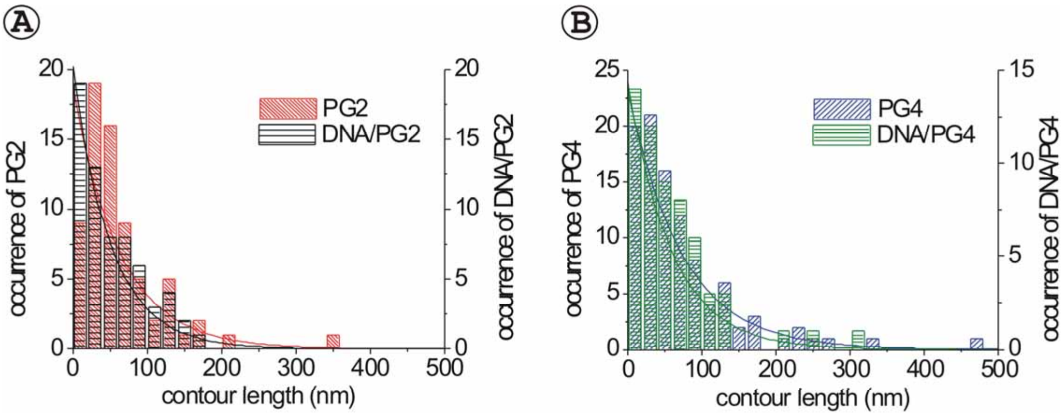

Figure 4.18: Contour length distributions of dendronized polymers. a) PG2 (red) and complexes formed from PG2 and DNA (black); b) PG4 (blue) and complexes formed from PG4 and DNA (green).

Table 4.4: Number average contour length, weight average contour length and length polydispersity of dendronized polymers and complexes.

System	$< \mathbf{L_n} >$ (nm)	$< \mathbf{L_w} >$ (nm)	**PD** $= \frac{<\mathbf{L_w}>}{<\mathbf{L_n}>}$
PG2	64 ±12	110 ±24	1.72 ±0.17
PG4	73 ±10	152 ±21	2.08 ±0.11
DNA/PG2	52 ±18	86 ±37	1.65 ±0.33
DNA/PG4	59 ±13	117 ±26	1.98 ±0.17

(L_{DNA-C}) can be obtained by subtracting the measured contour length of the DNA molecule that comes out of the complex (L_{out}) from the length of the monodisperse DNA (L_0): $L_{DNA-C} = L_0 - L_{out}$ (Fig. 4.19a). In Fig. 4.19b the contour lengths of the complexes (L_c) are plotted versus the DNA that contributes to the complex (L_{DNA-C}). The results can be grouped in three linear parts, which also contain negative values for L_{DNA-C}. We attribute these three parts to complexes formed with one, two and three monodisperse DNA (L_0) strands.

Figs. 4.15a, d show that there are complexes formed which might possess more than one DNA molecule of the length L_0. Therefore, plotting the contour length of the complexes (L_C) versus the DNA that contributes to the complex (L_{DNA-C}), and allowing doubles and triples of the monodisperse DNA (2×L_0 and 3×L_0) with the complex, the data exhibit an overall linear de-

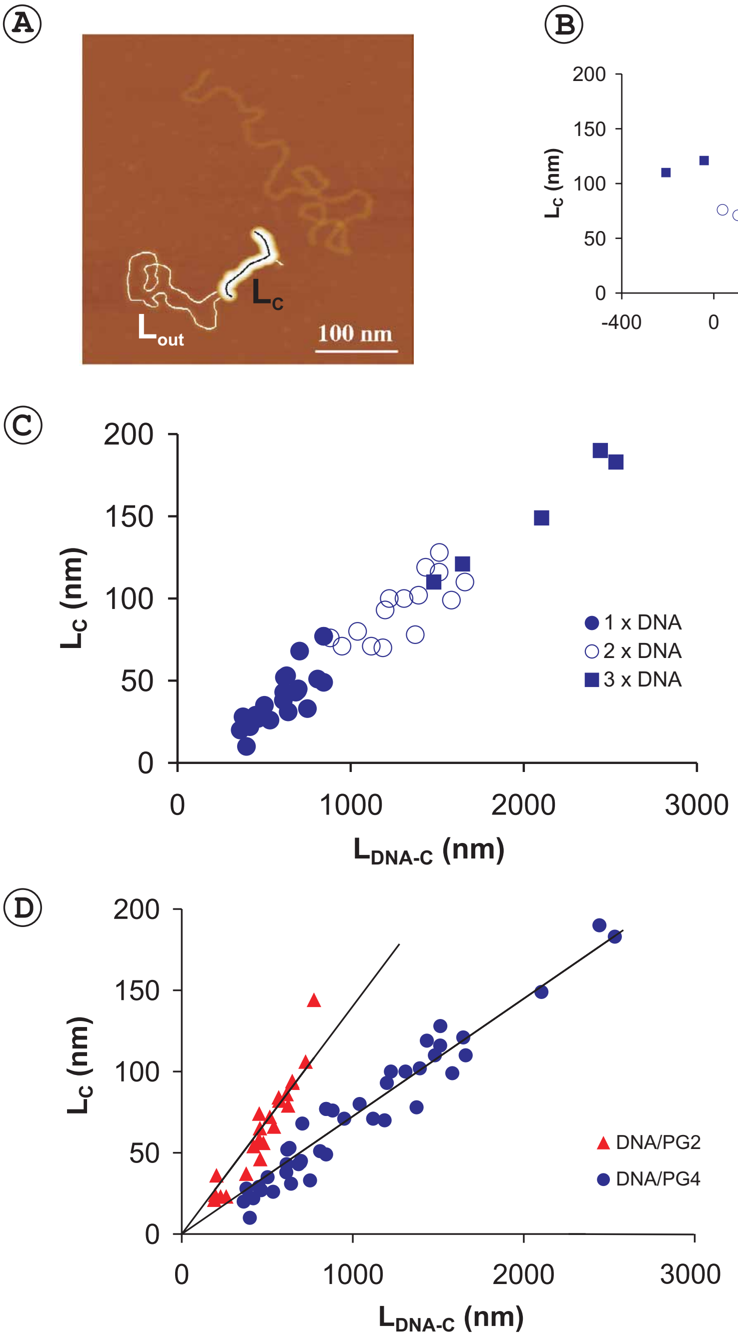

Figure 4.19: Linear dependence of the complex length (L_C) on the DNA length used for complexes (L_{DNA-C}). A) complex length (L_C) and contour length of the DNA molecule that comes out of the complex (L_{out}) are superimposed on the raw data. B) Contour length of the complex (L_C) versus length of DNA within the complex (L_{DNA-C}) for the DNA/PG4 complex. C) Data from B) allowing for more than one DNA molecule involved in a complex. Dendronized polymers complexing with 1 (•), 2 (○) and 3 (□) DNA molecules. D) Linear dependence of complex length (L_C) on DNA length used for complexes (L_{DNA-C}) for PG2 (△) and PG4 (•).

pendence (Fig. 4.19 c). The slope (m) varied depending on the generation of the dendronized polymer used (Fig. 4.19d): For DNA/PG2 complexes it is $m = 0.14 \pm 0.01$ and for DNA/PG4 complexes it is $m = 0.08 \pm 0.02$, using the statistical error.

Based on this linear dependence, as well as on the height measurements, and on the comparison of the contour length distributions of complexes and dendronized polymers, it is suggested that the DNA molecules wrap around the positively charged dendronized polymer (Fig. 4.20). However, also a configuration where DNA is aligned parallel to the underlying dendronized polmyer could be proposed. In this case, complexes should be seen, where many DNA strands exit at the ends of the complex because it is not as likely that the DNA makes a turn of 360° to fall backwards on the dendronized polymer again instead of coming off it. Consider Figs. 4.14 and 4.15 this was not observed. Therefore, it seems that the first model is the more reliable one.

For a quantitative model, one should take into account that SFM images underestimate the height of all the polymers, i.e. the dendronized polymers, the DNA molecules, and the complexes due to tip-sample interactions (deformation of the sample, section 2.5.6). Thus, using the calculated radii of dendronized polymers in section 3.3 according to their volume, and the theoretical diameter for DNA (r =2 nm), the DNA length required for one turn around the dendronized polymers (U), where $U = 2\pi(a_{PGi} + r/2)$ (i stands for the different generations) is (16.3 ± 1.0) nm for PG2 and (27.0 ± 2.1) nm for PG4. With $X_{PGi} = m_i U_i$, this results in a DNA pitch of $X_{PG2} = (2.30 \pm 0.27)$ nm for PG2 and $X_{PG4} = (2.16 \pm 0.27)$ nm for PG4 (Fig. 4.20), leaving some space for water layers. However, considering the special architecture and the swelling in solution of the dendronized polymers, an upper limit of the radius can be estimated to (3.2 ± 0.3) nm and (5.2 ± 0.5) nm for PG2 and PG4, respectively, as discussed in section 4.5.3. Thus, using the upper limits of radii, the pitch can be estimated to $X_{PG2} = (3.7 \pm 0.6)$ nm for PG2 and $X_{PG4} = (3.1 \pm 0.5)$ nm for PG4. However, to be on the save side, the lower limit of the radii were considered for the analysis in the case of zero salt concentration.

For comparison, also N. V. Hud and K. H. Downing [31] report on DNA toroids using cryo-TEM which show a minimum fringe spacing of 2.03 nm.

On the other hand, the high curvature of DNA around a diameter of (6.6 ± 0.7) nm of PG4 is practically identical to the average diameter (6.4 nm) formed by the superhelix of the nucleosome core particle [14]. The curvature for PG2 is even a little bit smaller.

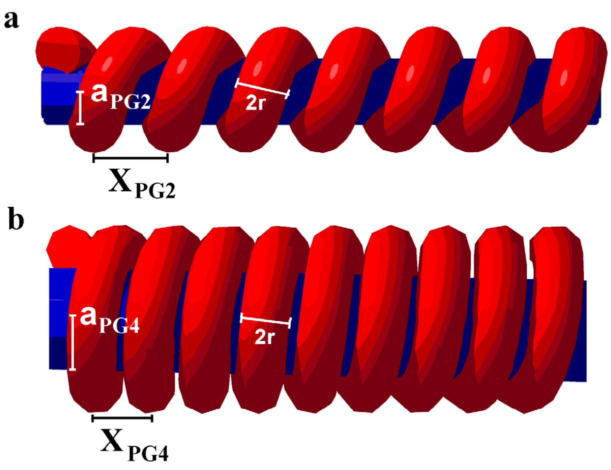

Figure 4.20: Model of the complex. DNA wraps around the dendronized polymer PG2 (a) and PG4 (b) resulting in pitches X_{PG2} and X_{PG4}. a_{PG2}, a_{PG4}, and r are the diameters of PG2, PG4, and DNA, respectively. Color code: blue cylinder stands for the dendronized polymer, red chain stands for the DNA.

In order to confirm the wrapping model, circular plasmid pUC19 DNA was used. If the DNA molecule wraps around the dendronized polymer, the DNA which is left over should preserve the coiling in opposite direction. This extra coiling of the free DNA molecule should be seen in the SFM. However, due to knicked DNA strands, the tension can be easily released like the supercoiling in section (2.1) and thus, again the DNA which came out of the complex is in an open circular state as seen in the SFM image (Fig. 4.16).

It has been shown in previous studies [43, 119] that the DNA spacing on charged lipid membranes increases when the surface charge density of the lipid membranes decreases. This increase in the pitch size can also be seen in our experiment upon decreasing the linear charge density of the dendronized polymer from PG4 to PG2 (described in section 3.3).

However, the overall charge of the complex depends also on the dendronized polymer generations involved in the complex formation. If we assume two negatively charged phosphates per 0.34 nm bp length, 4 positively charged amine groups on the PG2 and 16 on the PG4 per 0.25 nm repeat unit assuming the all-trans configuration (section 3.3), stoichiometrically, the DNA/PG4 complexes were nearly neutral (slightly overcharged), whereas the DNA/PG2 complexes were negatively overcharged. The fact that both complexes adsorbed only onto positively coated mica substrate is consistent with negatively charged complexes. While the radii and the linear charge densities of the two dendronized polymers are different, the charge ratio was kept constant near the isoelectric point (1/0.7 DNA/dendronized polymer). Evidence for the overcharging of charged macro-ions and surfaces by electrostatic interaction with oppositely charged macromolecules has been given experimentally [69, 70] and theoretically [71, 141, 142], and has been discussed in section 2.8.1.

Park et al. [72] and Kunze and Netz [73] provide theoretical approaches for spontaneous overcharging of a complex of a negatively charged semi-flexible chain wrapped around a positively charged rigid cylinder. The theories are discussed in section 2.8.2.

The theory of Park et al. [72] is a non-linear approach based on the Poisson-Boltzmann equation for macro-ions in aqueous monovalent salt solutions in the limit of low salt concentrations that is derived in section 2.8.2. It predicts an over- and undercharging of the complex depending on the flexibility (persistence length) of the chain given by Eq. (2.58). In the experiment the semi-flexible chain is identified with DNA and the rigid cylinder with the dendronized polymer. The flexibility of the chain (DNA) stays constant, while the radii and the linear charge densities of the cylinder (i.e. the dendronized polymer) are varied, which in the theory is associated with the elastic energy term and the electrostatic energy term of the system, respectively. Adhering to the theory of Park et al., the effective dimensionless charge density ξ_{eff} in the minimum energy state of the system can be calculated by minimizing the total free energy $\mathrm{F}_{tot,non}$ of the complex system in Eq. (2.57) with respect to ξ_{eff}. The theory predicts undercharging ($\xi_{eff} > 0$) only when the elastic energy term is larger than the electrostatic energy term and overcharging for the opposite case (see Eq. 2.58). For the case of the DNA/PG2 complex we can conclude that the contribution of the electrostatic energy is larger than the contribution of the elastic energy in the complex ($\xi_{eff} < 0$), while for the DNA/PG4 complex these two terms are about equal ($\xi_{eff} \approx 0$).

Condider following Gedankenexperiment: Assume a cylinder as long as needed to possess a charge equal to the charge of the length of the wrapped semiflexible chain. Thus, the complex is neutral. However, the gain in entropy due to the release of counterions can be used to wrap an additional length of the semi-flexible chain around the cylinder and therefore overcharging the complex in agreement with the theory. Furthermore, for doubling the linear charge density of the cylinder and maintaining its radius and length, the length of the wrapped semi-flexible chain is also doubled conserving the neutrality of the complex. However, the gain in entropy will also double and thus, the additional length of the wrapped semiflexible chain will also increase and will be responsible for the overcharging of the complex system. Consequentially, the pitch of the wrapped chain decreases because the length of the cylinder did not change.

In the experiments, PG4 possesses a four times higher linear charge density than PG2 (see section 3.3) while the molecular diameter only doubles. According to the theory of Park et al. [72], a more closely packed DNA is expected for the DNA/PG4 compared to the DNA/PG2 complex, in agreement with the experiments. Additional to the above discussed Gedankenexperiment, also the contribution of the elastic energy term in Eq. (2.58) has to be taken into account. In a DNA/PG2 complex, the bending of DNA is higher than in the DNA/PG4 complex. Therefore, regarding the charge of the complex according to Park's theory, the higher gain of entropy of the counterions as well as the decrease of bending energy for the DNA/PG4 complex compared to the DNA/PG2 complex, should lead to a more pronounced overcharging of the DNA/PG4 complex compared to DNA/PG2 complex. This cannot be seen in the experiments. Therefore, the model of Park et al. may not be reasonable in our case. Furthermore, considering the total free energy of the complex in the non-linear approach and neglecting the bending energy contribution (Eq. 2.59), the effective charge of the complex can be calculated using Eq. (2.61). Comparing the values to the experimental results, the predicted overcharging in this theory for the DNA/dendronizd polymer systems is much too small.

In fact, the theory of Park et al. [72] predicts a more closely packed complex for DNA/PG4 in agreement with the experiments. However, the effective charge of the complex (Eq. 2.58) depends on the balance between the bending and the electrostatic term. However, according to the experiments the resulting contributions of the DNA/PG2 compared to the DNA/PG4 complex behaved in the opposite direction. Furthermore, the direct calculations of the charge of the complexes differ in many orders of magnitude compared to the results derived from the experiments. Overall, the proposed model of Park et al. might be not reasonable for our experiments.

Another approach by Kunze and Netz [73] used a linear approximation to derive the total free energy of the system on the DH-level in Eq. (2.51) that neglects the contributions due to the release of counterions (section 2.7.2). The theory predicts a helical structure and an overcharging of the complex given by Eq. (2.53). The effective linear charge density of the resulting complex τ_{eff} depends only on the electrostatic attraction (Eq. 2.47) and electrostatic repulsion (Eq. 2.48) and neglects the contribution from the elastic energy term (in the limit of low salt, the electrostatic terms diverge) as well as the entropy of the counterions (DH-regime). Explicitly, if DNA is associated with the wrapped PE (linear charge density of $\tau_P = 5.9e^-/\mathrm{nm}$) and the dendronized polymer with the cylinder, the overcharging of the experiment can be directly compared to the theory in Eq. (2.53). Using Eq. (2.53) the effective charge of the complex is

$$\tau_{eff} = \frac{\tau_P}{2} = 2.9\frac{e^-}{\mathrm{nm}} \tag{4.1}$$

From the experimental data in Fig. 4.19d an overcharging of DNA/PG2 and DNA/PG4 can be estimated to $(21 \pm 4)e^-/\mathrm{nm}$ and $(0.4 \pm 7.2)e^-/\mathrm{nm}$, respectively. Comparing the theoretical and experimental effective charge density of the complexes, the DNA/PG2 complex is much more overcharged in the experiment than in theory, whereas in the case of DNA/PG4 the values are comparable. According to this theory the effective charges of the complexes depend only on electrostatic contributions, since the contributions of counterion condensation, as well as bending energy are neglected. Also Nguyen and Shklovskii [143] recently report on overcharging using a different approach on the basis of the mechanism called *fractionalization* derived by the use of a Wigner-crystal and confirm the effective charge of the complex by Eq. (4.1). However, the linear model (Eq. 2.51) is derived from the DH approximation that neglects many effects that cannot be neglected in the real experiment like inhomogeneous charge distribution, counterion release, van der Waals interactions, and Dipol interactions in aqueous solution [82]. Nevertheless, in its limits the theory can be used successfully as a prediction of the overcharging. However the discussed oversimplification may be the reason that the experimentally found overcharging of DNA/PG2 complexes is much more pronounced than predicted.

In summary, the two models explain the wrapping of the polyelectrolyte with the lower linear charge density (DNA) around the more highly charged cylinder (dendronized polymer). Furthermore, the theories discuss the overcharging of the resulting complexes. While in the linear approximation the overcharging is due to purely electrostatic effects, in the non-linear approach the overcharging depends on the balance between the bending versus entropic contributions and favored overcharging by the entropic term. However, the experimental results indicate that the overcharging of the complex is mainly driven by electrostatic forces whereas contributions of counterion entropy and bending energy seem to be negligible. Furhermore, also theories beyond the discussed mean-field approach propose overcharging of polyelectrolyte complexes. Here, the correlation-induced charge inversion on the basis of a Wigner-crytal is discussed [144].

Since the pitch of DNA could not be resolved by SFM (section 2.5.6), TEM studies were performed to verify the wrapping model in Fig. 4.20 directly. Several experiments using TEM have been carried out in order to detect the complexes. Although single dendronized polymers could be visualized (Fig 4.5), the complexes could not.

Another possibility to verify the wrapping model is changing the properties of the involved molecules in order to change the electrostatic interaction. The electrostatic interaction can be modified not only by varying the linear charge densities of the involved PE, but also by changing the ionic strength of the solution (section 2.8). While the last suggestion will be discussed in section 4.5, the first is discussed in the following.

According to other experiments [43], [119], and the Gedankenexperiment discussed above the pitch X of the DNA should change by varying the charge density of the dendronized polymer at a fixed radius. Regarding the opposite case, i.e. fixed linear charge density and varying radius of the dendronized polymer, the pitch X of the DNA should also be affected.

Experimentally, the charge of the dendronized polymer of one generation was reduced and the influence on the pitch X was measured. However, by reducing the linear charge of the dendronized polymers, resulting in PG2% and PG4% (see section 3.3.1), the backbone of the dendronized polymer seems to shrink and thus maintains the linear charge density (see Fig. 4.8). Therefore, the diameters of the 30 % protected dendronized polymer changed compared to the 0 % protected dendronized polymers as discussed in section 4.1.7. Thus, the pitch X of the DNA/PG% complex will not vary due to the different charge density but rather due to the increased diameter. Assuming the same rate of overcharging of the complexes, this should result in a decreasing slope in the graph of L_C versus L_{DNA-C} for DNA/PG4% compared to DNA/PG4 complexes. Fig. 4.21 shows this graph in comparison to the results of DNA/PG4. Overall, the slope of DNA/PG4% is decreased compared to DNA/PG4 complexes as expected and amounts to $m = (0.61 \pm 0.06)$ nm. However, by reducing the charges on the dendronized polymer too many parameters changed simultaneously for further quantitative investigation of the influence in complex formation.

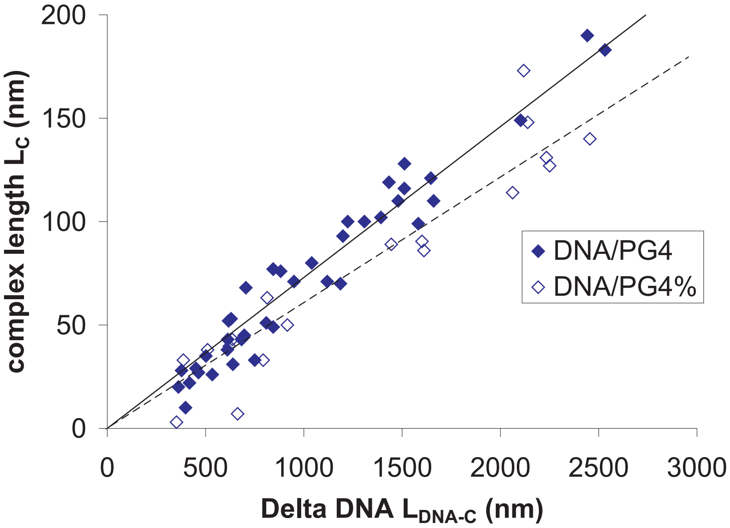

Figure 4.21: Linear dependence of the complex length (L_C) and DNA length used for complexes (L_{DNA-C}). A comparison between DNA/PG4 and DNA/PG4%.

4.5 Influence of NaCl on the Complex Formation of DNA and Dendronized Polymers

The salt concentration plays an important role in polyelectrolyte interaction (see section 2.7). Especially interactions of DNA and oppositely charged molecules in the presence of different salt concentrations play important roles in biological processes such as DNA transcription and replication (section 2.2.1). It has been shown that the process of unwinding of DNA from the histones can be controlled by different salt concentrations [28]. The salt concentration in the cell nucleus is as high as 100 mM NaCl [17].

In the present thesis, the influence of intermediate (10, 50, 100, 300, and 600 mM) (Fig. 4.22) and high (2.4 M) NaCl concentrations on the complexation of DNA and dendronized polymers were investigated. In the following experiments only PG2s were used. In contrast to the DNA/PG4 complex, the DNA pitch of the DNA/PG2 complex does no correspond to close packed wrapping, which is a pitch of 2 nm due to hard core repulsion of adjacent DNA strands.

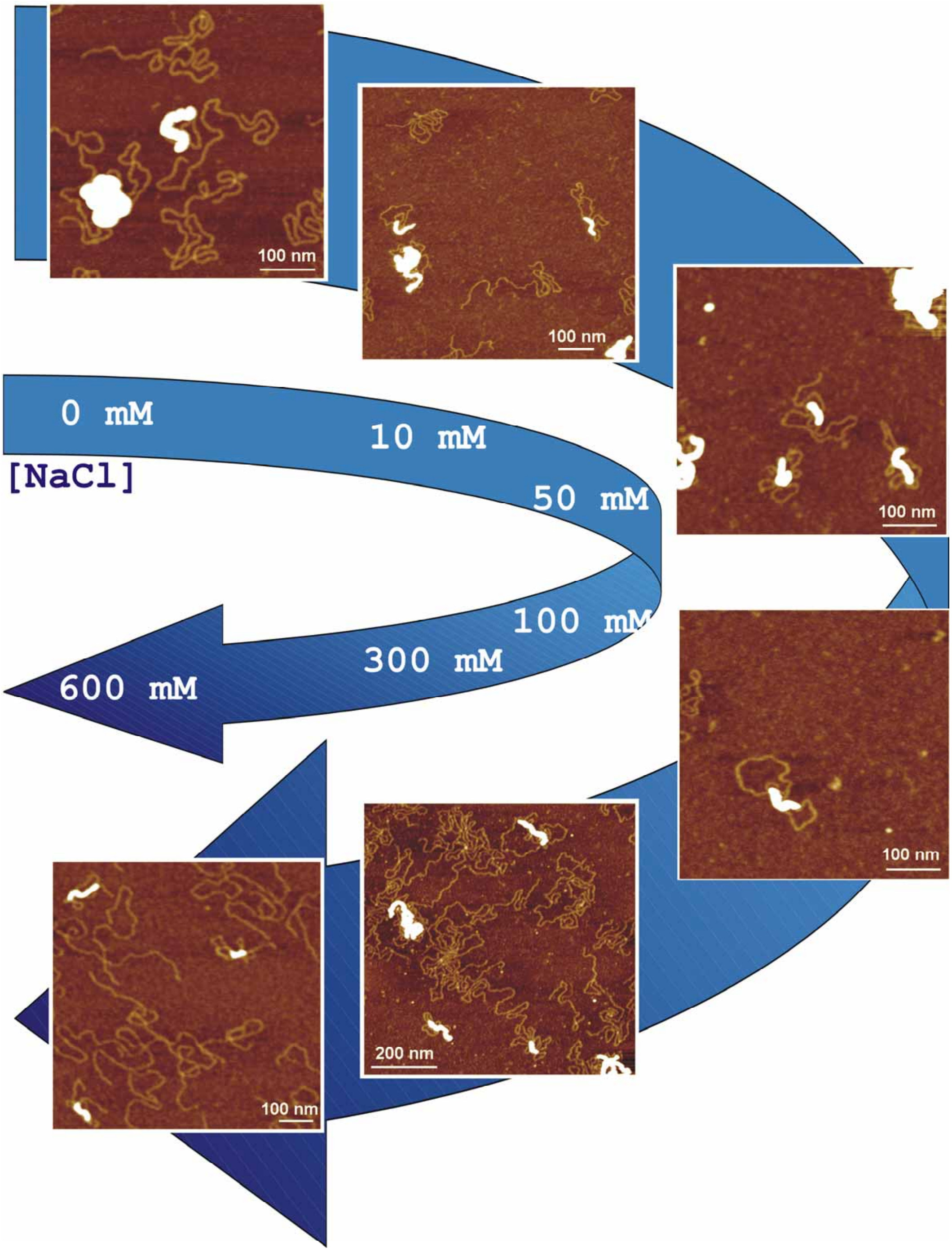

Figure 4.22: Influence of increasing salt concentration on complex formation. High resolution SFM images of complexes adsorbed on poly-L-ornithine coated mica. The height of all complexes was the same (4.0 ± 0.1) nm. The different scale bar is given in each SFM image.

4.5.1 Influence of Low NaCl Concentration on the DNA/PG2 Complex

The preparation of the complexes in 10, 50, 100, 300 and 600 mM NaCl solution is described in section 3.6.2. The visualized DNA/PG2 complexes from different NaCl solutions adsorbed only on poly-L-ornithine coated mica and showed the same structures as without added NaCl (Fig. 4.22). Again, the DNA pitch was also not resolved and the average height (4.0 ± 0.1) nm of the complexes did not change compared to the DNA/PG2 in the salt free solution.

4.5.2 Release of DNA from the DNA/PG2 Complex at High Salt Concentration

The release of DNA from the DNA/PG2 complex was observed 60 minutes after the dilution into an elevated NaCl concentration of 2.4 M. Single DNA strands, PG2s (grey arrows) as well as DNA/PG2 complexes (white arrows) on poly-L-ornithine coated mica substrates could be visualized in the presence of high salt concentration (Fig. 4.23).

4.5.3 Discussion on the Influence of NaCl on the Complex Formation of DNA Molecules and Dendronized Polymers

In order to reveal any differences in the complex formation of DNA and PG2 in the presence of elevated salt concentrations and with no salt, the images were analyzed as before. Plotting the contour length of the complexes L_C versus the DNA that contributes to the complex L_{DNA-C}, and allowing doubles and triples of the monodisperse DNA within the complex, the data again exhibit an overall linear dependence (Fig. 4.24a). The slope m varied depending on the NaCl concentration as summarized in Table 4.5.

The calculated radii of PG2 and PG4 in Eq. (3.1) assumed a polymer density of $\rho_g = 1g/cm^3$, which is a typical value for solid polymers. For a dendronized polymer one may expect cavities by its unique architecture (section 2.3.2). Also swelling of polyelectrolytes in solution is a well known feature [145]. Therefore, bearing the architecture and swelling in mind, an upper limit of the radius of PG2 can be given by approximating the dendronized polymer by a straight alcyl chain, depicted in Fig. 4.24b. The diameter is defined as $2a_{max} = 2 \times 12.5 \times b_E = 6.4$ nm, using $b_E = 0.2553$ nm [58]. Thus, according to section 4.4, the maximal circumference of PG2 amounts to $U_{max} = 26.4$ nm.

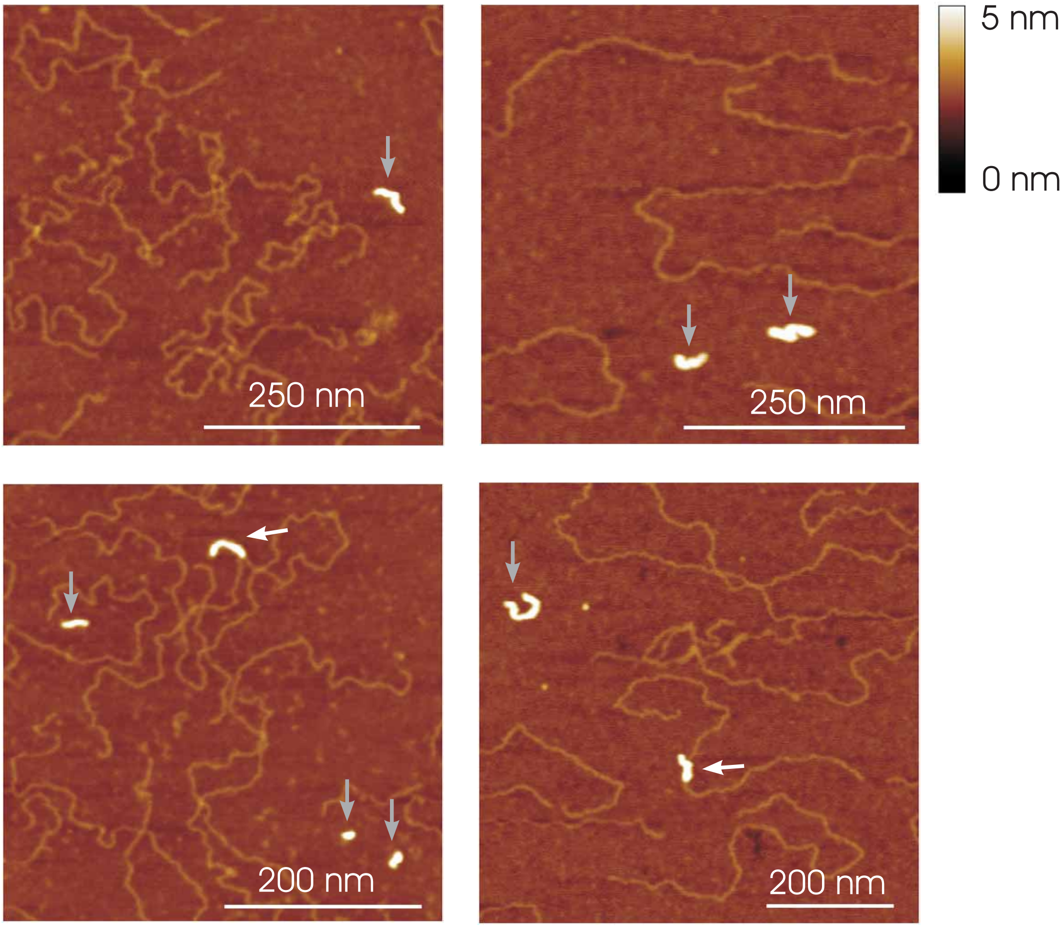

Figure 4.23: Release of DNA from the DNA/PG2 complex at high salt concentration. Adsorption of single PG2, single DNA molecules as well as complexes on poly-L-ornithine coated mica from 2.4 M NaCl solution. Grey arrows indicate single PG2s and white arrows indicate DNA/PG2 complexes. The scale is given within each image.

Using the slopes fom Fig. 4.24a, the maximal pitches X_{max} are calculated and summarized in Table 4.5 with respect to the NaCl concentration.

For increasing NaCl concentrations (10, 50, 100 mM) the amount of wrapped DNA on the PG2 increases. Thus, the slopes m and therefore the DNA pitches decreased compared to the prior case without added NaCl. The dotted line in Fig. 4.24a shows that for the same complex length of 100 nm the DNA that is needed for complexation increased from $L_{DNA-C} = 714$ nm in the salt free case to about the double length of $L_{DNA-C} = 1429$ nm in the case of 100 mM NaCl.

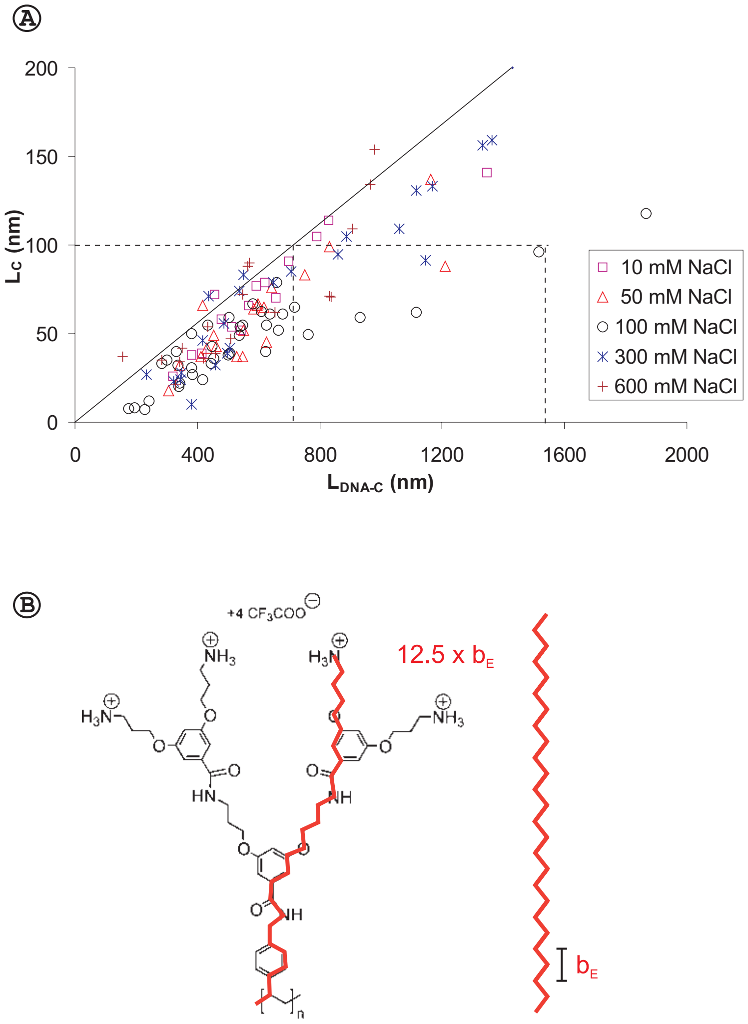

Figure 4.24: Complex formation of DNA and PG2 at elevated salt concentrations. A) Linear dependence of the complex length L$_C$ and DNA length used for complexes L$_{DNA-C}$. Slope m depends on the different salt concentrations. For comparison, the line shows the case of complexes in NaCl free solution from Fig. 4.19. B) Approximation of the radius of PG2 by a straight alcyl chain.

The increase of the amount of DNA per unit cylinder length for increasing salt concentration is in agreement with the linear theory of helical PE adsorption on a cylinder (section 2.8.2). Furthermore, in Fig. 2.22 (linear approach) the wrapping parameter η also doubles for an increase of 100 mM NaCl (corresponding to $\Delta\kappa a \simeq 1$). The enhanced overcharging of the complexes, i.e. decreasing slope, by adding NaCl can also be seen from Fig. 4.24a and is pre-

Table 4.5: Slope m and corresponding pitch X_{max}. The pitch X_{max} is calculated using the slopes in Fig. 4.24a. A direct comparison with the Debye screening length κ^{-1} is given.

[NaCl] mM	κ^{-1} **nm**	**slope** m	$\mathbf{X_{max}}$ **nm**
0		0.14 ±0.01	3.7 ±0.3
10	3.08	0.12 ±0.01	3.2 ±0.2
50	1.38	0.10 ±0.01	2.6 ±0.2
100	0.97	0.07 ±0.01	1.8 ±0.1
300	0.56	0.11 ±0.01	2.9 ±0.2
600	0.40	0.13 ±0.01	3.4 ±0.2

dicted within the theory.

However, for even higher salt concentrations (300 and 600 mM) the slope increases again (Table 4.5). If the radius of PG2 becomes larger than the Debye screening length, i.e. $a > \kappa^{-1}$, the adsorption can be simplified to an adsorption onto an oppositely charged planar surface again [122], such that the balance between electrostatic attraction and entropic repulsion determines the pitch as described in section 2.8.1. The electrostatic attraction gets screened and therefore the pitch increases again due to entropic repulsion (Eq. 2.34).

Overall, the DNA pitch decreased for 10 and 50 mM NaCl, reached its minimum at 100 mM NaCl, and increased again for 300 and 600 mM NaCl. If the pitch is plotted with respect to the salt concentration c_0 ($c_0 \sim \kappa$) (Fig. 4.25), the graph possessed a minimum as it is predicted in the theory of adsorption onto a planar surface in section 2.8.1, Fig. 2.20, due to the electrostatic (Eq. 2.36) and entropic Odijk (Eq. 2.34) repulsion. According to the theory (see section 2.8.1), in the case of 10, 50, and 100 mM NaCl the DNA-DNA distance (i.e. pitch) is determined by the balance between the electrostatic attraction and repulsion and decreases for increasing salt concentration, whereas in the case of 300 and 600 mM NaCl the balance between the electrostatic attraction and the entropic repulsion determines the mean DNA-DNA distance and increases for increasing salt concentration. Experimentally the onset between the two regimes occurred at 100 mM NaCl. The minimum is theoretically predicted by the balance of $b_e = b_{ent}$ and can be estimated to (110 ± 20)mM salt in Fig. 4.25. Previous experiments on DNA adsorption onto a charged lipid membrane report solely on an increase of DNA-DNA distance due to increasing salt concentrations [120]. However, in contrast to the DNA/PG2

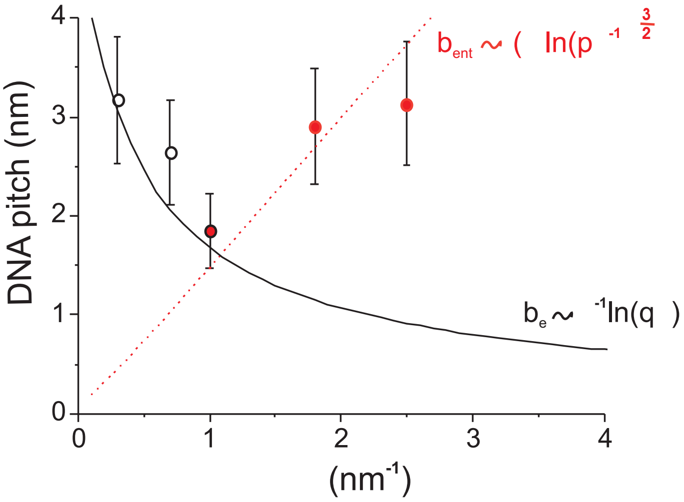

Figure 4.25: Pitch of DNA versus the salt concentration ($\sim \kappa$). The experimental data is fitted to the Eq. (2.34) and Eq. (2.36), including the constants q and p adapted to the DNA/PG2 system.

system, the surface charge of the lipid membrane was 19 orders of magnitude smaller. Therefore, the contribution of the electrostatics to the DNA-DNA distance became negligible [123] and the DNA lamellae were stabilized solely through the Odijk repulsion (Eq. 2.34).

In the case of higher salt concentrations, the desorption of DNA from the PG2 took place. From the complex solution, besides single DNA molecules and DNA/PG2 complexes, also single PG2s adsorbed on the poly-L-ornithine coated mica surface (Fig. 4.23). The adsorption of PG2s on poly-L-ornithine coated mica surfaces in the presence of high salt was already shown in section 4.1.5. Using Eq. (2.38) the salt concentration threshold, expressed in κ, for the desorption process can be calculated and becomes for the DNA/PG2 system approximately 2.6 nm^{-1}. Experimentally, κ amounts to ≈ 5 nm^{-1}, which is within the same order of magnitude. Furthermore, the release of DNA compared to other experiments, that investigate structural changes of nucleosome core particles [25], [24], is in good agreement. Yanger et al. [28] report on a DNA release from the nucleosome in a high NaCl solution (> 0.75 M) in an all or none unwrapping transition. In comparison to the DNA/dendronized polymer system, the surface charge density of PG2 is much higher than of the histone octamer. Thus, the onset of desorption of DNA from the PG2 has to be at higher salt concentrations as it can be seen in the experiment.

In summary, within the theory of PE interaction the influence of salt on the DNA/PG2 complex system could be studied. The dendronized polymers together with the DNA are a useful model system to test theories on the interaction of oppositely charged PE. It has been shown that an appropriate NaCl concentration can be used to change the DNA pitch substantially in agreement with the theory. For even higher salt concentrations the DNA/PG2 complex can fall apart into its components again.

Chapter 5

Conclusion and Perspective

DNA and dendronized polymers are well defined polyelectrolytes with the ability to form complexes with each other due to electrostatic interaction. Using the scanning force microscope as an imaging tool, single dendronized polymers, DNA molecules, and their complexes were investigated. High resolution images of single polyelectrolytes as well as the complexes were used to deduce their molecular structures. On the one hand, the scanning force microscope could be used successfully to determine the molecular length distribution of the dendronized polymers [56]. On the other hand, from the images a well defined molecular level structural model for the DNA/dendronized polymer complex could be derived. A helical morphology is proposed according to which the polyelectrolyte with the smaller linear charge density (DNA) is wrapped around the more highly charged dendronized polymer [146]. For different generations of dendronized polymers the pitch of the DNA varied. Overall the complex is negatively overcharged.

The work allowed for the first time, to elucidate the structure of single complexes of oppositely charged polyelectrolytes. The dendronized polymers together with DNA can provide a useful model system to help to understand the wrapping mechanism in the nucleosome, where DNA wraps around the histone proteins as well as in non-viral gene delivery systems. Furthermore, the complexes can be used to test theories on the interaction of oppositely charged polyelectrolytes. The experimental results were discussed with two theoretical approaches, both describing complexes in which the polyelectrolyte wraps around the other using the non-linear Poisson-Boltzmann equation [72] or the linear Debye-Hückel approximation [73]. Although both theories predict overcharging of the complexes, a better agreement with the experimental results is given within the latter approach. Therefore it can be concluded that the driving forces for the overcharging of the complexes are mainly electrostatic, whereas entropic and elastic energy contributions may be negligible.

The influence of the linear charge density of the dendronized polymers and of the ionic strength in aqueous solutions on the complex formation was also studied. The prediction of polyelectrolyte adsorption within the classical Debye Hückel theory [122] could be verified, particularly the observed minimum of the DNA pitch for increasing NaCl concentration [147]. For even higher NaCl concentration the DNA releases from the dendronized polymer in agreement with other experiments as well as the theory.

Both experimentally and theoretically, the research on the DNA/dendronized polymer complexes is indeed encouraging and opens the way to further experiments on this basis:

- Using higher generation dendronized polymers, the number of charged endgroups will increase as $\sim 2^{G+1}$. While the maximal wrapping density is already given in the DNA/PG4 complex, for higher dendronized polymers the charge of the complex can become even undercharged.
- Stiffness, radius and linear charge density of DNA could be varied by using G-quartett DNA.
- Layer-by-layer deposition of oppositely charged PEs can be used to change the charge of the complex [148]. Here, the negative charge of the DNA/dendronized polymer complex can be changed by adsorbing a positively charged PE. Furthermore, multilayer deposition on the complex can be investigated.
- These complexes are interesting model systems for transfection experiments. As mentioned above, in contrast to other non-viral gene delivery systems, the DNA/dendronized polymer complex exhibits a well defined structure.

Bibliography

[1] V. A. Bloomfield. DNA condensation. *Curr. Opinion Struc. Biol.*, 6:334, 1996.

[2] K. Keren, Y. Soen, G. B. Yoseph, R. Gilad, E. Braun, U. Sivan, and Y. Talmon. Microscopies of complexation between long DNA molecules and positively charged colloids. *Phys. Rev. Lett.*, 89:088103, 2002.

[3] E. Pfefferkorn. The role of polyelectrolytes in the stabilisation and destabilisation of colloids. *Adv. Colloid Interface Sci.*, 56:33, 1995.

[4] A. U. Bielinska, C. Chen, J. Johnson, and J. R. Baker Jr. DNA complexing with polyamidoamine dendrimers: Implication for transfection. *Bioconjugate Chem.*, 10:843, 1999.

[5] L. Shu, A. D. Schlüter, C. Ecker, N. Severin, and J. P. Rabe. Extremely long dendronized polymers: Synthesis, quantification of structure perfection, individualization, and SFM manipulation. *Angew. Chem., Int. Ed.*, 40:4666, 2001.

[6] A. Schaper and T. M. Jovin. Striving for atomic resolution in biomolecular topography: the scanning force microscope SFM. *Bioessays*, 18:925, 1996.

[7] M. Gerle, K. Fischer, S. Roos, A. H. E. Müller, M. Schmidt, S. S. Sheiko, S. Prokhorova, and M. Möller. Main chain conformation and anomalous elution behavior of cylindrical brushes as revealed by GPC/MALLS, light scanntering, and SFM. *Macromolecules*, 32:2629, 1999.

[8] A. L. Lehninger, D. L. Nelson, and M. M. Cox. *Principles of biochemistry.* Worth Publishers, New York, second edition, 1993.

[9] H. Lodish, A. Berk, S. L. Zipursky, P. Matsudaira, D. Baltimore, and J. Darnell. *Molecular Cell Biology.* W. H. Freeman and Company, New York, fourth edition, 2000.

[10] L. Stryer. *Biochemistry.* W. H. Freeman and Company, New York, fourth edition, 1995.

[11] A. Pingoud and A. Jeltsch. Structure and function of type II restriction endonucleases. *Nucl. Acid Res.*, 29:3705, 2001.

[12] A. Meisel, P. Mackeldanz, T. A. Bickle, D. H. Krüger, and C. Schroeder. Type III restriction endonucleases translocate DNA in a reaction driven by recognition site-specific ATP hydrolysis. *EMBO*, 14:2958, 1995.

[13] P. Janscak, U. Sandmeier, M. D. Szczelkun, and T. A. Bickle. Subunit assembly and mode of DNA cleavage of the type III restriction endonucleases EcoP1I and EcoP15I. *J. Mol. Biol.*, 306:417, 2001.

[14] K. Luger, A. W. Mäder, R. K. Richmond, D. F. Sargent, and T. J. Richmond. Crystal structure of the nucleosome core particle at 2.8 Angström resolution. *Nature*, 389:251, 1997.

[15] J. Widom. Chromatin: The nuclesome unwrapped. *Current Biology*, 7:R653, 1997.

[16] W. M. Gelbart, R. F. Bruinsma, P. A. Pincus, and V. A. Parsegian. DNA-inspired electrostatics. *Phys. Today*, 53:38, 2000.

[17] W. Saenger. *Principles of nucleic acid structure.* Springer-Verlag, New York, 1984.

[18] J. Widom. Toward a unified model of chromatin folding. *Annu. Rev. Biophys. Biophys. Chem.*, 18:365, 1989.

[19] J. Bednar, R. A. Horowitz, S. A. Grigoryev, L.M. Carruthers, J. C. Hansen, A. J. Koster, and C. L. Woodcock. Nucleosomes, linker DNA, and linker histone form a unique structural motif that directs the higher-order folding and compaction of chromatin. *Proc. Natl. Acad. Sci. USA*, 95:14173, 1998.

[20] H. Schiessel, W. M. Gelbart, and R. Bruinsma. DNA folding: Structural and mechanical properties ot the two-angle model for chromatin. *Biophys. J.*, 80:1940, 2001.

[21] J. Zlatanova, S. H. Leuba, and K. van Holde. Chromatin fiber structure: Morphology, molecular determinants, structural transitions. *Biophys. J.*, 74:2554, 1998.

[22] T. T. Nguyen and B. I. Shklovskii. Complexation of DNA with positive spheres: Phase diagram of charge inversion and reentrant condensation. *J. Chem. Phys.*, 115:7298, 2001.

[23] G. Felsenfest. Chromatin unfolds. *Cell*, 86:13, 1996.

[24] S. Mangenot, A. Leforestier, P. Vachette, D. Durand, and F. Livolant. Salt-induced conformation and interaction changes of nucleosome core particle. *Biophys. J.*, 82:345, 2002.

[25] E. Ballestar, M. Boix-Chornet, and L. Franco. Conformational changes in the nucleosome followed by the selective accessibility of histone glutamines in the transglutaminase reaction: Effects of ionic strength. *Biochemistry*, 40:1922, 2001.

[26] K. J. Polach and J. Widom. Mechanism of protein access to specific DNA sequences in chromatin: A dynamic equilibrium model for gene regulation. *J. Mol. Biol.*, 254:130, 1995.

[27] K.-K. Kunze and R. R. Netz. Salt-induced DNA-histone complexation. *Phys. Rev. Lett.*, 85:4389, 2000.

[28] T. D. Yager, C. T. McMurray, and K. E. van Holde. Salt-induced release of DNA from nucleosome core particle. *Biochemistry*, 28:2271, 1989.

[29] S. N. Khrapunov, A. I. Dragan, A. V. Sivolob, and A. M. Zagaiya. Mechanisms of stabilizing nucleosome structure. Study of dissociation of histone octamer from DNA. *Biochim. Biophys. Acta*, 1351:213, 1997.

[30] N. L. Marky and G. S. Manning. A theory of DNA dissociation from the nucleosome. *J. Mol. Biol.*, 254:50, 1995.

[31] N. V. Hud, K. H. Downing, and R. Balhorn. A constant radius of curvature model for the organization of DNA in toriodal condensates. *Proc. Natl. Acad. Sci. U.S.A.*, 92:3581, 1995.

[32] R. Golan, L. I. Pietrasanta, W. Hsieh, and H.G. Hansma. DNA toroids: Stages in condensation. *Biochemistry*, 38:14069, 1999.

[33] C. Böttcher, C. Endisch, J. H. Fuhrhop, C. Catterall, and M. Eaton. High-yield preparation of oligomeric C.type DNA toroids and their characterization by cryoelectron microscopy. *J. Am. Chem. Soc.*, 120:12, 1998.

[34] M. J. Allen, E. M. Bradbury, and R. Balhorn. AFM analysis of DNA-protamine complexes bound to mica. *Nucleic Acid Res.*, 24:2221, 1997.

[35] M. Laus, K. Sparnacci, B. Ensoli, S. Butto, A. Caputo, I. Mantovani, G. Zuccheri, B. Samori, and L. Tondelli. Complex associates of plasmid DNA and a novel class of block copolymers with PEG and cationic segments as new vectors for gene delivery. *J. Biomater. Sci. Polymer Edn.*, 12:1, 2001.

[36] T. K. Bronich, H. K. Nguyen, A. Eisenberg, and A. V. Kabanov. Recognition of DNA topology in reactions between plasmid DNA and cationic copolymers. *J. Am. Chem. Soc.*, 122:8339, 2000.

[37] J. S. Choi, E. J. Lee, Y. H. Choi, Y. L. Jeong, and J. S. Park. Poly(ethylene glycol)-block-poly(l-lysine) dendrimer: Novel linear polymer/dendrimer block copolymer forming a spherical water-soluble polyionic complex with DNA. *Bioconjugate Chem*, 10:62, 1999.

[38] M. A. Wolfert, E. H. Schacht, V. Toncheca, K. Ulbrich, O. Nazarova, and L. W. Seymour. Characterization of vectors for gene therapy formed by self-assembly of DNA with synthetic block co-polymers. *Human Gene Therapy*, 7:2123, 1996.

[39] D. D. Dunlap, A. Maggi, M. R. Soria, and L. Monaco. Nanoscopic structure of DNA condensed for gene delivery. *Nucleic Acids Res.*, 25:3095, 1997.

[40] W. Chen, N. J. Turro, and D. A. Tomalia. Using ethidium bromide to probe the interactions between DNA and dendrimers. *Langmuir*, 16:15, 1999.

[41] V. A. Kabanov, V. G. Sergeyev, O. A. Pyshkina, A. A. Zinchenko, A. B. Zezin, J. G. H. Joosten, J. Brackman, and K. Yoshikawa. Interpolyelectrolyte complexes formed by DNA and astramol poly(propylene imine) dendrimers. *Macromolecules*, 33:9587, 2000.

[42] M. F. Ottaviani, F. Furini, A. Casini, N. J. Turro, S. Jockusch, D. A. Tomalia, and L. Messori. Formation of supramolecular structures between DNA and starburst dendrimers studies by EPR, CD, UV, and melting profiles. *Macromolecules*, 33:7842, 2000.

[43] J. O. Rädler, I. Koltover, T. Salditt, and C. R. Safinya. Structure of DNA-cationic liposome complexes: DNA intercalation in multilamellar membranes in distinct interhelical packing regimes. *Science*, 275:810, 1997.

[44] T. E. Creighton. *Encyclopedia of molecular biology*, volume 4. John Wiley and Sons, Inc., New York, 1997.

[45] A. G. Schatzlein. Non-viral vectors in cancer gene therapy: Principles and progress. *Anticancer Drugs*, 12:275, 2001.

[46] D. A. Tomalia, A. M. Naylor, and W. A. Goddard III. Starburst dendrimers: Molecular-level control of size, shape, surface chemistry, topology, and flexibility from atoms to macroscopic matter. *Angew. Chem., Int. Ed. Engl.*, 29:138, 1990.

[47] J. Haensler and F. C. Szoka Jr. Polyamidoamine cascade polymers mediate efficient transfection of cells in culture. *Bioconjugate Chem.*, 4:372, 1993.

[48] L. Qin, D. R. Pahud, A. U. Bielinska, J. F. Kukowska-Latallo, J. R. Baker Jr., and J. S. Bromberg. Efficient transfer of genes into murine cardiac grafts by starburst polyamidoamine dendrimers. *Humane Gene Therapy*, 9:553, 1998.

[49] A. U. Bielinska, J. F. Kukowska-Latallo, and J. R. Baker Jr. The interaction of plasmid DNA with polyamidoamine dendrimers: Mechanism of complex formation and analysis of alerations induced in nuclease sensitivity and transcriptional activity of the complexed DNA. *Biochim. Biophys. Acta*, 1353:180, 1997.

[50] J.-P. Behr. Gene transfer with synthetic cationic amphiphiles: Prospects for gene therapy. *Bioconjugate Chem.*, 5:382, 1994.

[51] E. Dauty, J. S. Remy, T. Blessing, and J. P. Behr. Dimerizable cationic detergents with a low cmc condense plasmid DNA into nanometric particles and transfect cells in culture. *J. Am. Chem. Soc.*, 123:9227, 2001.

[52] Y. Jiao, D. I. Cherny, G. Heim, T. M. Jovin, and T. E. Schäffer. Dynamic interactions of p53 with DNA in solution by time-lapse atomic force microscopy. *J. Mol. Biol.*, 2:233, 2001.

[53] S. Reich. in preparation. 2002.

[54] M. Freemantle. Blossoming of dendrimers. *Science/Technology*, 77:27, 1999.

[55] M. Wind, U.-M. Wiesler, K. Saalwächter, K. Müllen, and H. W. Spiess. Shape-persistent polyphenylene dendrimers - restricted milecular dynamics from advanced solid-state nuclear magnetic resonance techniques. *Adv. Mater.*, 13:752, 2001.

[56] L. Shu, I. Gössl, J. P. Rabe, and A. D. Schlüter. Quantitative aspects of the dendrozation of dendronized linear polystyrenes. *Macromol. Chem. Phys.*, 203:2540, 2002.

[57] R. Esfand and D.A. Tomalia. Poly(amidoamine) (pamam) dendrimers: From biomimicry to drug delivery and biomedical applications. *Drug Discov. Today*, 6:427, 2001.

[58] H.-G. Elias. *An introduction to polymer science.* VHC, Weinheim, 1997.

[59] D. A. Tomalia. Dendrimers: Nanoscopic modules for the construction of higher ordered complexity. *Modular Chem.*, page 183, 1997.

[60] P. G. de Gennes and H. Hervet. Statistics of starburst polymers. *J. Phys. (Paris)*, 44:L351, 1983.

[61] D. Boris and M. Rubinstein. A self-consistent mean field model of a starburst dendrimer: Dense core vs dense shell. *Macromolecules*, 29:7251, 1996.

[62] D. Pötschke, M. Ballhauff, P. Lindner, M. Fischer, and F. Vögtle. The structure of dendritic molecules in solution as investigated by small-angle neutron scattering. *Macromol. Chem. Phys.*, 201:330, 2000.

[63] A .D. Schlüter and J. P. Rabe. Dendronized polymers: Synthesis, characterization, assembly at interfaces, and manipulation. *Angew. Chem., Int. Ed.*, 39:864, 2000.

[64] L. Shu, A. Schäfer, and A. D. Schlüter. Dendronized polymers: Increasing of dendron generation by the attach-to approach. *Macromolecules*, 33:4321, 2000.

[65] Accelrys Inc. Materials studio^{TM}. *Version 2.1*, 2001.

[66] J. Barner, F. Mallwitz, L. Shu, A. D. Schlüter, and J. P. Rabe. Covalent connection of two individual polymer chains on a surface: An elementary step towards molecular nanoconstructions. *Angew. Chem., Int. Ed.*, in press, 2003.

[67] F. M. Menger and J. S. Keiper. Gemini surfactants. *Angew. Chem. Int. Ed.*, 39:1906, 2000.

[68] H.-J. Quadbeck-Seeger and A. Fischer. *Die Babywindel und 34 andere Chemiegeschichten.* WILEY-VCH Verlag GmbH, Weinheim, 2000.

[69] G. Decher. Fuzzy nanoassemblies: Toward layered polymeric multicomposites. *Science*, 277:1232, 1997.

[70] F. Caruso, H. Lichterfeld, E. Donath, and H. Möhwald. Investigation of electrostatic interactions in polyelectrolyte multilayer films: Binding of anionic fluorescent probes to layer assembled onto colloids. *Macromolecules*, 32:2317, 1999.

[71] R. R. Netz and J.-F. Joanny. Complexation between a semiflexible polyelectrolyte and an oppositely charged spheres. *Macromolecules*, 32:9013, 1999.

[72] S. Y. Park, R. F. Bruinsma, and W. M. Gelbart. Spontaneous overcharging of macro-ion complexes. *Europhys. Lett.*, 46:454, 1999.

[73] K .-K. Kunze and R. R. Netz. Morphologies of semiflexible polyelectrolyte complexes. *Europhys. Lett.*, 58:299, 2002.

[74] H. Dautzenberg. Polyelectrolyte complex formation in highly aggregating systems. 1. Effect of salt: Polyelectrolyte complex formation in the presence of NaCl. *Macromolecules*, 30:7810, 1997.

[75] G. Binning, C. F. Quate, and Ch. Gerber. Atomic force microscope. *Phys. Rev. Lett.*, 56:930, 1986.

[76] R. J. Colton, A. Engel, J. E. Frommer, H. E. Gaub, A. A. Gewirth, R. Guckenberger, J. Rabe, W. M. Heckl, and B. Parkinson. *Procedures in scanning probe microscopies.* John Wiley and Sons, Inc., New York, 1998.

[77] O. Marti, B. Drake, and P. K. Hansma. Atomic force microscopy of liquid-covered surfaces: Atomic resolution images. *Appl. Phys. Lett.*, 51:484, 1987.

[78] J. Fritz, M. K. Baller, H. P. Lang, H. Rothuizen, P. Vettiger, E. Meyer, H.-J. Güntherodt, Ch. Gerber, and J. K. Gimzewski. Translating biomolecular recognition into nanomechanics. *Science*, 288:316, 2000.

[79] M. Rief, F. Oesterhelt, B. Heymann, and H. E. Gaub. Single molecule force spectroscopy on polysaccharides by atomic force microscopy. *Science*, 275:1295, 1997.

[80] IBM. Millipede. http://www.zurich.ibm.com/st/storage/concept.html.

[81] S. Lüscher, A. Fuhrer, R. Held, T. Heinzel, K. Ensslin, M. Bichler, and W. Wegscheider. Quantum wires and quantum dots defined by lithography with an atomic force microscope. *Microel. J.*, 33:319, 2002.

[82] J. Israelachvili. *Intermolecular and surface forces.* Academic press inc., London, second edition, 1998.

[83] D. Krüger, B. Anczykowski, and H. Fuchs. Physical properties of dynamic force microscopies in contact and noncontact operation. *Ann. Physik*, 6:341, 1997.

[84] N. A. Burnham, O. P. Behrend, F. Oulevey, G. Gremaud, P.-J Gallo, D. Gourdon, E. Dupas, A. J. Kulik, H. M. Pollock, and G. A. D. Briggs. How does a tip tap? *Nanotechnology*, 8:67, 1997.

[85] J. P. Spatz, S. Sheiko, M. Möller, R. G. Winkler, P. Reineker, and O. Marti. Forces affecting the substrate in resonant tapping force microscopy. *Nanotechnology*, 6:40, 1995.

[86] U. Dürig, O. Züger, and A. Stalder. Interaction force detection in scanning probe microscopy: Methods and applications. *J. Appl. Phys.*, 72:1778, 1992.

[87] J. Tamayo and R. Garcia. Deformation, contact time, and phase contrast in tapping mode scanning force microscopy. *Langmuir*, 12:4430, 1996.

[88] J. P. Cleveland, B. Aczykowski, A. E. Schmid, and V. B. Elings. Energy dissipation in tapping-mode atomic force microscopy. *Appl. Phys. Lett.*, 72:2613, 1998.

[89] F. Schabert and J. P. Rabe. Vertical dimension of hydrated biological samples in tapping mode scanning force microscopy. *Biophys. J.*, 70:1514, 1996.

[90] P. K. Hansma, J. P. Cleveland, M. Radmacher, D. A. Walters, P. E. Hillner, M. Bezanilla, M. Fritz, D. Vie, H. G. Hansma, C. B. Prater, J. Massie, L. Fukunaga, J. Gurley, and V. Elings. Tapping mode atomic force microscopy in liquids. *Appl. Phys. Lett.*, 64:1738, 1994.

[91] B. Anczykowski, D. Krüger, and H. Fuchs. Cantilever dynamics in quasinoncontact force microscopy: Spectroscopic aspects. *Phys. Rev. B*, 53:15485, 1996.

[92] B. Anczykowski, J. P. Cleveland, D. Krüger, V. Elings, and H. Fuchs. Analysis of the interaction mechanisms in dynamic mode SFM by means of experimental data and computer simulation. *Appl. Phys. A*, 66:885, 1998.

[93] J. Tamayo, A. D. L. Humphris, and M. J. Miles. Piconewton regime dynamic force micrososcopy in liquid. *Appl. Phys. Lett.*, 77:582, 2000.

[94] L. I. Pietrasanta, D. Thrower, W. Hsieh, S. Rao, O. Stemmann, J. Lechner, J. Carbon, and H. Hansma. Probing the saccharomyces cerevisiae centromeric DNA (CEN DNA)- binding factor 3 (CBF3) kinetochore complex by using atomic force microscopy. *Proc. Natl. Acad. Sci. U.S.A.*, 96:3757, 1999.

[95] S. A. Prokhorova, S. S. Sheiko, M. Möller, C.-H. Ahn, and V. Percec. Molecular imaging of monodendron jacketed linear polymers by scanning force microscopy. *Macromol. Rapid Commun.*, 19:359, 1998.

[96] R. G. Winkler, J. P. Spatz, S. S. Sheiko, M. Möller, P. Reineker, and O. Marti. Imaging material properties by resonant tapping-force microscopy: A model investigation. *Phys. Rev. B*, 54:8908, 1996.

[97] S. J. N. Noort van, K. O. V. Werf van der, B. G. Grooth de, N. F. Hulst can, and J. Greve. Height anomalies in tapping mode atomic force microscopy in air caused by adhesion. *Ultramicroscopy*, 69:117, 1997.

[98] Zhuang Wei. SFM investigation of Ni catalyzed polyisocyanide in controlled environments. Master's thesis, Institut für Physik, Humboldt-Universität zu Berlin, 2002.

[99] P. Samorí, V. Francke, T. Mangel, K. Müllen, and J.P. Rabe. Poly-para-phenylene-ethynylene assemblies for a potential molecular nanowire: An sfm study. *Optical Materials*, 9:390, 1998.

[100] F. Zenhausern, M. Adrian, R. Emch, M. Jobin, M. Taborelli, and P. Descouts. Scanning force microscopy and cryo-electron microscopy of tabacco mosaic virus as a test specimen. *Ultramicroscopy*, 42-44:1168, 1992.

[101] Olympus. Micro cantilever. Technical report, 2002.

[102] C. Bustamante, C. Rivetti, and D. J. Keller. Scanning force microscopy under aqueous solutions. *Curr. Op. Struc. Biol.*, 7:709, 1997.

[103] H. G. Hansma. Surface biology of DNA by atomic force microscopy. *Annu. Rev. Phys. Chem.*, 52:71, 2001.

[104] C. Bustamante and D. Keller. Scanning force microscopy in biology. *Physics Today*, 12:32, 1995.

[105] C. Bustamante and Rivetti C. Visualizing protein-nucleic acid interactions on a large scale with the scanning force microscope. *Annu. Rev. Biophys. Biomol. Struct.*, 25:395, 1996.

[106] M. Radmacher, M. Fritz, H. G. Hansma, and P. K. Hansma. Direct obervation of enzyme activity with the atomic force microscope. *Science*, 265:1577, 1994.

[107] G. C. Eastmond. *Comprehensive polymer sciences.* Pergamon Press, 1989.

[108] Forschungszentrum Jülich. *Physik der Polymere.* WEKA-Druck GmbH, Linnich, 1991.

[109] T. J. Odijk. Polyelectrolytes near the rod limit. *Polym. Sci. Polym. Phys. Ed.*, 15:477, 1977.

[110] J. Skolnick and M. Fixman. *Macromolecules*, 10:944, 1977.

[111] C. Rivetti, M. Guthold, and C. Bustamante. Scanning force microscopy of DNA deposited onto mica: Equilibration versus kinetic trapping studied by statistical polymer chain analysis. *J. Mol. Biol.*, 264:919, 1996.

[112] C. Bustamante, S. B. Smith, and D. Smith. Single-molecule studies of DNA mechanics. *Curr. Op. Struc. Biol.*, 10:279, 2000.

[113] R. R. Netz and D. Andelman. Neutral and charged polymers at interfaces. *cond-mat/0203364v1*, 2002.

[114] W. Nolting. *Grundkurs: Theoretische Physik, Elektrodynamik.* Zimmermann-Neufang, Ulmen, 1990.

[115] M. Abramowitz. *Handbook of mathematical functions with formulas, graphs, and mathemathicals tables.* National Bureau of Standards, Washington, 1972.

[116] G. S. Manning. *J. Chem. Phys.*, 51:924, 1969.

[117] B. H. Zimm and M. Le Bret. Counter-ion condensation and system dimensionality. *J. Biomol. Struc. Dynamics*, 1:461, 1983.

[118] B. Maier and J. O. Rädler. Conformation and self-diffution of single DNA molecules confined to two dimensions. *Phys. Rev. Lett.*, 82:1911, 1999.

[119] H. Clausen-Schaumann and H. E Gaub. DNA adsorption to laterally structured charged lipid membranes. *Langmuir*, 15:8246, 1999.

[120] Y. Fang and J. Yang. Two-dimensional condensation of DNA molecules on cationic lipid membranes. *J. Phys. Chem. B*, 101:441, 1997.

[121] O. J. Rojas, P. M. Claesson, D. Muller, and R. D. Neuman. The effect of salt concentration on adsorption of low-charge-density polyelectrolytes and interactions between polyelectrolyte-coated surfaces. *J. Colloid Interface Sci.*, 205:77, 1998.

[122] R. R. Netz and J.-F. Joanny. Adsorption of semiflexible polyelectrolytes on charged planar surfaces: Charge compression, charge reversal, and multilayer formation. *Macromolecules*, 32:9013, 1999.

[123] R. R. Netz. Elektrostatik der Erbsubstanz. *Physik Journal*, 9:54, 2002.

[124] T. Odijk. On the statistics and dynamics of confined or entangled stiff polymers. *Macromolecules*, 16:1340, 1983.

[125] S. Lifson and A. Katchalsky. The electrostatic free energy of polyelectrolyte solutions. II. Fully stretched macromolecules. *J. Polymer Sc.*, XIII:43, 1954.

[126] Q. Zhong, D. Inniss, K. Kjoller, and V. B. Elings. Fractured polymer/silica fiber surface studied by tapping mode atomic foce microscopy. *Surf. Sci. Lett.*, 290:L688, 1993.

[127] *Scanning probe microscopy training notebook.*

[128] T. J. McMaster, M. J. Miles, P. R. Shewry, and A. S. Tatham. In situ surface adsorption of the protein C hordein using atomic force microscopy. *Langmuir*, 16:1463, 2000.

[129] W. A. Deer, R. A. Howie, and J. Zussman. *Rock forming minerals.* Longmans, London, 1965.

[130] S. Nishimura, S. Biggs, P. J. Scaled, T. W. Healy, K. Tsunematsu, and T. Tateyama. Molecular-scale structure of the cation modified muscovite mica basal plane. *Langmuir*, 10:4554, 1994.

[131] C. Böttcher. Differences in air dried stained and cryomicroscopical examinations on dendronized polymers. Informell discussion.

[132] G. J. Fleer, M. A. Cohen Stuart, J. M. H. M. Scheutjens, T. Cosgrove, and B. Vincent. *Polymers at interfaces.* Chapman & Hall, London, fist edition, 1993.

[133] J. Barner. Surfactant encapsulated clusters on HOPG. Informell discussion.

[134] R. D. Jäggi, A. Franco-Oberon, P. Studerus, and K. Ensslin. Detailed analysis of forces influencing lateral resolution for q-control and tapping mode. *Appl. Phys. Lett.*, 79:135, 2001.

[135] Christof Ecker. PhD thesis, Physics of Macromolecules, Humboldt University Berlin, 2003.

[136] P. Samorí, C. Ecker, I. Gössl, P. A. J. de Witte, J. J. J. M. Cornelissen, G. Metselaar, A. E. Rowan, R. J. M. Nolte, and J. P. Rabe. High shape persistence in single polymer chains rigidified with lateral hydrogen bonding networks. *Macromolecules*, 35:5290, 2002.

[137] *Product information sheet, cloning vectors pUC19.*

[138] E. S. Sobel and J. A. Harpst. Effects of Na^+ on the persistence length and excluded volume of T7 bacteriophage DNA. *Biopolymers*, 31:1559, 1991.

[139] A. Sanchez-Sevilla, J. Thimonier, M. Marilley, J. Rocca-Serra, and J. Barbet. Accuracy of AFM measurements of the contour length of DNA fragments adsorbed on mica in air and in aqueous buffer. *Ultramicroscopy*, 92:151, 2002.

[140] H. G. Hansma and D. E. Laney. DNA binding to mica correlates with cationic radius: Assay by atomic force microscopy. *Biophys. J.*, 70:1933, 1996.

[141] R. Bruinsma. Electrostatics of DNA-cationic lipid complexes: Isoelectric instability. *Eur. Phys. J. B*, 4:75, 1998.

[142] E.M. Mateescu, C. Jeppesen, and P. Pincus. Overcharging of a sperical macroion by an oppositely charged polyelectrolyte. *Europhys. Lett.*, 46:493, 1999.

[143] T. T. Nguyen and B. I. Shklovskii. Model of inversion of DNA charge by a positive polymer: Fractionalization of the polymer charge. *Phys. Rev. Lett.*, 89:018101–1, 2002.

[144] A. Y. Grosberg, T. T. Nguyen, and B. I. Shklovskii. Colloquium: The physics of charge inversion in chemical and biological systems. *Rev. Mod. Phys.*, 74:329, 2002.

[145] S. T. Dubas and J. B. Schlenoff. Swelling and smoothing of polyelectrolyte multilayers by salt. *Langmuir*, 17:7725, 2001.

[146] I. Gössl, L Shu, A. D. Schlüter, and J. P. Rabe. Molecular structure of DNA complexes with positively charged dendronized polymers. *J. Am. Chem. Soc.*, 124:6860, 2002.

[147] I. Gössl, L Shu, A. D. Schlüter, and J. P. Rabe. Influence of monovalent salt on the molecular structure of single DNA comlexes with positively charged dendronized polymers. *Single Mol.*, 3:315, 2002.

[148] V. S. Trubetskoy, A. Loomis, J. E. Hagstrom, V. G. Budker, and J. A. Wolff. Layer-by-layer deposition of oppositely charged polyelectrolytes on the surface of condensed DNA particles. *Nucl. Acids Res*, 27:3090, 1999.

Appendix A

Abbreviations

bp	Basepair
Cryo-TEM	Cryo-Transmission Electron Microscopy
DNA	Deoxyribonucleic Acid
DH Approximation	Debye-Hückel Approximation
GSN11	Gemini Surfactant Nr. 11
GSN14	Gemini Surfactant Nr. 14
OSF Model	Odijk-Skolnick-Fixman Model
PB Equation	Poisson-Boltzmann Equation
PCFF	Polymer Consistent Force-Field
PE	Polyelectrolyte
PG1	Dendronized Polymer First Generation
PG2	Dendronized Polymer Second Generation
PG2%	Dendronized Polymer Second Generation, 30 % charges are protected
PG3	Dendronized Polymer Third Generation
PG4	Dendronized Polymer Fourth Generation
PG4%	Dendronized Polymer Fourth Generation, 30 % charges are protected
SFM	Scanning Force Microscope
SPM	Scanning Probe Microscope
STM	Scanning Tunneling Microscope
UV-C	Ultraviolet Rays (wavelengths from 200 nm to 290 nm)
WLC Model	Worm-Like Chain Model

Appendix B

Physical Variables and Constants

a	Radius of PE (Dendronized Polymer)
α	Damping Constant
b	Horizontal PE-PE Distance
c_0	Salt Concentration
δ	Vertical PE-PE Distance, Layer Thickness
ε	Dielectric Constant
F	Force
f	Spacing of Elementary Charges
I	Ionic Strength
i	Degree of Polymerization
κ^{-1}	Debye Screening Length
k	Spring Constant
$k_B = (1.38066 \pm 1) \times 10^{-23}\mathrm{JK}^{-1}$	Boltzmann Constant
$k_B T$	Thermal Energy
L_C	Length of the Complex
L_{DNA-C}	Length of DNA that is used in the Complex
l_0	Persistence Length
l_{eff}	Effective Persistence Length
l_B	Bjerrum Length
l_C	Contour Length
$< L_n >$	Number Average Molecular Length
$< L_w >$	Weight Average Molecular Length

M	Molar Mass
m	Slope
m_e	Effective Mass
$N_A = (6.022137 \pm 4) \times 10^{23}\ \mathrm{mol}^{-1}$	Avogadro Constant
$n(i)$	Number Distribution
η	Wrapping Parameter
ξ	Manning Parameter
PD	Polydispersity
Q_{eff}	Quality Factor
R	Tip Radius
r	Radius of PE (DNA)
$\rho(\vec{r})$	Charge Density
S	Tip Broadening
$\sigma(\vec{r})$	Surface Charge Density
$\tau(\vec{r})$	Line Charge Density
τ_P	Line Charge Density of PE
U	Circumference of the Cylinder
$\varphi(\vec{r})$	Electrostatic Potential
$w(i)$	Weight Distribution
X	DNA Pitch
x	Dimensionless Radius
z	Tip-Sample Distance
$Ze = Z \times (1.6021773 \pm 5) \times 10^{-19}\ \mathrm{C}$	Z × Elementary Charge

Acknowledgement

I would like to thank all the people who contributed to my thesis.

First of all, I would like to thank Prof. Dr. J. P. Rabe giving me the opportunity to work under his supervision on this thesis. In particular his engagement, discussions, and support concerning my publications and conference contributions helped me to finish the present work.

Sincere thanks are given to Prof. Dr. A. D. Schlüter for the inspiring co-operation and support during my thesis. Under his supervision Dr. Lijin Shu synthesized the dendronized polymers, whom I also would like to gratefully acknowledge for his commitment to synthesize all the different kinds of dendronized polymers, especially the partially protected ones.

I would like to thank Prof. Dr. Roland R. Netz for discussions and his interest in my results.

Beside the fruitful results of the co-operation with Steffi Reich, I would like to thank her for so many discussions on biological themes and especially to provide the linearized DNA for my experiments. I will also not forget her critical review on this thesis.

I wish to thank Dr. Ch. Böttcher and Dr. B. Schado carrying out the Cryo-TEM images of my systems.

I like to emphasize the friendly atmosphere in our working group to which have contributed all PMMs. I will remember the Thursday lunches. Hopefully this tradition will become in Adlershof as delicious as in Mitte. I would like to thank PD Dr. Stefan Kirstein for the interesting discussions on my work and that he always spared time for further discussions. Particularly at the beginning Jörg Barner and Christof Ecker were a great help for me in order to get used to the SFM and simple preparation techniques. Necessarily to bear in mind Lothar Geyer for his instantaneous help regarding all computer problems and Evi Poblenz not only for her technical support but also for her engagement concerning women in physics.

For the financial support I like to thank the Graduiertenkolleg *Polymerwerkstoffe* as well as the Sfb 448 *Mesoskopisch strukturierte Verbundsysteme*.

At the end I would like to thank my parents for their permanent and loving support, and Sixten to be encouraging on my side.

Lebenslauf

Illdiko Maria Gössl	*03.02.1974 in Kassel
Schulausbildung	
08/80 - 07/90	**Grund- und Gesamtschule/Gymnasial Zweig** in Hofgeismar
08/90 - 08/93	**Albert-Schweitzer-Gymnasium** in Hofgeismar Abschluss: Abitur
Hochschulausbildung/ Promotion	
10/93 - 07/95	**Physik/Diplomstudiengang** an der Universität Heidelberg Abschluss: Diplom-Vorprüfung
09/95 - 08/96	**Physics/BSc** am King‘s College London, GB Abschluss: Bachelor of Science in Physics
10/96 - 11/99	**Physik/Diplomstudiengang** an der Universität Heidelberg Abschluss: Diplom in Physik
10/98 - 10/99	Diplomarbeit im II. Physiologischen Institut *Quantifizierung der mechanischen Membranstabilität von Sarkolemmvesikeln mit unterschiedlichen inrazellulären Strukturproteinen*
seit 02/00	**Promotion** an der Humboldt Universität zu Berlin, Insitut für Physik Arbeitsgruppe Herr Prof. Rabe *Physik von Makromolekülen*

Appendix C

Publications

Molecular structure of DNA complexes with positively charged dendronized polymers
I. Gössl, L. Shu, A.D. Schlüter, J.P. Rabe
J. Am. Chem. Soc. **124** (2002) 6860-6865

High shape persistence in single polymer chains rigidified with lateral hydrogen bonding networks
P. Samorí, Ch. Ecker, I. Gössl, P.A.J. de Witte, J.J.J.M. Cornelissen, G. Metselaar, A.E. Rowan, R.J.M. Nolte, J.P. Rabe
Macromolecules **35** (2002) 5290-5294

Quantitative aspects of the dendronization of dendronized linear polystyrenes
L. Shu, I. Gössl, J.P. Rabe, A.D. Schlüter
Macromol. Chem. Phys. **203** (2002) 2540-2550

Meeting abstract: Influence of monovalent salt on the molecular structure of single DNA complexes with positively charged dendronized polymers
I. Gössl, L. Shu, A.D. Schlüter, J.P. Rabe
Single Mol. **3** (2002) 315-316

Erklärung

Hiermit erkläre ich, die vorliegende Arbeit selbständig und ohne unerlaubte Hilfe angefertigt zu haben und nur die angegebene Literatur und Hilfsmittel verwendet zu haben.
Ich habe mich anderwärts nicht um einen Doktorgrad beworben und besitze einen entsprechenden Doktorgrad nicht.
Ich erkläre die Kenntnisnahme der dem Verfahren zugrunde liegenden Promotionsordnung der Mathematisch-Naturwissenschaftlichen Fakultät I der Humboldt-Universität zu Berlin.

Illdiko Maria Gössl
14. April 2003